TU/e EINDHOVEN UNIVERSITY OF TECHNOLOGY

Model-based estimation and control of the particle distribution and discharge supervision in nuclear fusion reactors

Citation for published version (APA):
Blanken, T. C. (2019). Model-based estimation and control of the particle distribution and discharge supervision in nuclear fusion reactors Eindhoven: Technische Universiteit Eindhoven

Document status and date:
Published: 21/01/2019

Document Version:
Publisher's PDF, also known as Version of Record (includes final page, issue and volume numbers)

Please check the document version of this publication:

• A submitted manuscript is the version of the article upon submission and before peer-review. There can be important differences between the submitted version and the official published version of record. People interested in the research are advised to contact the author for the final version of the publication, or visit the DOI to the publisher's website.
• The final author version and the galley proof are versions of the publication after peer review.
• The final published version features the final layout of the paper including the volume, issue and page numbers.

Link to publication

General rights
Copyright and moral rights for the publications made accessible in the public portal are retained by the authors and/or other copyright owners and it is a condition of accessing publications that users recognise and abide by the legal requirements associated with these rights.

• Users may download and print one copy of any publication from the public portal for the purpose of private study or research.
• You may not further distribute the material or use it for any profit-making activity or commercial gain
• You may freely distribute the URL identifying the publication in the public portal.

If the publication is distributed under the terms of Article 25fa of the Dutch Copyright Act, indicated by the "Taverne" license above, please follow below link for the End User Agreement:

www.tue.nl/taverne

Take down policy
If you believe that this document breaches copyright please contact us at:

openaccess@tue.nl

providing details and we will investigate your claim.

Download date: 03. jul. 2019

Model-based estimation and control of the particle distribution and discharge supervision in nuclear fusion reactors

Thomas Cornelis Blanken

2019

This work has been carried out within the framework of the EUROfusion Consortium and has received funding from the EURATOM research and training programme 2014-2018 under grant agreement No 633053. The views and opinions expressed herein do not necessarily reflect those of the European Commission. This work was supported in part by the Netherlands Organization for Scientific Research via F. Felici's VENI grant "Control of plasma profiles in a fusion reactor" (no. 680.47.436). This work was supported in part by the Swiss National Science Foundation.

This work was carried out in the Control Systems Technology group at the Department of Mechanical Engineering of the Eindhoven University of Technology and at the Dutch Institute for Fundamental Energy Research, in collaboration with the Swiss Plasma Center, part of the École Polytechnique Fédérale de Lausanne in Lausanne, Switzerland, and the Max-Planck-Institut für Plasmaphysik in Garching, Germany.

A catalogue record is available from the Eindhoven University of Technology Library.
ISBN: 978-90-386-4673-2.

Typeset using LaTeX.

Reproduction: Gildeprint, Enschede, the Netherlands.

©2019 by T.C. Blanken. All rights reserved.

Model-based estimation and control of the particle distribution and discharge supervision in nuclear fusion reactors

PROEFSCHRIFT

ter verkrijging van de graad van doctor aan de Technische Universiteit Eindhoven, op gezag van de rector magnificus prof.dr.ir. F.P.T. Baaijens, voor een commissie aangewezen door het College voor Promoties, in het openbaar te verdedigen op maandag 21 januari 2019 om 13:30 uur

door

Thomas Cornelis Blanken

geboren te Nuenen

Dit proefschrift is goedgekeurd door de promotoren en de samenstelling van de promotiecommissie is als volgt:

voorzitter:	prof.dr. L.P.H. de Goey
1^{e} promotor:	prof.dr. M.R. de Baar
2^{e} promotor:	prof.dr.ir. W.P.M.H. Heemels
copromotor:	dr.ir. F.A.A. Felici (École Polytechnique Fédérale de Lausanne)
leden:	prof.dr. S. Weiland
	prof.dr.ir. J.M.A. Scherpen (Rijksuniversiteit Groningen)
	dr.ir. E. Witrant (Université Grenoble Alpes)

Het onderzoek dat in dit proefschrift wordt beschreven is uitgevoerd in overeenstemming met de TU/e Gedragscode Wetenschapsbeoefening.

Summary

Model-based estimation and control of the particle distribution and discharge supervision in nuclear fusion reactors

Controlled nuclear fusion is a potential sustainable source of energy to complement other energy sources in meeting the increasing energy consumption of humanity. The furthest developed concept for a fusion reactor is the tokamak. In a tokamak reactor, a plasma (an ionized gas) is confined using magnetic fields and heated to achieve the conditions for fusion.

Control of tokamak plasmas is important for reliable high-performance operation in future reactors. Among other parameters, the plasma particle density must be estimated and controlled in feedback. Also, various control tasks must be simultaneously executed by the plasma control system, in both normal operation as well as in off-normal conditions, such as unexpected deviations from the target plasma scenario and hardware failure.

In this thesis, first, a model-based approach to real-time estimation of the particle density distribution in tokamak plasmas is presented, based on Extended Kalman filtering. This estimator merges multiple measurements with a control-oriented model of the density evolution. It is employed in experiments on the ASDEX Upgrade and TCV tokamaks. A good agreement between the real-time estimated density and offline available measurements is obtained. Also, a model-based feedback controller for the particle density is designed and employed on TCV. This controller achieves good tracking despite disturbances.

Second, a generic architecture for task-based supervisory plasma control is proposed. This architecture is implemented on the TCV control system and integrated with an actuator management algorithm, state estimation algorithms and controllers. In experiments on simultaneous control of the plasma pressure, the safety factor profile and neoclassical tearing modes, the supervisory controller

assigns priorities to the relevant control tasks based on the plasma state.

The methods developed in this thesis for distributed control and supervisory control are expected to be relevant for other distributed control challenges, for fusion reactors and in other applications.

Contents

1 Introduction **1**
1.1 Nuclear fusion: a clean source of energy 1
1.2 Magnetic confinement of a hot plasma: the tokamak 3
1.3 Control of tokamak plasmas 6
1.4 Research objectives and contributions 10
1.5 Outline of this thesis 11

2 Control-oriented modeling of the plasma particle density in tokamaks and application to real-time density profile reconstruction **13**
2.1 Introduction 14
2.2 Control-oriented 0+1D model of the particle transport 16
2.3 Dynamic state observer design using Kalman filtering 29
2.4 Future extensions and research 44
2.5 Conclusion 45
2.6 Acknowledgments 45
Appendix 46
2.A Spatial discretization using a finite-element method 46
2.B Time discretization using a trapezoidal method 50
2.C Numerical evaluation of line integrals 51

3 Model-based real-time plasma electron density profile estimation and control on ASDEX Upgrade and TCV **53**
3.1 Introduction 54
3.2 Model-based density profile observer 56
3.3 Profile estimation in high-density experiments on ASDEX Upgrade 59
3.4 Density control in integrated control experiments on TCV 69
3.5 Discussion 76
3.6 Conclusions 78

3.7 Acknowledgments 78
Appendix 79
3.A Equation summary of RAPDENS model 79
3.B Equation summary of the observer equations 81
3.C Details of controller design 84

4 Real-time plasma state monitoring and supervisory control on TCV 89
4.1 Introduction 90
4.2 Generic plasma control system software architecture 94
4.3 Design of a generic plasma state monitor 98
4.4 Design of a generic supervisory controller 104
4.5 Implementation and results on TCV 107
4.6 Discussion 116
4.7 Conclusions and outlook 117
4.8 Acknowledgments 119

5 Conclusions, discussion and recommendations 121
5.1 Conclusions 121
5.2 Discussion 123
5.3 Recommendations 128

Bibliography 133

Glossary 147

Dankwoord 149

Curriculum vitae 151

List of publications 153

Chapter 1

Introduction

The relevance and principles of nuclear fusion energy and tokamaks are introduced and a number of challenges related to control of tokamaks are stated. Next, the research objectives of this thesis and the contributions are presented and an outline of this thesis is given.

1.1 Nuclear fusion: a clean source of energy

The ever-increasing energy demand of humanity, combined with the environmental impact of the consumption of fossil fuels, calls for new sources of clean, sustainable, environmentally-friendly and long-lasting energy production [Intergovernmental Panel on Climate Change, 2007, 2018; International Energy Agency, 2016; Mackay, 2009]. Various renewable energy sources (e.g. wind power, solar energy, hydropower, geothermal energy) can provide significant portions of our energy consumption. However, they are difficult to scale to proportions needed to sustain the total consumption on earth. Nuclear (uranium) fission power plants can provide large amounts of energy, but produce long-lived nuclear waste. Moreover, the public opinion often opposes the production of fission energy due to safety concerns.

In looking for another more viable solution, we can take inspiration from our sun and other stars. They produce massive amounts of energy by nuclear fusion: the process by which light elements are fused [McCracken and Stott, 2012]. The application of nuclear fusion in a power plant on earth could provide a sustainable energy source without greenhouse gas emissions [McCracken and Stott, 2012; Sánchez, 2014]. The resulting nuclear waste has a considerably shorter lifespan compared to the nuclear waste from fission power plants. Among other sources of energy, nuclear fusion power is considered as one viable option

to provide clean energy in the future. The international community has initiated the development of nuclear fusion reactor power plants [McCracken and Stott, 2012]. However, the realization of a nuclear fusion power plant is extremely problematic and many challenges have been identified. In order to illustrate these challenges, the basics of nuclear fusion energy are briefly introduced.

The fusion reaction between deuterium and tritium nuclei (two isotopes of hydrogen) is the easiest to initiate, and yields a helium nucleus and a neutron [Freidberg, 2007; McCracken and Stott, 2012]:

$$\mathrm{D} + \mathrm{T} \rightarrow {}_2\mathrm{He}^4\ (3.5\,\mathrm{MeV}) + \mathrm{n}\ (14.1\,\mathrm{MeV}) \tag{1.1}$$

This produces an energy of 17.6 MeV (about 2.8 pJ) per reaction. Deuterium is naturally abundant in sea water and can easily be extracted. Tritium is not available and has to be produced from lithium by a fission reaction which is triggered by a neutron that is released by the fusion reaction (1.1) [Freidberg, 2007]. Lithium is abundant on earth.

For the fusion reaction, the repulsive forces between the positively charged nuclei must be overcome. It can be shown that a deuterium-tritium fuel temperature of 20 keV is optimal for the fusion reaction, that is 2.3×10^8 K. A reactor must confine many deuterium and tritium particles as efficiently as possible at this temperature. It has been shown that for a self-sustained fusion reaction, the product of the particle density n, temperature T and energy confinement time τ_E must exceed a critical value, see e.g. [Wesson, 2004]. This event is called ignition and the condition is expressed as

$$nT\tau_\mathrm{E} > 3 \times 10^{21}\ \mathrm{m}^{-3}\,\mathrm{keV\,s} \tag{1.2}$$

The energy confinement time quantifies the confinement quality; it is the thermal energy divided by the heat loss power, i.e. $\tau_\mathrm{E} = E_\mathrm{th}/P_\mathrm{loss}$. Different values of the value on the right-hand side of (1.2) may apply depending on assumptions of the spatial distributions of density and temperature [Freidberg, 2007; McCracken and Stott, 2012]. Under these conditions, the fusion fuel is in the so-called plasma state of matter, where all atoms are fully ionized. Plasmas are electrically conductive and respond strongly to electromagnetic forces [Freidberg, 2007].

Unfortunately, creating deuterium-tritium plasma that satisfies the condition (1.2) at 2.3×10^8 K is not easy. On earth, it can only be achieved in dedicated machines. Magnetic fields can be applied to confine hot plasmas. Multiple machine concepts for magnetic fusion reactors have been developed [Freidberg, 2007; McCracken and Stott, 2012]. The most advanced magnetic confinement concept is the tokamak [Wesson, 2004].

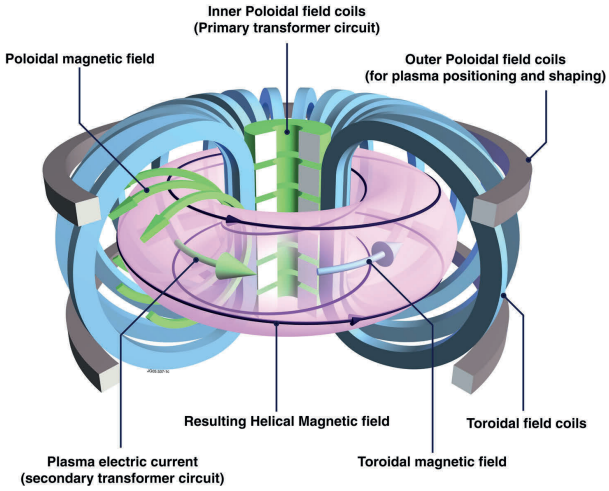

Figure 1.1 – Schematic layout of a tokamak. Magnetic field coils produce a helical magnetic field, that can confine a hot plasma. Source: EUROfusion (`https://www.euro-fusion.org/`.)

1.2 Magnetic confinement of a hot plasma: the tokamak

Tokamaks are machines that use magnetic fields to confine a hot plasma. They have reached the highest value of the product $nT\tau_{\mathrm{E}}$ (see (1.2)) compared to machines of different (magnetic) configurations [Braams and Stott, 2002; McCracken and Stott, 2012]. It is therefore the most promising design for nuclear fusion reactors that will produce energy in an economically efficient way. Economic considerations, engineering constraints and nuclear physics constraints imply that a realistic fusion reactor must operate at a density around $n \approx 1.5{\times}10^{20}$ m^{-3} (about 170000 times smaller than in air at room temperature), a temperature around $T \approx 20$ keV and a confinement time in the order of $\tau_{\mathrm{E}} \approx 1$ s, see [Freidberg, 2007]. For comparison, the core of the sun has a temperature of about 1.57×10^7 K. The ITER tokamak [IAEA, 2001] is currently being constructed, and will generate 500 MW fusion power at an input power of 50 MW [The ITER Organization].

The principles of magnetic confinement in tokamaks and the operational limits are provided next, in order to introduce the control challenges later on.

1.2.1 Magnetic equilibrium and kinetic profiles

A tokamak consists of a toroidal (torus-shaped) vacuum vessel surrounded by magnetic field coils to confine a toroidal plasma. Figure 1.1 shows the layout of a

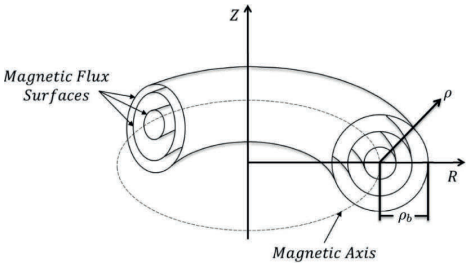

(a) Nested flux surfaces in a magnetic equilibrium. Source: [Boyer et al., 2014].

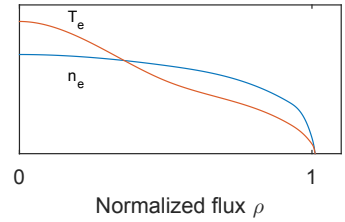

(b) Representative profile shapes of electron density and temperature as a function of the radial variable associated with the toroidal flux.

Figure 1.2 – Graphical representation of a cross-section of a tokamak plasma and typical profiles of density and temperature.

tokamak. A toroidal magnetic field B_{T} is generated by toroidal field coils. A loop voltage is induced by ramping a current in the primary transformer circuit and this drives a toroidally flowing current I_{p}. This current produces the poloidal magnetic field. The combination of the toroidal and poloidal fields produces a helical magnetic field. Additional poloidal field coils are used to position and shape the plasma. The helical magnetic field creates a macroscopic force balance (called equilibrium) in which the kinetic pressure of the plasma is balanced by an inward Lorentz force [Freidberg, 2007]. The force balance implies that the plasma is confined.

The plasma equilibrium has a set of nested surfaces of constant poloidal and toroidal flux, called flux surfaces. These surfaces are toroidally symmetric. The surfaces are labelled by the normalized radius ρ. In Figure 1.2a, the flux surfaces of a tokamak plasma are shown. A special flux surface is the so-called last closed flux surface (LCFS). Inside the LCFS, the plasma is organized in a set of nested closed flux surfaces. The kinetic pressure is constant on these surfaces because of the force equilibrium. Transport of heat and particles parallel to these surfaces is orders of magnitude faster than perpendicular to the surfaces. As a consequence, the surfaces also have constant temperature. Outside the LCFS, the magnetic field lines intersect the reactor wall. Particles and heat in the narrow region outside the LCFS flow towards the wall structures. The LCFS is represented by $\rho = 1$, and $\rho = 0$ represents the magnetic axis. In this thesis, we approximate that also the density is constant on a flux surface, although this is strictly speaking not correct. In Figure 1.2b, typical profiles of density $n\,(\rho)$ and temperature $T\,(\rho)$ are plotted.

Magnetohydrodynamics (MHD), i.e. the combination of fluid dynamics, Maxwell's equations of electromagnetism and the Lorentz force, provide a framework to analyze the plasma equilibrium and perturbations thereof, as well as the evolution

of the kinetic quantities and magnetic field, see [Zohm, 2014].

1.2.2 Tokamak reactor performance and stability limits

In order to produce energy in a economically viable way, a nuclear fusion reactor must operate at high performance. The design of a nuclear fusion power plant originates at the integration of the requirements, technological constraints and design variables. As such, the machine dimensions and nominal plasma parameters are determined by the desired output power, constraints on the maximum heat load, maximum magnetic field strength and maximum mechanical stresses, as well as nuclear physics constraints. This is explained in e.g. [Freidberg, 2007].

However, the resulting designs of ITER and DEMO are such that the plasma is inherently unstable. The normalized plasma pressure $\beta \propto nTB^{-2}$ at which these machines must operate is above MHD stability limits [Zohm, 2014]. The performance-limiting instability for ITER and DEMO is a MHD stability called the neoclassical tearing mode (NTM) [la Haye, 2006; Zohm, 2014]. The presence of a NTM in the plasma leads to a reduction of the energy confinement, which will reduce the reactor performance below its requirements. Other MHD stability limits set limits on e.g. the achievable plasma current, density, magnetic field distribution and shape [Greenwald et al., 1988; Wesson, 2004].

More importantly, exceeding the MHD stability limits can cause a plasma disruption. This is a quick and violent expulsion of heat and particles from the plasma, which can result in structural damage and downtime of the reactor [Riccardo, 2008]. On ITER, a disruption during high-performance operation has the potential to do significant damage if it is not mitigated. For example, in a disruption, a thermal energy of roughly 350MJ is released to the wall structures in tens of milliseconds. Disruptions have to be avoided by proper control of the tokamak. This is further introduced in Section 1.3.

1.2.3 Tokamaks considered in this thesis

The results in this thesis have been obtained on two tokamaks: TCV and ASDEX Upgrade. Over the years, many tokamaks have been built for scientific research as well as fusion power demonstration. For example, TCV [Coda et al., 2017], ASDEX Upgrade [Neu et al., 2016], DIII-D [Luxon, 2002] and JET [Horton and JET Contributors, 2016] are used for scientific research into the nature of (fusion) plasmas. Additionally, the JET and TFTR tokamaks have demonstrated the production of energy from nuclear fusion, although with considerable external heating power [Bell, 2016; Keilhacker et al., 2001]. The ITER tokamak is currently under construction in France [IAEA, 2001; The ITER Organization], and will produce net energy from fusion. To provide a sense of scale to the reader, TCV, ASDEX Upgrade and ITER are shown in Figure 1.3, and some dimensions and parameters of these tokamaks are listed in Table 1.1.

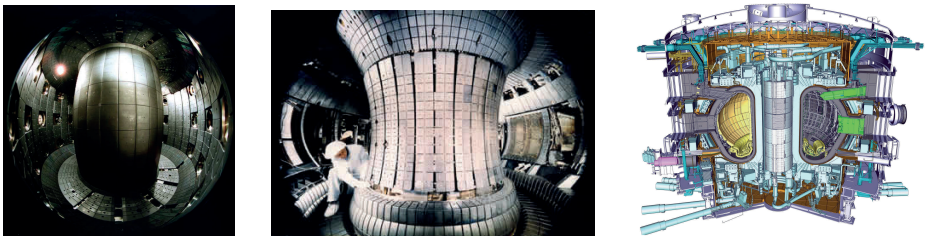

(a) TCV **(b)** ASDEX Upgrade **(c)** ITER

Figure 1.3 – The interior of TCV and ASDEX Upgrade, and a cutaway diagram of ITER.

Table 1.1 – Dimensions and parameters of TCV and ASDEX Upgrade (AUG) as of 2018, and ITER.

	TCV	AUG	ITER
Major radius R [m]	0.88	1.65	6.2
Toroidal magnetic field B_T [T] at mid-radius	1.5	2.5	5.3
Plasma current I_p [MA] (maximum)	1	1.6	15
Installed auxiliary heating and current drive power P_aux [MW]	3	31	73

1.3 Control of tokamak plasmas

In order to achieve stable, high-performance plasmas in long discharges, active control of the plasma is necessary. In the context of this thesis, control refers to the automated manipulation of a process such that quantities in that process follow a desired evolution in time [Skogestad and Postlethwaite, 2001]. Many important control problems in tokamaks exist [Gribov et al., 2007; Humphreys et al., 2015; Pironti and Walker, 2005], corresponding to control of:

- the plasma current, position and shape,
- the radial plasma profiles of density, temperature, and current density,
- magnetohydrodynamic instabilities: sawteeth, (neoclassical) tearing modes, edge localized modes, resistive wall modes,
- detachment and power exhaust,

Additionally, plasma supervision must coordinate all control and actuation. On a tokamak, a plasma control system (PCS) hosts all real-time algorithms, such as feedback controllers. Plasma control can be divided in three categories:

1. **Control of the quantities along nominal trajectories** The PCS must ensure that the plasma quantities evolve along time-varying references.

These bring the plasma from the start of the discharge to the desired operating point (for fusion power production or scientific research), and vice versa to the end of a discharge. Feedback control is needed since discharge-to-discharge differences in machine conditions and other disturbances can otherwise lead to the quantities diverging from references.

2. **Avoiding operational limits and stability limits** Some plasma quantities are open-loop unstable in the operating point of the reactor, or the trajectories to that operating point. Almost all of the aforementioned operational limits are the result of unstable dynamics.
3. **Intervening when instabilities are triggered** When operational (stability) limits are exceeded, the PCS must take corrective actions to bring the plasma back to the nominal trajectories.

The avoidance of plasma disruptions is part of the second and third category.

Feedback control of tokamak plasmas is not trivial. It requires immediate and accurate knowledge of the system state. Often, sensors in tokamaks do not directly measure the quantities of interest, but measure quantities that are derived or are spatially located elsewhere, see [Hutchinson, 2002]. While sensors on present-day experimental devices are numerous, the set of sensors on a fusion reactor is restricted [Boivin, 2016; Donné et al., 2007]. This is because of the limited space available for sensor equipment, as well as the harsh nuclear (radioactive) environment inside the device [Biel et al., 2015].

This thesis addresses two major challenges in control of tokamak plasmas:

1. the control and estimation of the spatial distribution of the plasma particle density, and
2. the integration of various estimation and control algorithms with supervision algorithms, in particular for avoidance of operational limits.

The state of the art, future required solutions and challenges are discussed next. After that, the objectives and contributions of this thesis are presented.

1.3.1 Plasma particle density control and estimation

In order to achieve a high fusion power in steady-state, the density n of the fuel nuclei in the plasma must be maintained constant at a relevant value [Gribov et al., 2007].

Density control requirements

The requirements on the bandwidth, steady-state error and disturbance rejections of the closed-loop on, e.g., ITER has not been clearly documented. However, it would be advantageous to achieve zero steady-state error, maximize the bandwidth and reject low-frequent disturbances within the physical limits of the system in order to achieve maximum operational flexibility. In any case,

the bandwidth is lower-bounded by the discharge duration, and upper bounded by the particle confinement time, actuation timescales and measurement noise content.

Disturbances on a density feedback loop

There are multiple sources of disturbances acting on (a feedback loop for) the plasma density. An example of physical disturbances on the plant is variation in energy confinement and transport due to magnetohydrodynamic instabilities. Examples of other disturbances entering the feedback loop are sensor noise, sensor artifacts (e.g., spurious biases on interferometers), and sensor failure (e.g., hardware damage, misalignment or interference leading to inconsistent signal values).

The state of the art and gap analysis

On present-day tokamaks, feedback controllers are often tuned on a trial-and-error basis. Sometimes many discharges are required to obtain a satisfactory result. However, on ITER there will be limited opportunity to use discharges for the tuning of control algorithms. Experimental time on ITER is costly and limited. Moreover, most often a single measurement channel is used for density feedback control, see e.g. [Janky et al., 2015; Vijvers et al., 2012]. This proves to be vulnerable to measurement errors, such as embodied by spurious biases [Gil et al., 2010; Mlynek et al., 2014]. Over the years, different low-complexity models have been developed that can be used to tune feedback controllers [Juhn et al., 2012; Vijvers et al., 2012], but these did not consider the spatial distribution of the density.

The challenge

On future nuclear fusion reactors, the real-time controller and estimator for the plasma particle density should operate properly from their first deployment with minimal tuning on a trial and error basis. Real-time control and estimation algorithms should be tested thoroughly in closed-loop simulations before being used in plasma operations. The estimation results should be as accurate as possible with the given measurements, and should not deteriorate due to measurement errors. Furthermore, the steady-state control error should be as small as possible, the control bandwidth should be as high as possible, and disturbances should be rejected. This challenge calls for model-based design of controller algorithms, such as seen in [Felici et al., 2016; Moreau et al., 2013] and validation of the control system (components) in simulation [de Vries et al., 2018].

1.3.2 Operational limits, integrated control and plasma supervision

A reactor plasma control system (PCS) must simultaneously control all relevant plasma quantities such as density, temperature, safety factor profile, shape, position, NTM island width, sawtooth period, etc. [Gribov et al., 2007; Humphreys et al., 2015], ensuring that they stay close to their targets and references. The instabilities mentioned in Section 1.2.2 can cause the plasma to deviate from its targets and can lead to a disruption [De Vries et al., 2011]. In order to protect the investment and avoid structural damage to the hardware, a tokamak reactor is equipped with a machine protection system. One part of the protection system is the disruption mitigation system, which is designed to alleviate the adverse effects of a disruption when a disruption occurs. Still, disruptions are undesired even if mitigated. To this extent the PCS should, as a first line of defense, actively avoid operational limits or exciting physical instabilities as best as possible with its resources and its capabilities. Some physics instabilities can arise unexpectedly throughout a discharge.

The state of the art and gap analysis

A multitude of actuators for the suppression and stabilization of these instabilities have been identified, see e.g. [Maraschek et al., 2018]. Moreover, (feedback) control methods have been developed using modern control theory for these instabilities, see e.g. [van den Brand et al., 2013; Hennen et al., 2010; Kong et al., 2017; Lauret et al., 2016; Olofsson et al., 2016; Witvoet et al., 2012]. However, the resources for actuation are constrained on a reactor. The total installed actuation power is only slighty larger than the nominally required power, to minimize investment and operational costs of a reactor. Also, actuator availability can change during a plasma discharge and the actuation is shared (i.e. actuators for heating are also those for suppression of instabilities) [Maljaars and Felici, 2017]. Depending on the state of the plasma and the actuators, not all control objectives may be realized simultaneously. This implies that a PCS must prioritize its control objectives. This can be called plasma supervision.

The challenge

The plasma control system of a reactor should contain a plasma supervision algorithm. This supervisory controller must manage the allocation of actuators to individual controllers based on the state of the machine. For example, it must respond to off-normal events such as (the onset of) magnetohydrodynamic instabilities, the approach of operational limits, or hardware failure. Plasma supervision requires a careful integration of (developed) state estimation algorithms, state monitors, controllers, and actuator allocation algorithms.

1.4 Research objectives and contributions

The challenges stated in Section 1.3.1 and 1.3.2 cover a wide range of problems and topics in the control of tokamaks. The aim of this thesis is to accomplish two specific research objectives, which contribute solutions to those challenges. The first research objective of this thesis is formulated as:

> **Research objective 1:** Develop model-based techniques for the estimation and control of the spatial distribution of the plasma particle density in tokamaks.

The contributions to accomplish this research objective are:

Contribution 1: A design of a control-oriented physics-based model for the evolution of the electron density in tokamak plasmas. The dynamics of the electron density profile is modeled using particle conservation laws and low-complexity empirical particle transport and source models. The model is suited for real-time computations and is geared towards control applications. It is called the RAPDENS model[1].

Contribution 2: A design of a model-based state observer for the plasma electron density profile in tokamaks. An Extended Kalman filter-based observer for estimation of the electron density profile is derived from the RAPDENS model and a forward measurement model.

Contribution 3: A design for model-based feedback control of the plasma electron density in tokamaks. A feedback controller for the electron density is derived using robust H_∞ synthesis on the RAPDENS model.

Contribution 4: Demonstration of density profile estimation in reactor-relevant experiments on the ASDEX Upgrade tokamak. The observer is implemented on the real-time plasma control system of ASDEX Upgrade. It uses both interferometry and Bremsstrahlung measurements for density profile estimation. The accuracy of its profile estimation is evaluated by comparison to offline-available measurements. The observer is employed in feedback control experiments with pellet fuelling, where the observer provides the estimated core density.

Contribution 5: Demonstration of density profile estimation and feedback control in experiments on the TCV tokamak. The observer and feedback controller are implemented on the real-time plasma control system of TCV and employed in feedback control experiments. The profile-averaged density is controlled in presence of disturbances from electron cyclotron heating and current drive. The profile estimation accuracy is evaluated by comparison to offline-available measurements.

[1] The model is called RAPDENS (RApid DENsity Simulator), since it shares some similarities with the RAPTOR model for the evolution of temperature and poloidal magnetic flux profiles [Felici et al., 2011]. The observer implementations are called RAPDENS-observer.

The second research objective is formulated as:

Research objective 2: Develop a control system architecture including a plasma supervision system that allows operating a tokamak close to operational limits.

The contributions to accomplish this research objective are:
Contribution 6: A design of a plasma control system architecture for task-based supervisory control on tokamaks. A generic PCS architecture is developed. This architecture integrates state estimation and reconstruction algorithms, a monitor for finite states of the plasma, a supervisory controller, actuator management for resource allocation and (feedback) controllers. The supervisory controller prioritizes various tasks depending on the finite state of the plasma and actuators. These tasks embody the objectives of the individual feedback controllers and their priorities determine the allocation of actuation resources to controllers.
Contribution 7: A demonstration of task-based supervisory control in experiments on the TCV tokamak. The architecture is implemented on the TCV control system, integrating existing controllers and observers with a novel plasma state monitor and supervisory controller. Its capabilities are demonstrated in experiments on NTM detection and integrated control of NTMs and the plasma pressure and safety factor profile.

1.5 Outline of this thesis

The remainder of this thesis is organized as follows. In Chapter 2, the control-oriented modeling of the plasma electron density is presented (**Contribution 1**). Also, its application to density profile estimation using an observer is shown in simulations using TCV data (**Contribution 2**). This chapter is published in Fusion Engineering and Design ([Blanken et al., 2018b]). In Chapter 3, the model-based observer is summarized and the model-based feedback controller design is presented (**Contribution 3**). Moreover, the implementations of the observer and controller and experimental results on ASDEX Upgrade and TCV are presented (**Contribution 4 and 5**). This chapter is submitted to Fusion Engineering and Design. In Chapter 4, the control system architecture with the plasma state monitoring and task-based supervisory controller is proposed (**Contribution 6**) and experimental results of plasma state monitoring and supervisory control are presented (**Contribution 7**). This chapter is published in Nuclear Fusion ([Blanken et al., 2018a]). Finally, in Chapter 5 the main conclusions of the presented work are drawn, the work is discussed in relation to current research and recommendations for future research are given.

Chapter 2

Control-oriented modeling of the plasma particle density in tokamaks and application to real-time density profile reconstruction

Abstract A model-based approach to real-time reconstruction of the particle density profile in tokamak plasmas is presented, based on a dynamic state estimator. Traditionally, the density profile is reconstructed in real-time by solving an ill-conditioned inversion problem using a measurement at a single point in time. This approach is sensitive to diagnostics errors and failure. The inclusion of a dynamic model in a real-time estimation algorithm allows for reliable reconstruction despite diagnostic errors. Predictive simulations show that the model can reproduce the density evolution of discharges on TCV and ASDEX Upgrade after tuning of a few parameters. Offline reconstructions using experimental data from TCV show accurate estimation of the density profile and show examples of fault detection of interferometry signals.

This chapter is published as: T.C. Blanken, F. Felici, C.J. Rapson, M.R. de Baar, W.P.M.H. Heemels, the TCV team and the ASDEX Upgrade team (2018), Control-oriented modeling of the plasma particle density in tokamaks and application to real-time density profile reconstruction, Fusion Engineering and Design, 126, 87-103.

2.1 Introduction

A key challenge in tokamak operations is maintaining stable plasma conditions, remaining within safety limits and accurate control of the plasma state [Pironti and Walker, 2005]. Plasma control has expanded in recent years from control of bulk plasma quantities (such as total plasma current, average particle density and average temperature) to control of the spatial distributions of these quantities, e.g. the profiles of temperature, safety factor and rotation [Barton et al., 2012; Boyer et al., 2014; Goumiri et al., 2016; Maljaars et al., 2015; Moreau et al., 2013].

Since the density profile affects the plasma pressure and fusion power [Wesson, 2004], drives radiation, influences the non-inductive current distribution, determines diagnostics validity (e.g. ECE cut-off), and can trigger detrimental plasma instabilities [Boozer, 2012; Zohm, 2014], real-time monitoring and control of the particle density profile is of great importance for safe, reliable and high-performance operation of large tokamaks such as ITER [Biel et al., 2015; Gribov et al., 2007; Hender et al., 2007; Loarte et al., 2007].

An important challenge can be identified as to enable density control, namely the reliable real-time reconstruction of the density profile from diagnostic measurements. Most tokamaks have diagnostics for the plasma particle density that can be used for monitoring and real-time control. Often an interferometry system is used, which measures the line-integrated electron density along one or more laser chords intersecting the plasma [Donné, 1995; Hutchinson, 2002], but other possibilities include Thomson scattering [Donné et al., 2008; Hutchinson, 2002] and reflectometry [Hutchinson, 2002; Weiwen et al., 2006].

In control and monitoring of the density, the line-averaged density is often considered, which is conveniently derived from an interferometry signal if the chord intersection length is known. Moreover, there exist data fitting methods for reconstruction of the density profile for analysis or control that minimize a least-squares criterium or fit splines on multiple interferometry channels [Chiang et al., 1997; Fischer and Dinklage, 2004; Furno et al., 2005; Koponen and Dumbrajs, 1997; Mlynek, 2010; Mlynek et al., 2011; Park, 1989] or Thomson scattering [Fischer et al., 2002; Maddison et al., 2006] at one point in time.

However, the estimates obtained by these static data fitting methods are sensitive to diagnostic faults [Mlynek, 2010; Murari et al., 2006], notably drifts. For example fringe jumps occur in an interferometry system if the density fluctuates rapidly, often when a pellet is injected. This may result in a loss of control performance or even a loss of density control.

Despite ongoing research on detection and correction of fringe jumps [Gil et al., 2010; Mlynek et al., 2011; Murari et al., 2006; Zabeo et al., 2004], no reliable solution is being used on TCV and ASDEX Upgrade. Moreover, data fitting methods can suffer from ill-conditioning, leading to unrealistic profiles with spatial oscillations [Mlynek, 2010].

The inclusion of a dynamic model of the density profile evolution in the profile reconstruction may solve these issues by promoting proximity of the measured quantities to solutions that are feasible with respect to our knowledge of the modeled process. Thereby it can suppress unrealistic spatial oscillations in the profile estimate, reject measurement noise and anticipate for the effects of actuation, such as fuelling, on the density evolution.

For this purpose, we present a control-oriented model of the plasma particle density evolution. We prefer a white-box model-based approach over identifying models from data since nonlinear behaviour and physical couplings that evolve in time complicate identification of processes from measurement data. On the other hand, full first-principle physics modeling is challenging since

1. transport inside a tokamak plasma LCFS is modeled by the combination of a set of 1D PDEs for radial transport and a 2D elliptical PDE for the magnetic equilibrium (see [Hinton and Hazeltine, 1976; Pereverzev and Yushmanov, 2002]) which is difficult and time-consuming to solve in combination with calculation of the particle fluxes, and

2. transport outside the tokamak plasma LCFS consists of complex processes such as wall retention and recycling, neutral particle dynamics, and atomic and molecular processes (see [Stangeby, 2000; Wesson, 2004]) which are all complex to model in themselves, let alone in their interaction.

Because of these complications, heuristic models are better suited for real-time applications in this case. We present a control-oriented and real-time nonlinear model for radial (1D) plasma density transport with additional particle inventories (0D) of the wall and vacuum. Compared to existing multi inventory (0D) models for density control [Boncagni et al., 2013; Brelen, 1994; Fielding et al., 1978; Juhn et al., 2012; Maddison et al., 2006; Vijvers et al., 2012; Wong et al., 1992], we replace the plasma particle inventory by the spatial distribution of the plasma density. Moreover, we include the influence of plasma equilibrium, temperature, current and operational modes (limited or diverted plasma, low or high confinement [Wesson, 2004]) on the transport processes and diagnostics.

In this paper, we use for the first time a model-based dynamic state observer for density profile reconstruction. The observer, comprising of an Extended Kalman filter [Anderson and Moore, 1979], provides both estimates of the density profile as well as reality vs. model deviations that persist over multiple confinement times from multiple diagnostics signals. Here we build upon earlier work in [Felici et al., 2011, 2014a], where physics-model-based dynamic state observers have been applied for real-time estimation of the current and temperature profiles. In the observer, we employ a threshold method to detect fringe jumps [Murari et al., 2006], from the discrepancy between the measured interferometry signals and the model-based predictions of these measurements.

The proposed dynamic state observer algorithm can be implemented on control systems of existing tokamaks, and used for e.g. real-time density feedback

control and/or deriving whether ECE channels are in cut-off in real-time. For future tokamaks as ITER, this model-based design procedure can be performed today with models extrapolated from existing tokamaks and iterated using the same methodology as density transport parameters become better known in the course of ITER operation. We want to emphasize that the purpose of this paper is not to make statements on the physics of density evolution in tokamaks. Instead, the objective is to demonstrate that a control-oriented model can be used to enhance real-time reconstruction of the density profile.

The remainder of this paper is structured as follows. The control-oriented model of the density transport and synthetic interferometer model is introduced in Section 2.2, along with simulations of a TCV and an ASDEX Upgrade discharge. The design of the observer, the detection of fringe jumps and the offline estimation results on experimental data are discussed in Section 2.3. Extensions and future work that is in line with the proposed solutions are discussed in Section 2.4. Finally, concluding remarks are given in Section 2.5.

2.2 Control-oriented 0+1D model of the particle transport

In this section, a 0D+1D diffusion/drift transport model is presented for control purposes, with the flexibity to adapt for multiple devices, multiple diagnostics and multiple actuators. Particle transport in the plasma, particle flows and sources in the tokamak are modeled in a heuristic fashion, rather than using complex first-principle transport models.

Existing physics models of plasma particle transport (e.g. [Romanelli et al., 2015; Tamain et al., 2007]) and models used in offline profile reconstruction algorithms (e.g. ASTRA [Pereverzev and Yushmanov, 2002], CRONOS [Artaud et al., 2010]) are not directly suitable for the task of real-time density reconstruction, since their execution time generally exceeds the discharge duration. It has been shown in [Barton et al., 2012; Boyer et al., 2014; Felici et al., 2011, 2014a; Maljaars et al., 2015; Moreau et al., 2013] that low-complexity 1D models can be used for reconstruction and control of the temperature and safety factor profiles.

Our model consists of a 1D drift-diffusion PDE for radial particle transport and two 0D ODEs for the time evolution of the inventory of the wall and the neutral vacuum, all based on particle conservation laws. This approach is similar to multi inventory (0D) models for controller design on TCV [Vijvers et al., 2012], JET [Brelen, 1994], TEXT [Wong et al., 1992] and KSTAR [Juhn et al., 2012], but here the radial particle transport in the plasma is also modeled. Since transport on flux surfaces is several orders of magnitude faster than radial transport (perpendicular to flux surfaces), we may consider radial plasma transport only [Hinton and Hazeltine, 1976]. The ionization, recombination and recycling

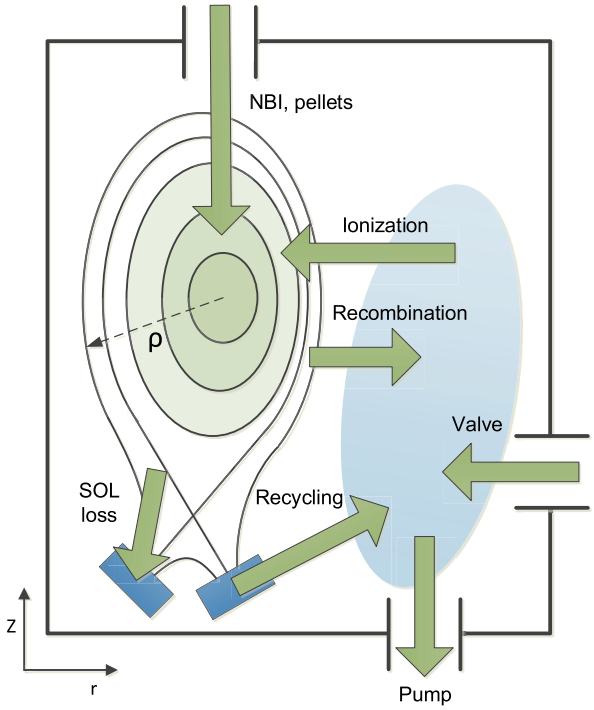

Figure 2.1 – Schematic representation of the tokamak cross-section in the *R-Z* plane. Depicted are the plasma, the wall components, the neutral vacuum and the modeled particle flows.

terms are approximated, and the NBI and pellet injection deposition locations are postulated. See Figure 2.1 for a schematic representation of the modeled transport flows considered in this model.

The particle transport processes change in time due to a variety of physical factors. The LCFS electron temperature $T_{\mathrm{e,b}} = T_{\mathrm{e}}|_{\rho=1}$, electrical current I_{p}, plasma geometry through 2D equilibrium $\psi(R, Z)$ and distinct operational regimes (limited or diverted plasma $c_{\mathrm{D}} \in \{0, 1\}$, low or high confinement mode $c_{\mathrm{H}} \in \{0, 1\}$) are included in the model as a time-varying external input parameter. It is assumed that estimates of these parameter values are available through real-time 2D equilibrium reconstruction and other diagnostics.

The PDE is discretized in space and the resulting set of ODEs is then discretized in time. The relation between plasma density and measured quantities is included using diagnostics models.

2.2.1 1D radial plasma transport

Let us start by defining the usual toroidal flux surface label $\rho_{\text{tor}} = \sqrt{\frac{\Phi}{\pi B_0}}$ where Φ is the toroidal magnetic flux and B_0 is the vacuum toroidal magnetic field strength at the major radius R_0, see [Hinton and Hazeltine, 1976]. By defining $\rho_{\text{tor,B}}$ as ρ_{tor} on the LCFS, a dimensionless flux label ρ can be introduced, given by

$$\rho = \frac{\rho_{\text{tor}}}{\rho_{\text{tor,B}}} \tag{2.1}$$

The flux-surface average of a quantity Q is defined as $\langle Q \rangle = \frac{\partial}{\partial V} \int Q \, dV$ (see e.g. [Pereverzev and Yushmanov, 2002]). We assume a quasi-neutral plasma with a constant effective charge $Z_{\text{eff}} = 1$, so consisting of hydrogen (isotopes). The methodology may be extended to time-varying Z_{eff} and/or additional particle species.

Electron density continuity

The evolution of the flux-surface averaged electron density $n_e(\rho, t)$ resulting from radial transport and a net source is modeled as a PDE [Hinton and Hazeltine, 1976] on the domain $\Omega = \{(t, \rho) \in \mathbb{R} \mid t_0 \leq t \leq t_{\text{f}},\ 0 \leq \rho \leq \rho_{\text{e}}\}$, where the constant $\rho_{\text{e}} > 1$ represents the location of the scrape-off layer edge and t_0 and t_{f} represent the start and end time. The PDE is written as

$$\frac{1}{V'} \frac{\partial}{\partial t} (n_e V') + \frac{1}{V'} \frac{\partial \Gamma}{\partial \rho} = S \tag{2.2}$$

where $\Gamma(\rho, t)$ is the radial electron transport flux, $S(\rho, t)$ is the net electron source and $V' = \frac{\partial V}{\partial \rho}$ with $V(\rho)$ the volume enclosed by a flux surface. Strictly speaking, ρ_{tor} is not defined outside the LCFS due to the open field lines. However, we choose to artificially prolong ρ up to ρ_{e} and we set $\nabla\rho|_{1<\rho\leq\rho_e} := \nabla\rho|_{\rho=1}$ and $V'|_{1<\rho\leq\rho_e} := V'|_{\rho=1}$.

Radial plasma particle flux

The radial electron flux $\Gamma(\rho, t)$ is governed by diffusion and a drift (pinch) velocity [Hinton and Hazeltine, 1976; Zabolotsky et al., 2006] and is given by

$$\Gamma = -V' \left(G_1 D \frac{\partial n_e}{\partial \rho} + G_0 \nu n_e \right) \tag{2.3}$$

where D and ν are the coefficients of diffusion and drift (pinch), and $G_1 = \left\langle (\nabla\rho)^2 \right\rangle$, $G_0 = \langle |\nabla\rho| \rangle$ and $\langle |\nabla\rho| \rangle = \langle |\nabla\psi| \rangle \left(\frac{\partial \psi}{\partial \rho} \right)^{-1}$ are geometrical parameters that depend on the $\psi(R, Z)$ equilibrium [Hinton and Hazeltine, 1976]. The values for D and ν are estimated to represent the empirical system behaviour.

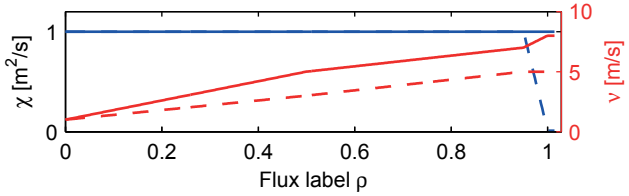

Figure 2.2 – Modeled diffusion D (blue) and drift velocity ν (red) coefficients as a function of ρ. Solid and dashed lines indicate the coefficients for low confinement ($c_{\mathrm{H}} = 0$) and high confinement ($c_{\mathrm{H}} = 1$), respectively.

Thus, $D(\rho, c_{\mathrm{H}})$ and $\nu(\rho, I_{\mathrm{p}}, c_{\mathrm{H}})$ are chosen as simple functions of ρ and c_{H}, and it is assumed that $\nu = \nu_0 \frac{I_{\mathrm{p}}}{I_{p,0}}$ to represent the increase of pinch at higher current, where $I_{p,0}$ is the *nominal* plasma current, being the programmed flat-top current. An H-mode implies a reduction of transport in the plasma edge [Willensdorfer et al., 2013] and is reproduced by lower edge diffusion and a lower drift velocity for $c_{\mathrm{H}} = 1$. In Figure 2.2, the chosen functions $D(\rho, c_{\mathrm{H}})$ and $\nu(\rho, I_{p,0}, c_{\mathrm{H}})$ are depicted for both L- and H-mode.

Domain and boundary conditions

The domain edge ρ_{e} is chosen as $\rho_{\mathrm{e}} = 1 + \lambda_{\mathrm{SOL}}$ where the dimensionless scrape-off layer width λ_{SOL} is assumed to be constant and estimated a priori as $\lambda_{\mathrm{SOL}} = \sqrt{D|_{\rho=1, c_{\mathrm{H}}=0} \pi R_0 q_{95} c_s^{-1}}$ [Stangeby, 2000; Wesson, 2004], where q_{95} is the *nominal* edge safety factor at 95% of the normalized poloidal flux and c_s is the ion velocity at *nominal* scrape-off layer temperature. At TCV and ASDEX Upgrade, this is 50keV. The boundary conditions are $\left.\frac{\partial n_e}{\partial \rho}\right|_{\rho=0} = 0$ and $n_e|_{\rho=\rho_{\mathrm{e}}} = 0$. The outflux at the domain edge $\Gamma|_{\rho=\rho_{\mathrm{e}}}$ is treated as a source to the vacuum inventory.

Sources

In our model the source is composed of four parts and is written as

$$S = S_{\mathrm{inj}} + S_{\mathrm{iz}} - S_{\mathrm{rec}} - S_{\mathrm{SOL}\to\mathrm{wall}} \tag{2.4}$$

These four contributions are depicted in Figure 2.1 and are modeled as follows.

- The electron source of ionization of injected neutrals from NBI and pellets is modeled by their particle deposition locations, and is given by

$$S_{\mathrm{inj}} = \Lambda_{\mathrm{NBI}}(\rho)\,\Gamma_{\mathrm{NBI}}(t) + \Lambda_{\mathrm{pellet}}(\rho)\,\Gamma_{\mathrm{pellet}}(t) \tag{2.5}$$

where Γ_{NBI} and Γ_{pellet} are the NBI and pellet injection fuelling rates. The functions $\Lambda_{\mathrm{NBI}}(\rho)$ and $\Lambda_{\mathrm{pellet}}(\rho)$ model the spatial deposition of the ionization of injected neutrals, with $\int_{V_\mathrm{p}} \Lambda_{\mathrm{NBI}} dV = \int_{V_\mathrm{p}} \Lambda_{\mathrm{pellet}} dV = 1$ such that $\int_{V_\mathrm{p}} S_{\mathrm{inj}} dV = \Gamma_{\mathrm{NBI}} + \Gamma_{\mathrm{pellet}}$, where $V_\mathrm{p} = \int_0^{\rho_\mathrm{e}} V' d\rho$ is the plasma volume.

- The electron source thermal ionization of other neutrals equals $\langle \sigma v \rangle_{\mathrm{iz}} n_n n_e$ where $\langle \sigma v \rangle_{\mathrm{iz}}(T_\mathrm{e})$ is the ionization cross-section [Wesson, 2004] and n_n is the neutral density, but is approximated as

$$S_{\mathrm{iz}} = \langle \sigma v \rangle_{\mathrm{iz}}(T_{\mathrm{e,b}}) \Lambda_{\mathrm{iz}} \frac{N_\mathrm{v}}{V_\mathrm{v}} n_e \tag{2.6}$$

  where $T_{\mathrm{e,b}} = T_\mathrm{e}|_{\rho=1}$ is the LCFS electron temperature, N_v is the vacuum inventory, $V_\mathrm{v} = V_\mathrm{r} - V_\mathrm{p}$ is the vacuum volume and V_r is the vessel volume. The function $\Lambda_{\mathrm{iz}}(\rho, c_\mathrm{D})$ models the product of the spatial distribution of the neutral density and the ionization cross-section such that $\langle \sigma v \rangle_{\mathrm{iz}}(T_{\mathrm{e,b}}) \Lambda_{\mathrm{iz}} \frac{N_\mathrm{v}}{V_\mathrm{v}} \approx \langle \sigma v \rangle_{\mathrm{iz}}(T_\mathrm{e}) n_n$.

- The thermal recombination sink of ions equals $\langle \sigma v \rangle_{\mathrm{rec}} n_e n_i$ where $\langle \sigma v \rangle_{\mathrm{rec}}(T_\mathrm{e})$ is the recombination cross-section [Wesson, 2004] and n_i is the ion density, but is approximated as

$$S_{\mathrm{rec}} = \langle \sigma v \rangle_{\mathrm{rec}}(T_{\mathrm{e,b}}) \Lambda_{\mathrm{rec}} n_e^2 \tag{2.7}$$

  The function $\Lambda_{\mathrm{rec}}(\rho)$ models the spatial distribution of the recombination cross-section such that $\langle \sigma v \rangle_{\mathrm{rec}}(T_{\mathrm{e,b}}) \Lambda_{\mathrm{rec}} \approx \langle \sigma v \rangle_{\mathrm{rec}}(T_\mathrm{e})$.

- The particle sink in the scrape-off layer due to wall impact of particles exiting the plasma through the scrape-off layer is modeled as

$$S_{\mathrm{SOL}\to\mathrm{wall}} = \frac{H(\rho - 1) n_e}{\tau_{\mathrm{SOL}}} \tag{2.8}$$

  where $H(\cdot)$ is the Heaviside function and $\tau_{\mathrm{SOL}}(c_\mathrm{D})$ is the time constant for particle loss through the scrape-off layer [Stangeby, 2000], modeled as

$$\tau_{\mathrm{SOL}} = \begin{cases} \pi R_0 q_{95} c_s^{-1} & \text{if } c_\mathrm{D} = 0 \\ g_\mathrm{d} \pi R_0 q_{95} c_s^{-1} & \text{if } c_\mathrm{D} = 1 \end{cases}$$

  where $g_\mathrm{d} > 1$ is used to model the reduction of net outflow to the wall in a diverted plasma.

The functions Λ_{iz}, Λ_{rec}, Λ_{NBI} and $\Lambda_{\mathrm{pellet}}$ are chosen ad-hoc in this study, see Figure 2.3, but could be computed using more detailed physics models of e.g. neutral beam injection [Feng et al., 1995; Pankin et al., 2004]. The width of $\Lambda_{\mathrm{iz}}(\rho, c_\mathrm{D})$ is decreased for $c_\mathrm{D} = 1$ to model the decreased ionization depth experienced in a diverted plasma, where the main plasma is located farther from the wall components due to flux expansion.

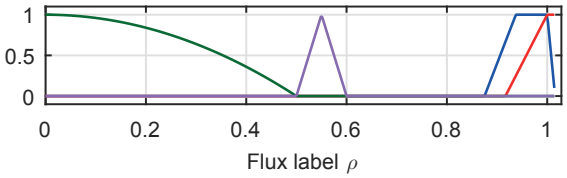

Figure 2.3 – Example of spatial distributions Λ_{iz} (blue), Λ_{rec} (red), Λ_{NBI} (green) and $\Lambda_{\mathrm{pellet}}$ (magenta) for a limited plasma.

2.2.2 0D model of the neutral wall inventory

All particles in the tokamak that are not in the plasma are either assigned to the wall inventory $N_{\mathrm{w}}(t)$ or the neutral vacuum inventory $N_{\mathrm{v}}(t)$. The wall inflow is formed by the scrape-off layer sink $S_{\mathrm{SOL}\rightarrow\mathrm{wall}}$ and the outflow is denoted by $\Gamma_{\mathrm{recycle}}(t)$, see Figure 2.1. The wall particle inventory balance is given by

$$\frac{dN_{\mathrm{w}}}{dt} = \Gamma_{\mathrm{SOL}\rightarrow\mathrm{wall}}(t) - \Gamma_{\mathrm{recycle}}(t) \tag{2.9}$$

where $\Gamma_{\mathrm{SOL}\rightarrow\mathrm{wall}} = \int_{V_{\mathrm{p}}} S_{\mathrm{SOL}\rightarrow\mathrm{wall}} dV$. The wall recycling outflow $\Gamma_{\mathrm{recycle}}(t)$ is modeled by a linear term representing outward diffusion of particles embedded in the wall material and a term representing particle expulsion due to impacting plasma particles. Hereby, the latter outflow matches the inflow from the scrape-off layer if the wall inventory N_{w} approaches the saturation level N_{sat}, and is given by

$$\Gamma_{\mathrm{recycle}} = \frac{N_{\mathrm{w}} - c_w V_{\mathrm{v},0} V_{\mathrm{v}}^{-1} N_{\mathrm{v}}}{\tau_{\mathrm{release}}} + \frac{N_{\mathrm{w}}}{N_{\mathrm{sat}}} \Gamma_{\mathrm{SOL}\rightarrow\mathrm{wall}} \tag{2.10}$$

where $V_{\mathrm{v},0} = V_{\mathrm{r}} - V_{\mathrm{p},0}$ is the *nominal* vacuum volume, $V_{\mathrm{p},0}$ is the *nominal* plasma volume and τ_{release} is a time constant for the decay of the wall inventory due to outward diffusion, c_w is a dimensionless constant that determines the steady-state balance between the wall inventory and vacuum density, and $N_{\mathrm{sat}}(c_{\mathrm{D}}, c_{\mathrm{H}})$ is the saturation level of the wall inventory, modeled as

$$N_{\mathrm{sat}}(c_{\mathrm{D}}, c_{\mathrm{H}}) = \begin{cases} N_{\mathrm{sat},0} & \text{if } c_{\mathrm{D}} = 0,\ c_{\mathrm{H}} = 0 \\ N_{\mathrm{sat,D}} & \text{if } c_{\mathrm{D}} = 1,\ c_{\mathrm{H}} = 0 \\ N_{\mathrm{sat,H}} & \text{if } c_{\mathrm{D}} = 1,\ c_{\mathrm{H}} = 1 \end{cases}$$

where $N_{\mathrm{sat,D}} > N_{\mathrm{sat},0}$ to model the absorption of particles by the wall when the plasma is diverted and $N_{\mathrm{sat,H}} < N_{\mathrm{sat,D}}$ to model the expulsion of wall particles when the plasma enters an H-mode [Willensdorfer et al., 2012]. The coefficients $N_{\mathrm{sat},0}$, $N_{\mathrm{sat},0}$, $N_{\mathrm{sat},0}$, $\tau_{release}$ and c_{wv} are difficult to obtain from data, since no diagnostics exist to measure the wall inventory, and retention and recycling depend on the wall conditioning. However, they can be estimated using studies that identify retention [Rohde et al., 2009a,b].

2.2.3 0D model of the neutral vacuum inventory

The particle inflows to the vacuum are the thermal recombination S_{rec}, wall recycling outflow $\Gamma_{\mathrm{recycle}}$ and gas injection Γ_{valve}, see Figure 2.1. We also include the plasma outflux at the domain edge $\Gamma|_{\rho=\rho_{\mathrm{e}}}$. The outflows from the vacuum are the ionization S_{iz} and the (cryo)pump outflow Γ_{pump}. The vacuum particle inventory balance is given by

$$\frac{dN_{\mathrm{v}}}{dt} = \Gamma_{\mathrm{rec}}(t) - \Gamma_{\mathrm{iz}}(t) + \Gamma|_{\rho=\rho_{\mathrm{e}}} + \Gamma_{\mathrm{recycle}}(t) + \Gamma_{\mathrm{valve}}(t) - \Gamma_{\mathrm{pump}}(t) \quad (2.11)$$

where $\Gamma_{\mathrm{rec}} = \int_{V_{\mathrm{p}}} S_{\mathrm{rec}} dV$ and $\Gamma_{\mathrm{iz}} = \int_{V_{\mathrm{p}}} S_{\mathrm{iz}} dV$. The (cryo)pump outflow $\Gamma_{\mathrm{pump}}(t)$ is assumed to be proportional to the neutral density and is given by

$$\Gamma_{\mathrm{pump}} = \frac{N_{\mathrm{v}} V_{\mathrm{v},0}}{\tau_{\mathrm{pump}} V_{\mathrm{v}}} \quad (2.12)$$

where τ_{pump} is a time scale that expresses exponential decay of the neutral density due to pumping, which may depend on the number of pumps used and the strike point positions.

2.2.4 Inputs

The gas inflow rate $\Gamma_{\mathrm{valve}}(t)$, NBI fuelling rate $\Gamma_{\mathrm{NBI}}(t)$ and pellet fuelling rate $\Gamma_{\mathrm{pellet}}(t)$ are considered as inputs to the system. They are constrained to be nonnegative and have upper limits, expressed as

$$0 \leq \Gamma_{\mathrm{valve}}(t) \leq \Gamma_{\mathrm{valve}}^{\mathrm{max}} \quad (2.13)$$

$$0 \leq \Gamma_{\mathrm{NBI}}(t) \leq \Gamma_{\mathrm{NBI}}^{\mathrm{max}} \quad (2.14)$$

We assume that the gas inflow rate $\Gamma_{\mathrm{valve}}(t)$ is either proportional to the actuator input signal, or that the gas valve is feedback controlled to provide the flow $\Gamma_{\mathrm{valve}}(t)$. The pellet injection fuelling rate $\Gamma_{\mathrm{pellet}}(t)$ is a pulsed signal which takes on either zero or $\Gamma_{\mathrm{pellet}}^{\mathrm{max}}$. Each pulse represents the arrival of an individual pellet and the time integral of each pulse equals the number of deposited electrons.

2.2.5 External input parameter

The coefficients of the model change in time due to a variety of external factors. These are modeled by a time-varying external input parameter $p(t)$, defined as

$$p = \begin{bmatrix} c_{\mathrm{D}} & c_{\mathrm{H}} & T_{\mathrm{e,b}} & I_{\mathrm{p}} & V' & G_1 & G_0 & \Omega \end{bmatrix} \quad (2.15)$$

where $T_{\mathrm{e,b}} = T_{\mathrm{e}}|_{\rho=1}$ is the electron temperature at the LCFS, Ω is a matrix that links the density profile to the diagnostic outputs and is introduced in Section 2.2.8, and V', G_1, G_0, and Ω are determined from an equilibrium $\psi(R, Z)$.

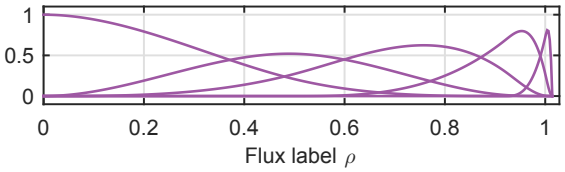

Figure 2.4 – Example of basis functions $\Lambda_\alpha(\rho)$, $\alpha = 1, 2, ..., m$ with $m = 5$ used to spatially discretize the electron density (2.16).

We assume that the parameter values are available through real-time equilibrium reconstruction (see e.g. [Blum et al., 2012; Ferron et al., 1998; Moret et al., 2015]) and/or diagnostics.

2.2.6 Spatial discretization using finite elements

The numerical solution of (2.2), (2.9) and (3.14) is implemented using a finite element method (see e.g. [Hughes, 1987]) for the spatial discretization similar to [Felici and Sauter, 2012] and a trapezoidal method for the time discretization. The methodology describing the use of finite elements and the time discretization are discussed in detail in 2.A and 2.B respectively, but a brief outline is given here.

First, the electron density is approximated as

$$n_e(\rho, t) = \sum_{\alpha=1}^{m} \Lambda_\alpha(\rho)\, b_\alpha(t) \tag{2.16}$$

where the basis functions $\Lambda_\alpha : [0, \rho_e] \to [0, 1]$, $\alpha = 1, 2, ..., m$ are chosen as cubic B-splines with finite support [de Boor, 2001]. B-splines are continuous and differentiable piecewise polynomials on a finite domain [de Boor, 2001]. An example set of basis functions is shown in Figure 2.4. The variables $b(t) = \begin{bmatrix} b_1(t) & \cdots & b_m(t) \end{bmatrix}^T$ are the time-varying spline coefficients. For the purpose of control-oriented modeling, a small number of basis functions ($m = 5$) with closely-spaced spline knots around the plasma edge is chosen. The boundary conditions discussed in Subsection 2.2.1 are imposed by restricting the values and derivatives of the basis functions at the boundaries.

Second, an equidistant time discretization $t_k = t_0 + kT_s$, $k = 0, 1, ..., N$ is chosen, where $T_s > 0$ is the time step and $N = (t_f - t_0)/T_s$.

Finally, applying the finite element method and the trapezoidal time discretization on (2.2), (2.9) and (3.14) as described in 2.A and 2.B yields the system of nonlinear discrete-time ODEs

$$x_k = f_d(p_{k-1}, x_{k-1}) + B_d(p_{k-1})\, u_{k-1} \tag{2.17}$$

where $p_k = p(t_k)$, and the state $x_k \in \mathbb{R}^{n_x}$ and the input $u_k \in \mathbb{R}^{n_u}$ are defined as

$$x_k = \begin{bmatrix} b(t_k) \\ N_{\mathrm{w}}(t_k) \\ N_{\mathrm{v}}(t_k) \end{bmatrix} \quad u_k = \begin{bmatrix} \Gamma_{\mathrm{valve}}(t_k) \\ \Gamma_{\mathrm{NBI}}(t_k) \\ \Gamma_{\mathrm{pellet}}(t_k) \end{bmatrix}$$

with $n_x = m + 2$ and $n_u = 3$. Because of the products of n_e, N_{w} and N_{v} in (2.6), (2.7) and (2.10), $f_{\mathrm{d}}(p_k, x_k)$ is a nonlinear function of x_k.

2.2.7 Interferometry measurements

The interferometry output signal is proportional to the line-integrated electron density along a laser chord intersecting the plasma (see e.g. [Hutchinson, 2002]). Multiple chords with different line of sight through the plasma allow to infer the electron density profile. The interferometry phase signal $\Delta\phi$ of the c-th chord at the sampling time instant t_k is denoted by $\Delta\phi_k^c \in \mathbb{R}$ and is given by

$$\Delta\phi_k^c = c_{\mathrm{FIR}} \int_{L_c} n_e\left(\rho\left(\psi\left(R, Z\right)\right), t_k\right) dL \tag{2.18}$$

where L_c is the intersection length of the plasma and the c-th laser chord, and the interferometry constant is given by $c_{\mathrm{FIR}} = \lambda e^2 / \left(4\pi\epsilon_0 m_e c^2\right)$ where λ is the laser wavelength, e is the electron charge, ϵ_0 is the the permittivity of vacuum, m_e is the electron rest mass and c is the speed of light.

Modeling fringe jumps

Fringe jumps are counting errors of the interferometry phase difference $\Delta\phi$ and form infrequent jumps at individual output channels. While fringe jumps are infrequent, their magnitude is sufficiently large to disturb density estimates and reconstructions. The jump magnitude in the phase signal equals an integer multiple of 2π, i.e. $2\pi k, k \in \mathbb{N}$. By incorporating a description of fringe jumps in the measurement, (2.18) is replaced by

$$\Delta\phi_k^c = c_{\mathrm{FIR}} \int_{L_c} n_e\left(\rho\left(\psi\left(R, Z\right), t_k\right)\right) dL + 2\pi d_k^c \tag{2.19}$$

$$d_k^c = d_{k-1}^c + \Delta_{k-1}^c \tag{2.20}$$

where $d_k^c \in \mathbb{N}$ is the cumulative number of fringe jumps on chord c at time t_k and $\Delta_{k-1}^c \in \mathbb{N}$ is a stochastic variable that represents possibly multiple jumps on chord c between time t_{k-1} and t_k.

The probability of jumps is known to be strongly correlated with fast changes of the plasma density [Gil et al., 2010; Mlynek et al., 2011], but obtaining the probability density function for Δ_k^c as a function of (the time derivative of) the plasma density is beyond the scope of this paper. For the present purposes, it is assumed that initially $d_1^c = 0$ and that the expected value $\mathbb{E}\left[\Delta_k^c\right] = 0$.

2.2.8 Synthetic output equation

The measurement output vector of all n_{FIR} available interferometry chords can, by stacking (2.19), be represented as $y_k \in \mathbb{R}^{n_{\text{FIR}}}$ and is given by

$$y_k = \begin{bmatrix} \int_{L_1} n_e(\rho, t_k)\, dL \\ \vdots \\ \int_{L_{n_{FIR}}} n_e(\rho, t_k)\, dL \end{bmatrix} + \delta d_k \tag{2.21}$$

where $\delta = 2\pi c_{\text{FIR}}^{-1}$ and $d_k = \begin{bmatrix} d_k^1 & \cdots & d_k^{n_{\text{FIR}}} \end{bmatrix}^T \in \mathbb{N}^{n_{\text{FIR}}}$ is the column of the cumulative number of fringe jumps on all chords at time t_k. The fringe jump state equation of all chords is given by

$$d_k = d_{k-1} + \Delta_{k-1} \tag{2.22}$$

where $\Delta_k = \begin{bmatrix} \Delta_k^1 & \cdots & \Delta_k^{n_{\text{FIR}}} \end{bmatrix}^T \in \mathbb{N}^{n_{\text{FIR}}}$.

The numerical evaluation of the line integrals is discussed in 2.C. The spatial discretization (2.16) and an equilibrium $\psi(R, Z)$ allow to express the line integrals in (2.21) as a linear combination of the electron density spline coefficients b_k from (2.16). By evaluating the line integrals, the synthetic output equation is written as

$$y_k = C(p_k)\, x_k + \delta d_k \tag{2.23}$$

where $C(p_k) = \begin{bmatrix} \Omega(p_k) & 0^{n_{\text{FIR}} \times 2} \end{bmatrix}$ and $\Omega(p_k)$ is given by

$$\Omega_{ij}(p_k) = \int_{L_i} \Lambda_j(\rho(\psi(R, Z)))\, dL \tag{2.24}$$

It is assumed that $\rho(\psi)$ and $\psi(R, Z)$ are known from real-time 2D equilibrium reconstruction (see [Blum et al., 2012; Ferron et al., 1998; Moret et al., 2015]).

2.2.9 Computational time requirements

For real-time control, the sampling interval must be at least an order of magnitude smaller than the particle confinement time. On TCV, the particle confinement time τ_p is at least 10ms [Weisen et al., 1996]. The sampling frequency of the density feedback controller is 1ms on TCV [Paley et al., 2010] and 1.5ms on ASDEX Upgrade [Mlynek et al., 2011], which is slower than the respective interferometer sampling frequencies [Barry, 1999; Boboc et al., 2010; Mlynek, 2010]. Note that typically, the controller bandwidth used at TCV is below 25Hz [Vijvers et al., 2012]. Currently, Thomson scattering measurements of the electron density are not available in real time on TCV and ASDEX Upgrade. The time resolution of Thomson scattering is limited by the repetition rate of the laser. The repetition rate is in itself typically too low for feedback control, but

real-time Thomson scattering measurements may be used to correct the interferometry signals and enhance profile reconstruction.

TCV has a total of 14 interferometry chords, while ASDEX Upgrade has 6 chords. Presently, the evaluation of (2.17) and (2.23) with $n_x = 7$ and $n_{FIR} = 14$ and $T_s = 1$ms, for which details are given in 2.A through 2.C, takes 2ms of computational time. Here, MATLAB using an Intel®Core™2 DUO E6600 at 2.40 GHz PC running Windows 7 was used. On TCV, the energy confinement time τ_e is between 2ms and 50ms [Kirneva et al., 2015; Pochelon et al., 1999; Weisen et al., 1997] and the particle confinement time τ_p from $5\tau_e$ up to $10\tau_e$ [Weisen et al., 1996]. Implementation on a tokamak control system can easily reduce the computational time to below a cycling time of 1ms, satisfying the required time resolution.

2.2.10 TCV and ASDEX Upgrade simulation: qualitative model validation

To validate the model, we present simulations of the model and compare them with measurement data from TCV and ASDEX Upgrade.

First we use the parameter signals, equilibrium reconstruction and gas valve input signal from TCV shot #45109 as a test case to simulate a TCV discharge. The model coefficients are chosen to be representative for a typical discharge in the TCV tokamak. In Figure 2.5, the simulated density with Thomson scattering measurements are shown. The plasma is diverted at $t = 0.25$s and enters a high confinement mode around $t = 0.5$s. Note that the Thomson scattering data is mapped to ρ_{tor} loci using an (offline) equilibrium. The errorbars represent the sample standard deviation of binned data, in bins with a $\rho_{\text{tor}} = 0.05$ width and covering three consecutive time points.

The simulation replicates the measurement with reasonable similarity. The decay of plasma density after the plasma is diverted is not accurately followed: the model assumes an instantaneous change of configuration and transport, whereas the evolution of the strike point location towards their stationary location takes longer. The decay of plasma density therefore takes longer than modeled. Similarly, the rise of plasma density during the low to high confinement mode transition is not accurately followed: again, the model assumes and instantaneous change of transport dynamics, whereas the low to high confinement transition is a more complex process. There is a good agreement before 1.6sbetween the Thomson scattering measurements and the simulated density profiles (Fig. 2.5(c)). After 1.6s, the measured density increases, while the simulated density does not, see Fig. 2.5(b). Here, the model simulation shows a slight decay of the plasma density which is caused by the decreasing plasma current and increasing plasma volume. It is not clear what causes the increase of the measured density, nor what needs to be modeled to reproduce such behaviour with the model. Note that the wall retention model (2.10) is a severe simplifica-

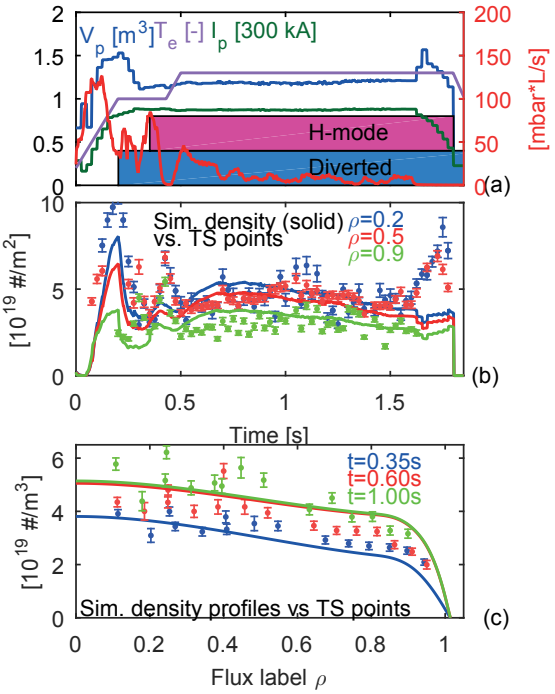

Figure 2.5 – Nominal simulation of TCV plasma using plasma parameters and the mass flow of the gas puff (in red) signal from TCV shot #45109 (a). The plasma current is normalized to 300kA. The simulated density time traces and Thomson scattering points at three loci of ρ_{tor} are shown in (b). The simulated density profiles with Thomson scattering points at three time points are shown in (c). Note that error bars are provided with the Thomson scattering data; these represent the sample standard deviation of the data.

tion of reality. It is challenging to estimate the coefficients N_{sat} and c_{wv} a priori to predict the absolute value of the plasma density and the wall inventory, both transiently and in flat-top for various discharge scenarios.

Second, we use the parameter signals, equilibrium reconstruction and input signals from ASDEX Upgrade shot #32527 as a test case to simulate an ASDEX Upgrade discharge. The model coefficients are now chosen to be representative for a standard H-mode discharge in ASDEX Upgrade. Note that the wall saturation inventory $N_{\mathrm{sat,H}}$ was taken as 1.8×10^{22} atoms, as was also identified for ASDEX Upgrade H-mode discharges [Rohde et al., 2009a]. In Figure 2.6, the simulated plasma density, plasma inventory and wall inventory are shown and compared to interferometry and Thomson scattering measurements. The plasma is diverted at $t = 0.5$s and enters a high confinement mode around $t = 1.8$s. Note

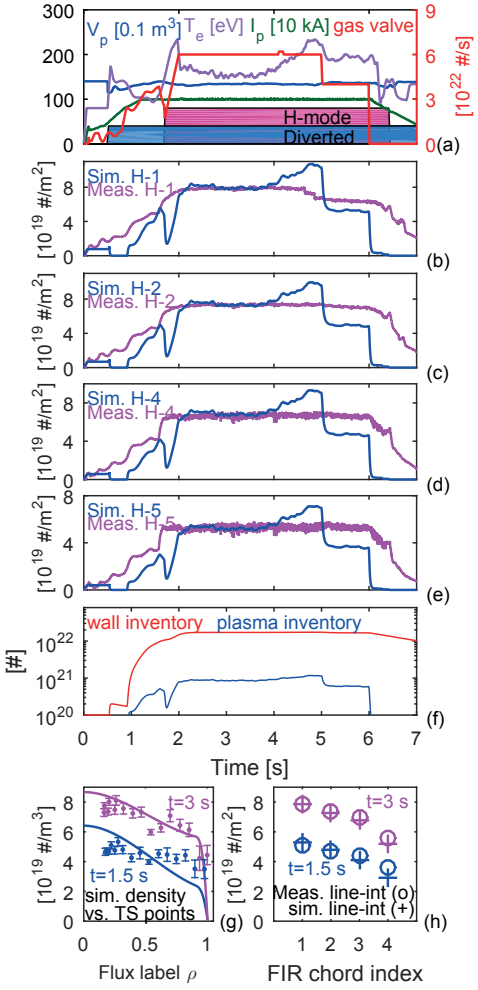

Figure 2.6 – Nominal simulation of an AUG plasma using equilibrium and input data from AUG shot #32527 (a). The simulated line-integrated density (solid) and measurements from AUG shot #32527 (dashed) are shown in (b),(c),(d) and (e) for four interferometer chords. The simulated wall inventory and plasma inventory are shown in (c). The simulated density profiles at $t = 1.5$s and $t = 3$s are shown in (g), together with Thomson scattering measurements. The line-integrated densities and interferometry measurements at $t = 1.5$s and $t = 3$s are shown in (h).

that the Thomson scattering data is mapped to ρ_{tor} loci using an offline available equilibrium.

Here, the simulation replicates the interferometry and Thomson scattering measurements best during the high confinement mode. During ramp-up, the density is not well replicated. Since the plasma particle inventory is small compared to the total integrated valve inflow in ASDEX Upgrade [Rohde et al., 2009a,b], the simulated plasma density is very sensitive to the chosen model equations. Predominantly the wall and pumping models (2.10),(2.12) play a large role in the evolution of the plasma density. After $t = 4$s, the simulated plasma density starts to increase with respect to the interferometry measurements due to an increase of the temperature and later drops following the closing of the gas valve. Here, the ionization source model incorporates the known temperature dependency on the ionization rate, see equation (2.6). In the current formulation of the model, particularly the particle flows outside the main plasma, it is challenging to reproduce the insensitivity of the plasma density to the partial closing of the gas valve around $t = 5$s, which is attributed to inefficient fueling in the high-temperature H-mode. In the future, we would like to include this effect in a self-consistent real-time capable model. This will require better modeling of the ionization distribution, particle losses in the scrape-off layer and the particle recycling flows. The density profile at $t = 3$s is replicated with good accuracy and shows the pedestal typically seen in high confinement plasmas. Both the simulated profile and simulated synthetic interferometer line-integrated density signals show at $t = 3$s match with the Thomson scattering measurements and the interferometer data, respectively.

Although self-consistent modeling and simulation of a complete discharge on two tokamaks is challenging, we emphasize that the ability of the model to produce smooth density profiles is highly valuable for the reconstruction algorithm discussed in the next section.

2.3 Dynamic state observer design using Kalman filtering

In this section, the problem of reconstructing the density profile as well as modeling errors/disturbances in real-time is addressed. Here, we will use our knowledge of the process captured in the model, as introduced in Section 2.2, to complement real-time diagnostics.

We begin this section by introducing the basic working of an observer applied to the density reconstruction problem. Next, a solution to compensate for systematic modeling errors is shown. Subsequently, the observer equations and a method for detecting fringe jumps within the observer from characteristics of this type of sensor error are described. Next, the tuning possibilities and reconstruction tradeoffs of the observer are discussed. At the end of this section,

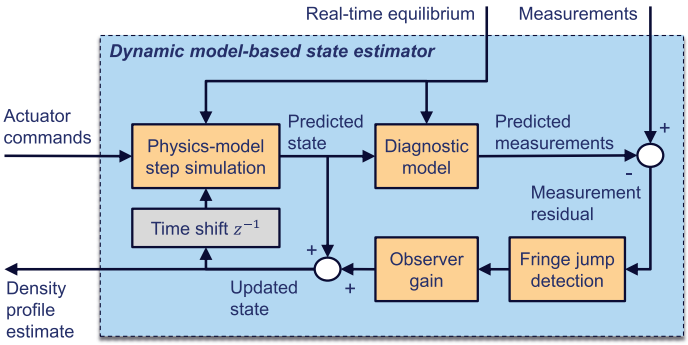

Figure 2.7 – Block diagram of the dynamic state estimator. The state estimator combines measurements with a model to reconstruct the density profile in real-time, to be used for feedback control of the density. We detect fringe jumps from the difference between measurements and model-based predictions of the measured quantities.

tests of the observer density reconstruction based on simulated data, as well as reconstructions using experimental data are presented.

The dynamic state observer, or Kalman filter [Anderson and Moore, 1979], is a tool widely used in the systems & control community [Moreno and Pigazo, 2009] for estimating the internal state of a dynamical system in real-time by combining measurements with a model of the system. While a Kalman filter is a minimum-variance estimator for linear dynamical systems, an Extended Kalman filter (EKF) is a linearized, and therefore *sub-optimal* version of the Kalman filter for nonlinear dynamical systems [Anderson and Moore, 1979]. No guarantees can be given about the stability and estimation accuracy of the EKF, but it is considered the *de facto* standard for estimation of nonlinear systems and is widely used [Moreno and Pigazo, 2009]. We apply the EKF to estimate the density profile and modeling errors/disturbances in real-time with interferometry diagnostics (2.18). More specifically, the EKF iteratively produces estimates $\hat{x}_{k|k}$ of the system state x_k at every measurement sample y_k using the state estimate at the previous time step $\hat{x}_{k-1|k-1}$. A block scheme of the proposed dynamic state observer is depicted in Figure 2.7. At every iteration of the EKF, a one-sample ahead prediction is made based on the nonlinear model (2.17), (2.22) and a forward diagnostics model (2.23) given a state estimate at the previous time step. The state estimate is updated with information from the measurement sample y_k.

The control-oriented model (2.17), (2.22), (2.23) is augmented with an additive random-walk state disturbance to represent modeling errors, similar to [Felici et al., 2014a]. This allows the observer to effectively estimate modeling

errors in real-time as systematic differences between measurements and model-based predictions of the measured quantities. The advantage of this method over adapting the model coefficients is that the observer equations remain stable, whereas adaptive parameter estimation methods [Mechoud et al., 2013; Xu et al., 2010] introduce extra nonlinearity and may be unstable depending on the chosen time step.

2.3.1 Extended Kalman filter for estimation of state and disturbances

In this subsection, the Extended Kalman filter (EKF) [Anderson and Moore, 1979] including a state disturbance model is described.

In order to derive the EKF equations we need to model stochastic behavior of our system (2.17), (2.23) with associated covariance matrices. First, the diagnostics noise is represented by an additive zero-mean white measurement noise v_k with covariance matrix R_k on the output y_k. Furthermore, uncertainty on the evolution of the density, wall inventory and vacuum inventory is modeled as an additive zero-mean process noise w_k^x with covariance matrix Q_k^x on the state x_k. Finally, additive unknown disturbances $\zeta_k \in \mathbb{R}^m$ are modeled on the plasma density state equation. These disturbances are assumed to be constant $\zeta_{k+1} = \zeta_k$. For estimating these disturbance in the EKF, a white noise signal is added to the evolution equation, yielding $\zeta_{k+1} = \zeta_k + w_k^\zeta$ where w_k^ζ is a zero-mean white noise with covariance matrix Q_k^ζ.

By including these noises and disturbances in our system (2.17), (2.22), (2.23), the augmented system is written as

$$
\begin{aligned}
x_k &= f_\mathrm{d}\left(p_{k-1}, x_{k-1}\right) + B_\zeta \zeta_{k-1} + B_\mathrm{d} u_{k-1} + w_{k-1}^x && (2.25)\\
\zeta_k &= \zeta_{k-1} + w_{k-1}^\zeta && (2.26)\\
d_k &= d_{k-1} + \Delta_{k-1} && (2.27)\\
y_k &= C\left(p_k\right) x_k + \delta d_k + v_k && (2.28)
\end{aligned}
$$

where B_ζ is chosen as $B_\zeta = \begin{bmatrix} I^{m\times m} & 0^{m\times 2} \end{bmatrix}^T$ such that each disturbance entry influences one variable of the electron density. Let us define the augmented state $\boldsymbol{x}_k \in \mathbb{R}^{n_x+m}$ as $\boldsymbol{x}_k = \begin{bmatrix} x_k^T & \zeta_k^T \end{bmatrix}^T$ and

$$
F_k = \begin{bmatrix} \left.\frac{\partial f_\mathrm{d}}{\partial x_k}\right|_{p_k, \hat{x}_{k|k}} & B_\zeta \\ 0 & I^{m\times m} \end{bmatrix} \quad G = \begin{bmatrix} B_\mathrm{d} \\ 0 \end{bmatrix}
$$

$$
H_k = \begin{bmatrix} C\left(p_k\right) & 0 \end{bmatrix} \quad Q_k = \begin{bmatrix} Q_k^x & 0 \\ 0 & Q_k^\zeta \end{bmatrix}
$$

The EKF equations for the system (2.25)-(2.28) consist of a prediction and an update step. First, the predicted augmented state $\hat{\boldsymbol{x}}_{k|k-1}$, the predicted

fringe jump state $\hat{d}_{k|k-1}$ are based on a forward evaluation of the dynamics (2.25)-(2.27) given the state estimates at the previous time step and are given by

$$\hat{\boldsymbol{x}}_{k|k-1} = \begin{bmatrix} f_{\mathrm{d}}\left(p_{k-1}, \hat{x}_{k-1|k-1}\right) \\ \hat{\zeta}_{k-1|k-1} \end{bmatrix} + G u_{k-1} \tag{2.29}$$

$$\hat{d}_{k|k-1} = \hat{d}_{k-1|k-1} \tag{2.30}$$

The covariance matrix $P_{k|k-1}$ of the prediction error of the augmented state $\boldsymbol{x}_{k|k-1}$ is given by

$$P_{k|k-1} = F_{k-1} P_{k-1|k-1} F_{k-1}^T + Q_{k-1} \tag{2.31}$$

Next, in the update step, the prediction is adjusted according the measurement sample y_k. The innovation residual is the difference between the measurement sample and the prediction of the measured quantity, and is based on the output equation (2.28). The innovation residual z_k, its covariance matrix S_k and the *near-optimal* Kalman gain L_k are given by

$$z_k = y_k - H_k \hat{\boldsymbol{x}}_{k|k-1} - \delta \hat{d}_{k|k-1} \tag{2.32}$$

$$S_k = R_k + H_k P_{k|k-1} H_k^T \tag{2.33}$$

$$L_k = P_{k|k-1} H_k^T S_k^{-1} \tag{2.34}$$

Finally, the updated estimate $\hat{\boldsymbol{x}}_{k|k}$ of the augmented state, its covariance matrix $P_{k|k}$ and the estimated fringe jump state $\hat{d}_{k|k}$ are given by

$$\hat{\boldsymbol{x}}_{k|k} = \hat{\boldsymbol{x}}_{k|k-1} + L_k \left(z_k - \delta \mathbb{E}\left[\Delta_{k-1} \mid z_k\right]\right) \tag{2.35}$$

$$\hat{d}_{k|k} = \hat{d}_{k|k-1} + \mathbb{E}\left[\Delta_{k-1} \mid z_k\right] \tag{2.36}$$

$$P_{k|k} = \left(I - L_k H_k\right) P_{k|k-1} \tag{2.37}$$

where $\mathbb{E}\left[\Delta_{k-1} \mid z_k\right]$ denotes the expected value of fringe jumps at time t_k given z_k, as discussed in the next subsection.

The EKF (2.29)-(2.37) iteratively produces estimates of the augmented state $\hat{\boldsymbol{x}}_{k|k}$, its associated covariance matrix $P_{k|k}$ and estimates of the fringe jump state $\hat{d}_{k|k}$, based on the measurements y_k, the inputs u_k and the initial values $\hat{\boldsymbol{x}}_{0|0}$ and $\hat{d}_{0|0} = 0$, where $k = 1, ..., N$. The computational speed of the EKF is dominated by (2.29). Because the EKF uses a linearization of the nonlinear dynamics (2.25) in (2.31), the expressions for the matrices $P_{k|k-1}$ (2.31), S_k (2.33) and $P_{k|k}$ (2.37) are approximations of the true covariance of the prediction error $\mathbb{E}\left[\left(\boldsymbol{x}_{k|k-1} - \hat{\boldsymbol{x}}_{k|k-1}\right)\left(\boldsymbol{x}_{k|k-1} - \hat{\boldsymbol{x}}_{k|k-1}\right)^T\right]$, the true covariance of the innovation residual $\mathbb{E}\left[z_k z_k^T\right]$ and the true covariance of the estimation error $\mathbb{E}\left[\left(\boldsymbol{x}_{k|k} - \hat{\boldsymbol{x}}_{k|k}\right)\left(\boldsymbol{x}_{k|k} - \hat{\boldsymbol{x}}_{k|k}\right)^T\right]$ respectively. No a priori guarantees can be

given about the stability and estimation accuracy of the EKF and results have to be checked a posteriori.

Note also that the fringe jump state prediction (2.30) equals its estimate at the previous time step since we do not anticipate for fringe jumps. In Section 2.3.3, the estimation tradeoffs involved with choosing the covariance matrices Q_k^x, Q_k^ζ and R_k are discussed.

Naturally, the estimated density profile can be computed using the density profile parametrization 2.16, by substituting the updated state estimate $\hat{x}_{k|k}$ in 2.16. For the results analysis in Sections 2.3.4 and 2.3.5, confidence bounds are plotted on the estimated profiles. These represent the standard deviation of the profile estimation error. They are denoted as $\sigma(\rho, t_k)$ and are computed from the a posteriori covariance matrix $P_{k|k}$ (2.37) as

$$\sigma(\rho, t_k) = \sum_{\alpha=1}^{m} \Lambda_\alpha(\rho) \sqrt{p_{\alpha,k|k}} \tag{2.38}$$

where $p_{\alpha,k|k},\ \alpha = 1, 2, .., m$ are the diagonal elements of the covariance matrix $P_{k|k}$ (2.37). Also, the updated interferometer signals are presented in the figures of Sections 2.3.4 and 2.3.5. These are the synthetic interferometer signals (2.23), evaluated using the updated estimates $\hat{x}_{k|k}$ and $\hat{d}_{k|k}$, i.e.

$$\hat{y}_{k|k} = C(p_k)\,\hat{x}_{k|k} + \delta\hat{d}_{k|k} \tag{2.39}$$

These represent the estimated measurement, based on the updated state estimates.

2.3.2 Fringe jump detection

Sensor errors can be detected from the innovation residual z_k, since it is the difference between measurements, containing the sensor errors, and the model-based prediction of the measured quantity. We choose to flag a fringe jump on the c-th interferometry channel when both the absolute value of the innovation $|z_k^c|$ exceeds a threshold and its time difference $\left|z_k^c - z_{k-1}^c\right|$ exceeds a threshold.

Since fringe jumps have a magnitude of an integer multiple of δ on an interferometry channel, the c-th channel is flagged to contain a jump if both the magnitude of the innovation $|z_k^c|$ and its time difference $\left|z_k^c - z_{k-1}^c\right|$ exceed the thresholds $\gamma\delta$ and $\kappa\delta$ respectively, where z_k^c is the c-th element of the innovation z_k. Recall from Section 2.2.7 that $\delta = 2\pi c_{\mathrm{FIR}}^{-1}$. The constants $\gamma \in (0, 1)$ and $\kappa \in (0, 1)$ set the detection sensitivity, where lower values of γ and κ increase the sensitivity, but also increase the false alarm probability. The expected value of fringe jumps at time t_k is composed of contributions of individual chords and is written as $\mathbb{E}[\Delta_{k-1} \mid \tilde{z}_k] = \mathbb{E}\left[\left[\Delta_{k-1}^1 \dots \Delta_{k-1}^{n_{FIR}}\right]^T \mid z_k\right]$. The detected jump on

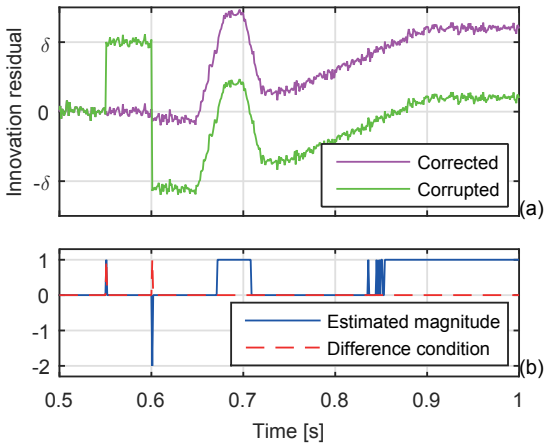

Figure 2.8 – An example of an innovation signal z_k^c corrupted by a positive jump at $t = 0.55$s, a double negative jump at $t = 0.6$s and ramps/drifts between $t = 0.65$s and $t = 0.9$s is given in (a). The corrected innovation residual $\tilde{z}_k^c$ is also plotted. The estimated magnitude $w\left(z_k^c\right)$ and the time difference condition $|z_k^c - z_{k-1}^c| \geq \kappa\delta$ are shown in (b). Observe that in (b), the jumps in the corrupted z_k^c exceed both the magnitude threshold and the ramp threshold. Consecutively, they are flagged as fringe jumps and are corrected for as desired. Note also in (b) that the ramps in z_k^c are correctly not flagged as fringe jumps since they do not exceed the time difference threshold even if they exceed the magnitude threshold.

chord c is denoted by $\mathbb{E}\left[\Delta_{k-1}^c \mid z_k\right]$ and is now chosen as

$$\mathbb{E}\left[\Delta_{k-1}^c \mid z_k\right] \approx \begin{cases} w\left(z_k^c\right) & \text{if } \left|z_k^c - z_{k-1}^c\right| \geq \kappa\delta \\ 0 & \text{if } \left|z_k^c - z_{k-1}^c\right| < \kappa\delta \end{cases} \tag{2.40}$$

where the estimated jump magnitude $w\left(z_k^c\right)$ is chosen as a truncation function and is defined as $w\left(z_k^c\right) = \operatorname{sgn}\left(z_k^c\right)\left\lceil \left|\frac{z_k^c}{\delta}\right| - \gamma \right\rceil$ where $\lceil a \rceil$ is the smallest integer larger then or equal to $a \in \mathbb{R}$. The corrected innovation residual is denoted by $\tilde{z}_k^c$ and is given by

$$\tilde{z}_k^c = z_k^c - \delta\,\mathbb{E}\left[\Delta_{k-1}^c \mid z_k^c\right] \tag{2.41}$$

Effectively, (2.41) is a modification of a wrapping (or modulo) operator applied on z_k^c. In fact, (2.41) reduces to $\tilde{z}_k^c = z_k^c (\text{mod } \delta)$ for $\gamma = 1$ and if $\left|z_k^c - z_{k-1}^c\right| \geq \kappa\delta$. We choose $\gamma = 0.9$ and $\kappa = 0.5$. The satisfactory response of the corrected innovation $\tilde{z}_k^c$ to an example innovation signal z_k^c containing both jumps and ramps is shown in Figure 2.8, including also the signals $w\left(z_k^c\right)$ and $\left|z_k^c - z_{k-1}^c\right| \geq \kappa\delta$. The detected jump (2.40) is subtracted from the innovation residual in (2.41) (also in (3.31)) and stored in the fringe jump state $\hat{d}_k$ in (2.36).

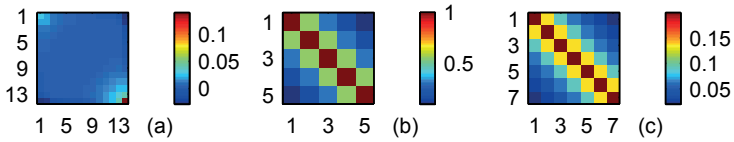

Figure 2.9 – Graphical representation of the matrices R_k (a), Q^T (b) and Q_k^x (c).

2.3.3 Design of the covariance matrices

The estimation accuracy and estimation convergence speed of an EKF is determined by the choice of the covariance matrices Q_k^x, Q_k^ζ and R_k (see e.g. [Anderson and Moore, 1979]).

The measurement covariance matrix R_k is chosen a priori as the sample covariance of high-pass diagnostic data. The covariance is increased on distrusted output channels or channels whose numerical evaluation of the line-integrals are sensitive to errors in the equilibrium reconstruction, as discussed in Section 2.2.7. In this way, the EKF estimates rely less on interferometry chords deemed unreliable.

The choice of the covariance matrices Q_k^x and Q_k^ζ is a design tradeoff between estimation accuracy, estimation convergence speed and noise level of the estimated state. Furthermore, the choice of the spatial structure of Q_k^x and Q_k^ζ determines the smoothness of the estimated profiles and the spatial correlation of the disturbance estimates.

The process covariance matrix Q_k^x is chosen as a symmetric Toeplitz (constant-diagonals) matrix, with a descending first row. Its entries reflect the amount of uncertainty on the state evolution. Increasing the values of Q_k^x increases the Kalman gain L_k (see (2.31) and (2.34)) and thereby improves the estimation accuracy, but also increases the amplification of measurement noise to the state estimate. The values of the first row determine the spatial correlation of the estimated profile and are chosen as exponentially decaying values. Increasing the decay width causes the profile estimates to be more spatially correlated and thus smooth, but decreases the estimation convergence speed.

The disturbance covariance matrix Q_k^ζ is chosen as the product of a diagonal matrix Q_D and a symmetric Toeplitz matrix Q_T with a unit diagonal and a descending first row. The entries of Q_D determine the rate at which the estimated state disturbances $\hat{\zeta}_k$ change. Increasing these increases the convergence speed of estimated model errors/disturbances. The values of the first row of Q_T determine the spatial correlation of the estimated disturbances and are chosen as exponentially decaying values. Increasing this decay width promotes smoothness of the estimated disturbances [Felici et al., 2014a]. An example of the matrices R_k, Q_T and Q_k^x is given in Figure 2.9. In Section 2.3.4, the effects of two different

settings is investigated.

2.3.4 Observer performance with simulated data

In this subsection, the estimation performance of the EKF on simulated data for TCV is assessed. The comparison allows to assess the estimation quality with respect to the simulated density. Results for two different settings of the Kalman gain (2.34) and different numbers of interferometry chords are presented.

Estimation quality and tuning tradeoffs for different observer gains

In order to assess the performance of the observer, two cases in which the observer estimates a *simulated* density profile with two different settings of the observer gain are shown. The system (2.17) is simulated and the observer (2.29)-(2.40) is applied to the simulated diagnostic signals (2.23). Some model coefficients (see Table 2.1) used in the observer are perturbed with respect to those used in the simulation, representing inaccurate knowledge of the transport processes, to assess the ability of the observer to estimate the density in the presence of modeling uncertainties. The simulation uses input and parameter data from TCV shot #41953 to recreate a realistic discharge scenario. White noise with the sample covariance of high-pass measurements of TCV shot #41953 is added to (2.23) as measurement noise.

The simulation results for the cases of high and low Kalman gain are shown in Figure 2.10 and Figure 2.11, respectively. As expected from the discussion in Section 2.3.3, a high Kalman gain yields accurate estimates of the density, as seen in the estimation error (Figure 2.10(c)), density profile (Figure 2.10(f)) and the spatial profile of the measurements (Figure 2.10(g)), but these estimates are affected by the measurement noise (Figure 2.10(c)(d)). On the other hand, a low Kalman gain yields less accurate estimates of the density, as seen in the estimation error (Figure 2.11(c)), density profiles (Figure 2.11(f)) and the spatial profile of the measurements (Figure 2.11(g)), but these estimates contain less measurement noise (Figure 2.11(c)(d)). However, in both cases the estimation error is favourably small and the disturbance estimate $\hat{\zeta}_{k|k}$ compensates for systematic modeling errors formed by the perturbed coefficients.

While either choice for the Kalman gain used in this section has its advantages and drawbacks, optimal settings follow from requirements. We feel that an intermediate setting provides the best estimation accuracy and an acceptable noise level in the estimated density. In this case, we proceed with an intermediate gain with respect to the gains used in this section.

Estimation quality for different numbers of interferometry channels

The number of interferometry channels n_{FIR} is different for each tokamak. Existing density profile reconstruction methods require $m \leq n_{FIR}$ to invert $\Omega(p_k)$

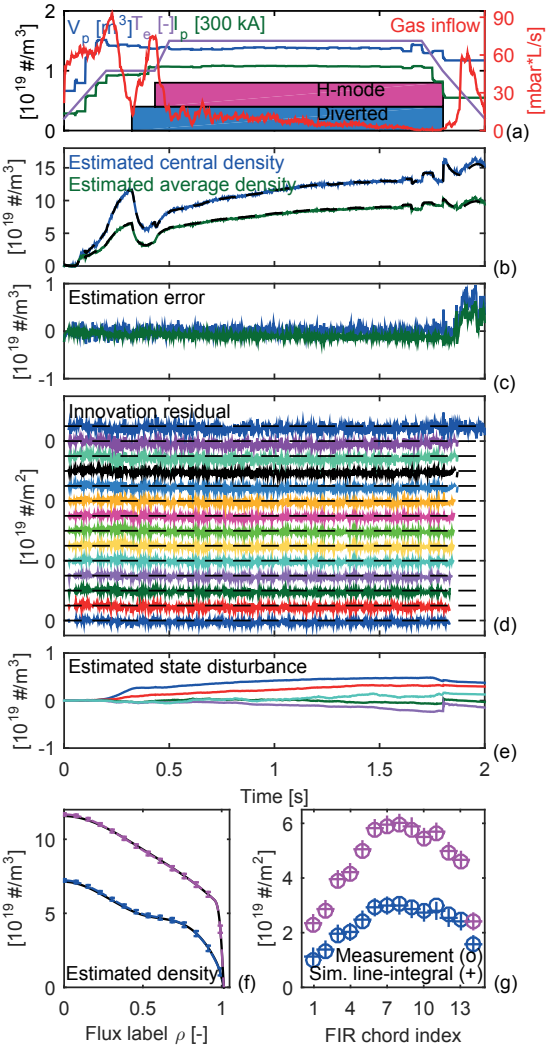

Figure 2.10 – Observer results for simulated data. A high Kalman gain is used. The input and parameter data of TCV shot #41953 are shown in (a). The estimated central and average density are shown in (b), with simulated densities in black. The elements of the corrected innovation residual $z_k - \delta\mathbb{E}\left[\Delta_{k-1} \mid z_k\right]$ (see (3.31)) are shown in (d), individually offset at intervals of $1 \times 10^{19}\,\mathrm{m}^{-2}$. The estimated disturbance is shown in (e). The estimated density profiles with confidence bounds (2.38) at $t = 0.25$s (blue) and $t = 1$s (magenta) are shown in (f), with simulated profiles in black. The measurements and updated measurements (2.39) at these time slices are shown in (g).

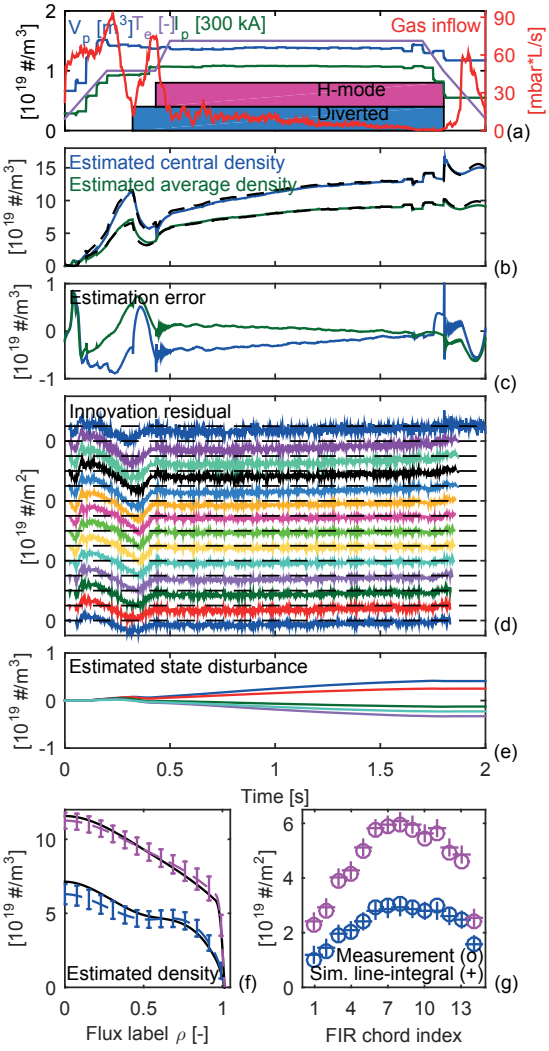

Figure 2.11 – Observer results for simulated data. A low Kalman gain is used. The input and parameter data of TCV shot #41953 are shown in (a). The estimated central and average density are shown in (b), with simulated densities in black. The elements of the innovation residual $z_k - \delta\mathbb{E}\left[\Delta_{k-1} \mid z_k\right]$ (see (3.31)) are shown in (d), individually offset at intervals of $1 \times 10^{19}\,\mathrm{m}^{-2}$. The estimated disturbance is shown in (e). The estimated density profiles with confidence bounds (2.38) at $t = 0.25$ (blue) and $t = 1$ (magenta) are shown in (f), with simulated profiles in black. The measurements and updated measurements (2.39) at these time slices are shown in (g).

Table 2.1 – Model perturbations

Coefficient	Unit	Nominal	Perturbed
D	$[\mathrm{m}^2/\mathrm{s}]$	1	0.8
ν	$[\mathrm{m}/\mathrm{s}]$	10	5
N_{sat}	[#]	3×10^{19}	6×10^{19}
$\langle \sigma v \rangle_{\mathrm{iz}} (T_{\mathrm{e,b}})$	$[\mathrm{m}^3/\mathrm{s}]$	1×10^{-14}	2×10^{-14}

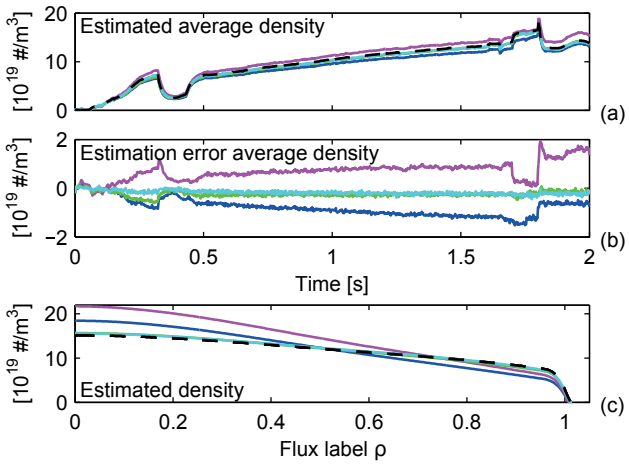

Figure 2.12 – Observer response to different number of interferometry channels. The simulated density is shown as a black dashed line. Reconstructed densities using either central channel #7 (blue), side channel #11 (magenta), three channels #3,#7,#11 (green), all 14 channels (cyan). The density profiles at $t = 1$s are shown in the lower figure. In case of a single channel, the profile shape is deduced from the model. In case of multiple channels, the profile shape is reconstructed from the measurements. The reconstruction quality is best when all channels are used.

in (2.23) and provide the static mapping $y_k \to \hat{x}_k$. The observer (2.29)-(2.40) with $m = 5$ is applied on the system simulation from Section 2.3.4 for different subsets of the 14 interferometry channels of TCV. Again, the observer uses the perturbed coefficients with respect to those used in the simulation, see Table 2.1. In Figure 2.12, the observer performance is shown using either a central channel #7, a side channel #11, three channels #3,#7,#11, and all 14 channels. In case of using a single channel, the profile shape is entirely deduced from the model known to the observer. Consequently, the estimation error (see Figure 2.12(b)) is large and there are large differences between the simulated

and estimated profile. While 14 output channels provide the best accuracy, only three channels already provide a small steady-state estimation error. This result can be attributed to the smoothness of the profile predicted by the model, while the update step keeps the predicted density evolution from drifting away from the measurements.

2.3.5 Observer performance with experimental data

In this section, the estimation performance of the observer on experimental interferometer data of TCV is assessed and compared to Thomson scattering measurements. Quantitative statements on the accuracy of estimated density profiles with respect to Thomson scattering points are challenging, since the error bars provided with the Thomson scattering measurement only account for noise. They do not account for inaccuracies in equilibria, which are used to map the measurement locations to ρ_{tor} loci.

Low density L-mode shot

The performance of the observer on measurement data from TCV shot #47675 is shown in Figure 2.13. This shot contains two consecutive fringe jumps on chord #10. All 14 channels except three central and one outer malfunctioning chords are used to estimate the density. The model coefficients used in the observer are those chosen in Section 2.2.10, which were found to be representative for a typical discharge in TCV. Up to 0.6s, the estimated density profiles lie close to the Thomson scattering measurements, see Figure 2.13(b)(e)). After 0.6s, the density is estimated to increase, although this is not visible in the Thomson scattering measurements, see Figure 2.13(b)(e)). The cause for these may be in inaccurate evaluation of the line integrals (see Section 2.7) due to inaccurate reconstructed equilibria. Note that the measured and estimated interferometer signals match well at the low-field side interferometer chords, but show large discrepancies at the high-field side interferometer chords. In Figure 2.13(f), the low-field side interferometer is #1 and the high-field side interferometer is #14. Accordingly, the innovation residuals are large for the high-field side interferometers, which are the uppermost traces in Figure 2.13(c). A quantitative analysis of the propagation of equilibrium reconstruction errors to the evaluation of the line-integrals is beyond the scope of this paper.

Two consecutive fringe jumps around $t = 0.33$s on chord #10 are correctly flagged and corrected (see Figure 2.13(f)). Note that the malfunction of three central chords (#8, #9 and #10) implies that the central density must be extrapolated by the observer from the other chords using the model.

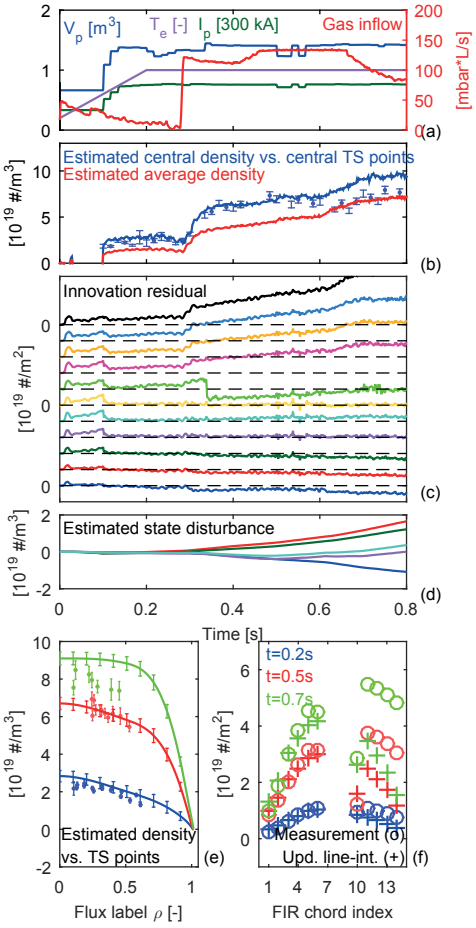

Figure 2.13 – Observer results for experimental data of TCV shot #47675. The input and parameter data of this shot are shown in (a). The estimated central and average density are shown in (b) together with the Thomson scattering measurements at $\rho_{\mathrm{tor}} = 0.1$. The elements of the innovation residual $z_k - \delta\mathbb{E}\left[\Delta_{k-1} \mid z_k\right]$ (see (3.31)) are shown in (c), individually offset at intervals of $1 \times 10^{19}\,\mathrm{m}^{-2}$. The estimated disturbance is shown in (d). The estimated density profiles with confidence bounds (2.38) and Thomson scattering measurements at three time slices are shown in (e). The interferometer measurements and synthetic estimated interferometer signals (2.39) at these time slices are shown in (f). The error bars on the Thomson scattering measurements represent the sample standard deviation of the data in bins with a $\rho_{\mathrm{tor}} = 0.05$ width and covering three consecutive time points.

High density H-mode shot

The performance of the observer on measurement data from TCV shot #48656 is shown in Figure 2.14. All 14 channels are used to estimate the density. Multiple fringe jumps occur on interferometer channel #14, although they are all corrected, see Figure 2.14(c)(f). The estimated density profiles lie close to the Thomson scattering measurements, see Figure 2.14(b)(e)). However, discrepancies can be seen when the estimated profile shapes are compared to the Thomson scattering measurements, see Figure 2.14(e). Yet, the measured interferometer and synthetic estimated interferometer signals at these time slices match to a high degree, see Figure 2.14(f). These discrepancies might be caused by inaccurate equilibrium reconstruction and evaluation of the line-integrals. Note that equilibria are used both to evaluate the line-integrals, as well as to map the Thomson scattering points to ρ_{tor} loci. Errors in reconstructed equilibrium may propagate in different ways to these to applications. Inaccurate reconstruction of the location of the magnetic axis because of inaccuracies in the free source terms in the equilibrium reconstruction problem due to inaccurate pressure measurements can lead to inaccurate evaluation of the central interferometer line-integrals. In Figure 2.15, the density profiles obtained by the observer are compared to profiles obtained by a static static least-squares fit of interferometry data using the measurement matrix $\Omega(p_k)$, see equation 2.24. The least-squares fit uses a minimum amount of Tikhonov regularization to suppress spatial oscillations at the plasma edge. However, the fringe jumps on the edge chord #14 after 0.6s cause the profile fit to display a steep internal gradient. Recall from Figure 2.14 that although the estimated profiles from the observer show shape discrepancies with respect to the Thomson scattering measurements, its measured and updated interferometry signals show remarkable similarity. The differences between the profiles are most likely related to the ill-conditioned least-squares fit which requires regularization, and to the propagation of equilibrium errors to the calculation of line-integrals and the mapping Thomson scattering points.

Still, the inclusion of Thomson scattering measurements into a real-time implementation of the observer using a common real-time reconstructed equilibrium could produce more accurate density profile estimates. When comparing their respective advantages and disadvantages, we can note that Thomson scattering density measurements provide better spatial resolution and do not suffer from fringe jumps when compared to interferometry measurements. However, Thomson scattering measurements are typically available at a lower sample frequency. When employing both diagnostics appropriately in an observer, the combined advantages could compensate for their respective drawbacks.

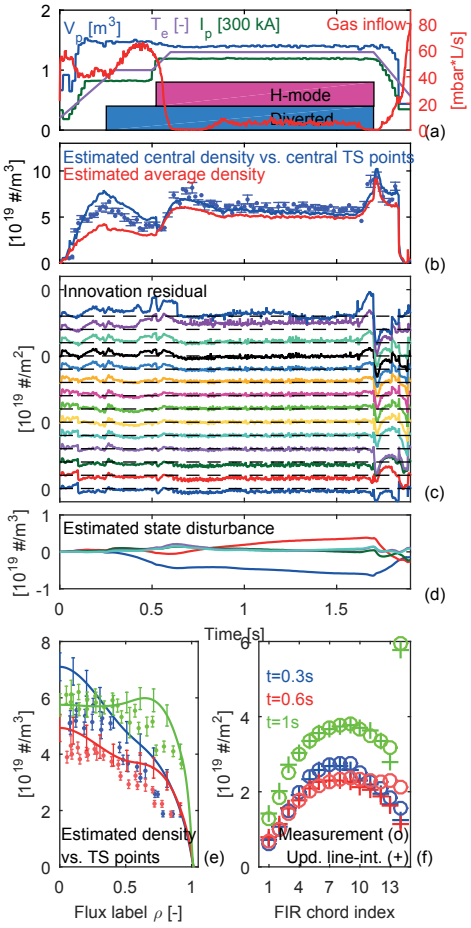

Figure 2.14 – Observer results for experimental data of TCV shot #48656. The input and parameter data of this shot are shown in (a). The estimated central and average density are shown in (b) together with the Thomson scattering measurements at $\rho_{\mathrm{tor}} = 0.1$. The elements of the innovation residual $z_k - \delta\mathbb{E}\left[\Delta_{k-1} \mid z_k\right]$ (see (3.31)) are shown in (c), individually offset at intervals of $1 \times 10^{19}\,\mathrm{m}^{-2}$. The estimated disturbance is shown in (d). The estimated density profiles with confidence bounds (2.38) and Thomson scattering measurements at three time slices are shown in (e). The interferometer measurements and synthetic estimated interferometer signals (2.39) at these time slices are shown in (f). Again, the error bars on Thomson scattering measurements represent the sample standard deviation of the data in bins with a $\rho_{\mathrm{tor}} = 0.05$ width and covering three consecutive time points.

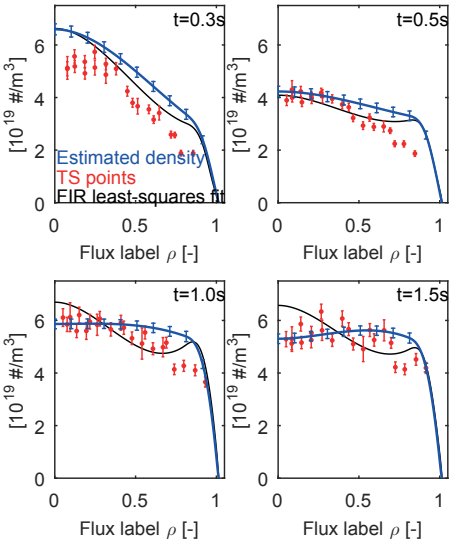

Figure 2.15 – Comparison of density profiles obtained by the observer, by a static least-squares fit of interferometry data and Thomson scattering measurements for TCV shot #48656. Again, the error bars on Thomson scattering measurements represent the sample standard deviation of the data in bins with a $\rho_{\text{tor}} = 0.05$ width and covering three consecutive time points. Note that both the estimated density profiles and the least-squares fit use interferometry data, but no Thomson scattering data.

2.4 Future extensions and research

It is known that the fuelling efficiency of the gas valve decreases with increasing electron temperature in the SOL, since the ionization depth decreases with increasing electron temperature [Belo et al., 2015; Romanelli et al., 2015]. This is problematic for ITER and different actuators must be used instead for density control at high plasma temperature. Pellet injection is foreseen to provide fuelling at high temperature, while the strike point positions could influence the pumping and ECRH influences the peaking of the density profile. In the future we will extend the modeled ionization (2.6) with a temperature-dependent ionization distribution. This will allow the design of controllers which are able to deal with the changing fuelling efficiency of available actuators. Moreover we may model the effect of the strike point locations on pumping, and the pump-out mechanism: the influence of ECRH on the density transport.

Additional diagnostics systems such as Thomson scattering, Bremsstrahlung, reflectometry and polarimetry may be incorporated in the observer for even

more reliable real-time density profile estimation. The detection of fringe jumps may be improved by incorporating the measurement residuals of neighbouring interferometry chords, or including information from other diagnostics such as Thomson scattering.

The observer will be implemented on tokamak control systems in the near future, and tested against more detailed physics codes for ITER.

2.5 Conclusion

A model-based approach to the design of a real-time plasma density profile reconstruction algorithm has been presented.

A control-oriented model was derived from a spatially discretized plasma transport equation which takes main particle transport channels into account. Simulation results show that the model is able to reproduce the evolution of interferometry signals during a TCV and an ASDEX Upgrade discharge with gas fuelling, by tuning the appropriate coefficients.

Based on this model, an extended Kalman filter was designed that estimates the density profile, state disturbances as well as fringe jumps in the interferometry signals. The state disturbance estimates form an effective way to compensate for model-reality mismatches, even with significant mismatch between the model assumed in the algorithm and the model used to simulate the system. Reconstructions on simulated data as well as offline reconstruction simulations on experimental data show that the observer estimates the density profile with an accuracy that is comparable to static fits when compared to Thomson scattering measurements. Yet, the proposed method provides profiles that are physically more realistic, whereas static fits can have spatial oscillations caused by their ill-conditioned inversion problem. It is shown that the estimation accuracy increases with the number of measurement channels used and increases with a well-chosen observer gain. In the light of scarce diagnostics on future reactors, additional and improved selfconsistent modeling of radial transport and particle recycling could further improve the estimation accuracy. The extensions mentioned in Section 2.4 as well as implementation, testing and validation on tokamak control systems are planned for the near future.

2.6 Acknowledgments

The work has been carried out within the framework of the EUROfusion Consortium and has received funding from the EURATOM research and training programme 2014-2018 under grant agreement No 633053. The views and opinions expressed herein do not necessarily reflect those of the European Commission. This work was supported in part by the Netherlands Organization for Scientific

Research via F. Felici's VENI grant: "Control of plasma profiles in a fusion reactor" (no. 680.47.436). The authors gratefully acknowledge Josef Kamleitner of SPC-EPFL for providing the GTI code to compute the interferometry matrix, and Wouter Vijvers of FOM-DIFFER and Alexander Mlynek of IPP Garching for useful discussions.

Appendix

This appendix treats the details of the numerical implementation, including the spatial and temporal discretization of the radial particle density transport equation (2.2) as well as some measures which have been taken to render the problem computationally efficient for real-time applications. Appendix 2.A treats the spatial discretization of the PDE using finite elements and Appendix 2.B shows the time discretization. Finally, Appendix 2.C shows how the line-integrals of the electron density in (2.21) are efficiently numerically evaluated.

2.A Spatial discretization using a finite-element method

The infinite-dimensional problem of the PDE (2.2) in the spatial coordinate ρ is transformed into a finite-dimensional problem using the finite-element method (see, e.g. [Hughes, 1987]) similar to [Felici and Sauter, 2012]. An important advantage of using a finite element method is that it allows efficient computation of the dynamics, required for real-time applications, and also that the order of spatial derivatives of the elements involved are, as we will see, one order lower than the order of the PDE.

The resulting system of ODEs will contain the physical quantities in the parameter $p(t) = \left[\begin{array}{ccccccccc} c_{\mathrm{D}} & c_{\mathrm{H}} & T_{\mathrm{e,b}} & I_{\mathrm{p}} & V' & G_1 & G_0 & \Omega \end{array}\right]$ defined in Section 2.2.5, which lies in the parameter space $\mathcal{P}$, i.e. $p(t) \in \mathcal{P}$. For reasons of brevity, the parameter space is not explicitly specified, but the letter $\mathcal{P}$ is used to indicate functional dependencies of the parameter $p(t)$ in the remainder of this paper.

Consider our time-varying, inhomogeneous PDE (2.2) on the domain $\Omega = \{(t, \rho) \in \mathbb{R} \mid t_0 \leq t \leq t_{\mathrm{f}},\ 0 \leq \rho \leq \rho_{\mathrm{e}}\}$

$$\frac{1}{V'}\frac{\partial}{\partial t}\left(n_e V'\right) + \frac{1}{V'}\frac{\partial \Gamma}{\partial \rho} = S \tag{2.42}$$

with the radial particle flux Γ given by (2.3) and the net electron source S given by (2.4). First, we approximate the electron density by

$$n_e(\rho, t) = \sum_{\alpha=1}^{m} \Lambda_\alpha(\rho)\, b_\alpha(t) \tag{2.43}$$

where the basis functions $\Lambda_\alpha : [0, \rho_e] \to [0, 1]$, $\alpha = 1, ..., m$ are chosen as cubic B-splines with a finite support [de Boor, 2001]. The knot sequence is denoted by $\rho_1 < \rho_2 < \cdots < \rho_{m-1} < \rho_m$ and we fix $\rho_1 = 0$, $\rho_{m-1} = 1$ and $\rho_m = \rho_e$. The boundary conditions $\frac{\partial n_e}{\partial \rho}\Big|_{\rho=0} = 0$ and $n_e|_{\rho=\rho_e} = 0$ of Section 2.2.1 are satisfied by choosing the basis functions Λ_α as the appropriate linear combination of the B-splines [de Boor, 2001] such that $\frac{\partial \Lambda_\alpha}{\partial \rho}\Big|_{\rho=0} = 0$ and $\Lambda_\alpha(\rho_e) = 0$ for every $\alpha = 1, ..., m$. For the purpose of control-oriented modeling, a small number of density states ($m = 5$) with closely-spaced knots near the plasma edge is chosen, see Figure 2.4 for an example of basis functions.

By substituting the electron density parameterization (2.43) in (2.42), (2.3) and (2.4), the electron density continuity is written as

$$\sum_{\alpha=1}^{m} \Lambda_\alpha \frac{\partial}{\partial t}(b_\alpha V') = \sum_{\alpha=1}^{m} b_\alpha \frac{\partial}{\partial \rho}\left(V'\left(G_1 D \frac{\partial \Lambda_\alpha}{\partial \rho} + G_0 \nu \Lambda_\alpha\right)\right) + V' S \tag{2.44}$$

where the net electron source S is written as

$$\begin{aligned} S &= \left(\Lambda_{\mathrm{iz}} \langle \sigma v \rangle_{\mathrm{iz}}(T_{\mathrm{e,b}}) \frac{N_{\mathrm{v}}}{V_{\mathrm{v}}} - \frac{H(\rho - 1)}{\tau_{\mathrm{SOL}}}\right) \sum_{\alpha=1}^{m} b_\alpha \Lambda_\alpha \\ &\quad - \Lambda_{\mathrm{rec}} \langle \sigma v \rangle_{\mathrm{rec}}(T_{\mathrm{e,b}}) \left(\sum_{\alpha=1}^{m} b_\alpha \Lambda_\alpha\right)^2 + \Lambda_{\mathrm{NBI}} \Gamma_{\mathrm{NBI}} + \Lambda_{\mathrm{pellet}} \Gamma_{\mathrm{pellet}} \end{aligned} \tag{2.45}$$

Projecting (2.44) onto a set of test functions $\Psi_\beta : [0, \rho_e] \to [0, 1]$, $\beta = 1, ..., m$ and integrating over the spatial domain yields the weak formulation of (2.42). The test functions $\Psi_\beta(\rho)$, $\beta = 1, ..., m$ with $\sum_{\beta=1}^{m} \Psi_\beta(\rho) = 1$ are chosen as cubic B-splines with a finite support on the same knot sequence $\rho_1 < \cdots < \rho_m$. The weak form can be formulated for every $\beta = 1, 2, ..., m$ and is written as

$$\begin{aligned} \sum_{\alpha=1}^{m} \frac{db_\alpha}{dt} \int_0^{\rho_e} \Psi_\beta \Lambda_\alpha V' d\rho &= -\sum_{\alpha=1}^{m} b_\alpha \int_0^{\rho_e} \frac{\partial V'}{\partial t} \Psi_\beta \Lambda_\alpha d\rho + \int_0^{\rho_e} \Psi_\beta S V' d\rho \\ &\quad + \sum_{\alpha=1}^{m} b_\alpha \int_0^{\rho_e} \Psi_\beta \frac{\partial}{\partial \rho}\left(V'\left(G_1 D \frac{d\Lambda_\alpha}{d\rho} + G_0 \nu \Lambda_\alpha\right)\right) d\rho \\ &= -\sum_{\alpha=1}^{m} b_\alpha \int_0^{\rho_e} \frac{\partial V'}{\partial t} \Psi_\beta \Lambda_\alpha d\rho + \int_0^{\rho_e} \Psi_\beta S V' d\rho \\ &\quad - \sum_{\alpha=1}^{m} b_\alpha \int_0^{\rho_e} \frac{d\Psi_\beta}{d\rho} V'\left(G_1 D \frac{d\Lambda_\alpha}{d\rho} + G_0 \nu \Lambda_\alpha\right) d\rho \\ &\quad + \sum_{\alpha=1}^{m} b_\alpha \Psi_\beta V'\left(G_1 D \frac{d\Lambda_\alpha}{d\rho} + G_0 \nu \Lambda_\alpha\right)\Big|_0^{\rho_e} \end{aligned} \tag{2.46}$$

Note that integration by parts is used which reduces the order of the maximum radial derivative to be evaluated. The weak form is now written[1] as

$$\begin{aligned}\sum_{\alpha=1}^{m}[M]_{\beta\alpha}\frac{db_\alpha}{dt} &= \sum_{\alpha=1}^{m}[H]_{\beta\alpha}\,b_\alpha + N_{\mathrm{v}}\sum_{\alpha=1}^{m}[J]_{\beta\alpha}\,b_\alpha \\ &\quad + \sum_{i=1}^{m}\sum_{\alpha=1}^{m}[L_\beta]_{i\alpha}\,b_\alpha b_i + [P]_\beta\begin{bmatrix}\Gamma_{\mathrm{NBI}}\\ \Gamma_{\mathrm{pellet}}\end{bmatrix}\end{aligned}$$

which can also be written in vector form

$$M\frac{db}{dt} = Hb + N_{\mathrm{v}}Jb + \begin{bmatrix} b^TL_1 \\ \vdots \\ b^TL_m\end{bmatrix}b + P\begin{bmatrix}\Gamma_{\mathrm{NBI}}\\ \Gamma_{\mathrm{pellet}}\end{bmatrix} \tag{2.47}$$

where the elements of the matrices functions $M, H, J, L_\beta : \mathcal{P} \to \mathbb{R}^{m\times m}$, $\beta = 1, ..., m$ and $P : \mathcal{P} \to \mathbb{R}^{m\times 2}$ are defined as

$$[M]_{\beta\alpha} = \int_0^{\rho_{\mathrm{e}}}\Psi_\beta\Lambda_\alpha V'd\rho \tag{2.48}$$

$$\begin{aligned}[H]_{\beta\alpha} &= -\int_0^{\rho_{\mathrm{e}}}\frac{\partial V'}{\partial t}\Psi_\beta\Lambda_\alpha d\rho - \int_0^{\rho_{\mathrm{e}}}\frac{d\Psi_\beta}{d\rho}V'\left(G_1D\frac{d\Lambda_\alpha}{d\rho} + G_0\nu\Lambda_\alpha\right)d\rho \\ &\quad + \Psi_\beta V'\left(G_1D\frac{d\Lambda_\alpha}{d\rho} + G_0\nu\Lambda_\alpha\right)\Big|_0^{\rho_{\mathrm{e}}} - \frac{1}{\tau_{\mathrm{SOL}}}\int_1^{\rho_{\mathrm{e}}}\Psi_\beta\Lambda_\alpha V'd\rho\end{aligned} \tag{2.49}$$

$$[J]_{\beta\alpha} = \frac{\langle\sigma v\rangle_{\mathrm{iz}}(T_{\mathrm{e,b}})}{V_{\mathrm{v}}}\int_0^{\rho_{\mathrm{e}}}\Lambda_{\mathrm{iz}}\Psi_\beta\Lambda_\alpha V'd\rho \tag{2.50}$$

$$[L_\beta]_{i\alpha} = -\langle\sigma v\rangle_{\mathrm{rec}}(T_{\mathrm{e,b}})\int_0^{\rho_{\mathrm{e}}}\Lambda_{\mathrm{rec}}\Psi_\beta\Lambda_\alpha\Lambda_i V'd\rho \tag{2.51}$$

$$[P]_\beta = \int_0^{\rho_{\mathrm{e}}}\Psi_\beta\begin{bmatrix}\Lambda_{\mathrm{NBI}} & \Lambda_{\mathrm{pellet}}\end{bmatrix}V'd\rho \tag{2.52}$$

The term $\Psi_\beta V'\left(G_1D\frac{d\Lambda_\alpha}{d\rho} + G_0\nu\Lambda_\alpha\right)\Big|_0^{\rho_{\mathrm{e}}}$ in (2.49) reduces to $\Psi_\beta V'\left(G_1D\frac{d\Lambda_\alpha}{d\rho} + G_0\nu\Lambda_\alpha\right)\Big|_{\rho_{\mathrm{e}}}$ since $V'|_{\rho=0} = 0$. This resulting term represents particle flux Γ at the domain boundary ρ_{e} in the weak formulation (2.47). Therefore $\Gamma|_{\rho_{\mathrm{e}}}$ has been added as an inflow to the vacuum inventory (2.11). Note the nonlinear terms in (2.47).

Next, the wall and vacuum particle inventory balances (2.9) and (2.11) are

[1] For ease of notation, the i,j-th element of a matrix $A \in \mathbb{R}^{m\times n}$ or a matrix function $A : \mathcal{U} \to \mathbb{R}^{m\times n}$ is denoted as $[A]_{ij}$, where $i \in \{1, ..., m\}$, $j \in \{1, ..., n\}$ and $\mathcal{U}$ is the argument space.

written as

$$\frac{dN_{\mathrm{w}}}{dt} = A_{\mathrm{wb}}b + A_{\mathrm{ww}}N_{\mathrm{w}} + A_{\mathrm{wv}}N_{\mathrm{v}} + A_2 N_{\mathrm{w}} b \tag{2.53}$$

$$\frac{dN_{\mathrm{v}}}{dt} = A_{\mathrm{vb}}b + A_{\mathrm{vw}}N_{\mathrm{w}} + A_{\mathrm{vv}}N_{\mathrm{v}} - A_2 N_{\mathrm{w}} b + A_{\mathrm{iz}}N_{\mathrm{v}}b + b^T A_{\mathrm{rec}} b + \Gamma_{\mathrm{valve}} \tag{2.54}$$

where the elements of the row functions $A_{\mathrm{wb}}, A_2, A_{\mathrm{vb}}, A_{\mathrm{iz}} : \mathcal{P} \to \mathbb{R}^{1\times m}$, the elements of the matrix function $A_{\mathrm{rec}} : \mathcal{P} \to \mathbb{R}^{m\times m}$, the functions $A_{\mathrm{wv}}, A_{\mathrm{vv}} : \mathcal{P} \to \mathbb{R}$ and the constants $A_{\mathrm{ww}}, A_{\mathrm{vw}} \in \mathbb{R}$ are defined as

$$[A_{\mathrm{wb}}]_\alpha = \frac{1}{\tau_{\mathrm{SOL}}} \int_1^{\rho_{\mathrm{e}}} \Lambda_\alpha V' d\rho \tag{2.55}$$

$$A_{\mathrm{ww}} = -\tau_{\mathrm{release}}^{-1} \qquad A_{\mathrm{vw}} = -A_{\mathrm{ww}}$$

$$A_{\mathrm{wv}} = \frac{c_{wv} V_{\mathrm{v},0}}{V_{\mathrm{v}} \tau_{\mathrm{release}}} \qquad A_{\mathrm{vv}} = -A_{\mathrm{wv}} - \frac{V_{\mathrm{v},0}}{V_{\mathrm{v}} \tau_{\mathrm{pump}}}$$

$$A_2 = -N_{\mathrm{sat}}^{-1} A_{\mathrm{wb}}$$

$$[A_{\mathrm{vb}}]_\alpha = -V' \left(G_1 D \frac{d\Lambda_\alpha}{d\rho} + G_0 \nu \Lambda_\alpha \right) \Big|_{\rho_{\mathrm{e}}}$$

$$[A_{\mathrm{iz}}]_\alpha = -\frac{\langle \sigma v \rangle_{\mathrm{iz}} (T_{\mathrm{e,b}})}{V_{\mathrm{v}}} \int_0^{\rho_{\mathrm{e}}} \Lambda_{\mathrm{iz}} \Lambda_\alpha V' d\rho \tag{2.56}$$

$$[A_{\mathrm{rec}}]_{i\alpha} = n_e \langle \sigma v \rangle_{\mathrm{rec}} (T_{\mathrm{e,b}}) \int_0^{\rho_{\mathrm{e}}} \Lambda_{\mathrm{rec}} \Lambda_i \Lambda_\alpha V' d\rho \tag{2.57}$$

Finally, (2.47) is premultiplied by M^{-1} and stacked with (2.53)-(2.54) to get the nonlinear system of ODEs

$$\frac{dx}{dt} = A(p(t))\, x(t) + f(p(t), x(t)) + B u(t) \tag{2.58}$$

where state vector $x(t) \in \mathbb{R}^{n_x}$ with $n_x = m+2$ and the input vector $u(t) \in \mathbb{R}^{n_u}$ with $n_u = 3$ are defined as

$$x(t) = \begin{bmatrix} b(t) \\ N_{\mathrm{w}}(t) \\ N_{\mathrm{v}}(t) \end{bmatrix} \qquad u(t) = \begin{bmatrix} \Gamma_{\mathrm{valve}}(t) \\ \Gamma_{\mathrm{NBI}}(t) \\ \Gamma_{\mathrm{pellet}}(t) \end{bmatrix}$$

The matrix function $A : \mathcal{P} \to \mathbb{R}^{n_x \times n_x}$, the vector function $f : \mathcal{P} \times \mathbb{R}^{n_x} \to \mathbb{R}^{n_x}$ and the matrix $B \in \mathbb{R}^{n_x \times n_u}$ are defined as

$$A(p) = \begin{bmatrix} M^{-1}H & 0 & 0 \\ A_{\mathrm{wb}} & A_{\mathrm{ww}} & A_{\mathrm{wv}} \\ A_{\mathrm{vb}} & A_{\mathrm{vw}} & A_{\mathrm{vv}} \end{bmatrix} \tag{2.59}$$

$$f(p,x) = \begin{bmatrix} M^{-1}JN_{\mathrm{v}}b + M^{-1}\begin{bmatrix} b^T L_1 \\ \vdots \\ b^T L_m \end{bmatrix} b \\ A_2 N_{\mathrm{w}} b \\ -A_2 N_{\mathrm{w}} b + A_{\mathrm{iz}} N_{\mathrm{v}} b + b^T A_{\mathrm{rec}} b \end{bmatrix} \tag{2.60}$$

$$B = \begin{bmatrix} 0 & M^{-1}P \\ 0 & 0 \\ 1 & 0 \end{bmatrix} \tag{2.61}$$

To quickly compute (2.59)-(2.61), the integrals in (2.48)-(2.52) and (2.55)-(2.57) can be precomputed if the integrands do not depend on time, i.e. if all time- and space-dependent variables are written as (a sum of) products of time-varying variables and functions of ρ. This was naturally done for the electron density in (2.43) but is also done for ν, V' and the mode-dependent D, ν_0, N_{sat}, τ_{SOL}, Λ_{iz}. The time-varying part of V' is separated as e.g. $V' = \frac{\partial V}{\partial \rho} \approx 2\rho V_{\mathrm{p}}(t)$. For example, (2.48) is written as a product $M = 2V_{\mathrm{p}}(t)\, Z_{\mathrm{M}}$ where the matrix $Z_{\mathrm{M}} \in \mathbb{R}^{m\times m}$ does not depend on time and is given by

$$[Z_{\mathrm{M}}]_{\beta\alpha} = \int_0^{\rho_{\mathrm{e}}} \rho \Psi_\beta \Lambda_\alpha d\rho$$

Next, this integral and (2.49)-(2.52) and (2.55)-(2.57) are numerically evaluated using Legendre-Gauss quadrature [Quarteroni et al., 2007] as is also done in [Felici, 2011], for each combination of the switching parameters $c_{\mathrm{D}} \times c_{\mathrm{H}} \in \{0,1\} \times \{0,1\}$.

2.B Time discretization using a trapezoidal method

The system of continuous-time ODEs (2.58) can be discretized in time. Consider an equidistant time grid $t_k = t_0 + kT_{\mathrm{s}},\ k \in \{0,1,...,N\}$ where $T_{\mathrm{s}} > 0$ is the time step and $N = (t_{\mathrm{f}} - t_0)/T_{\mathrm{s}} \in \mathbb{N}$. We choose a finite difference approximation of the time derivative $\frac{dx}{dt}\big|_{t_k} \approx (x_{k+1} - x_k)/T_{\mathrm{s}}$ and apply the trapezoidal method on (2.58) to get

$$\begin{aligned} \frac{x_{k+1} - x_k}{T_{\mathrm{s}}} &= (1-\theta)\left(A(p_k)\, x_k + f(p_k, x_k) + Bu_k\right) \\ &\quad +\theta\left(A(p_{k+1})\, x_{k+1} + f(p_{k+1}, x_{k+1}) + Bu_{k+1}\right) \end{aligned} \tag{2.62}$$

where the discrete-time state, input and parameter are defined as $x_k = x(t_k)$, $u_k = u(t_k)$ and $p_k = p(t_k)$ respectively, and $\theta \in [0,1]$ is a discretization parameter[2]. We choose $\theta = \frac{1}{2}$. For practical reasons, the approximations $p_{k+1} \approx p_k$

[2]This is a generalization of the trapezoidal rule; $\theta = \frac{1}{2}$ yields the trapezoidal rule, whereas $\theta = 0$ and $\theta = 1$ yield the forward and backward Euler method respectively.

and $u_{k+1} \approx u_k$ are applied. To obtain a scheme that requires no iterations, we set $f(p_{k+1}, x_{k+1}) \approx f(p_k, x_k)$. To ensure stability of the scheme given the latter choice, the time step must be sufficiently small. Since most dynamics in the right-hand side of equation 2.58 are linear in the state x, the scheme is found to be stable in practical use with the time step of 1ms used for TCV simulations and 1.5ms for ASDEX Upgrade simulations, presented in Sections 2.2.10, 2.3.4 and 2.3.5.

Rewriting (2.62) and applying these approximations yields the nonlinear system of difference equations

$$x_k = f_\mathrm{d}(p_{k-1}, x_{k-1}) + B_\mathrm{d}(p_{k-1})\, u_{k-1} \tag{2.63}$$

where $f_\mathrm{d} : \mathcal{P} \times \mathbb{R}^{n_x} \to \mathbb{R}^{n_x}$ and $B_\mathrm{d} : \mathcal{P} \to \mathbb{R}^{n_x \times n_u}$ are defined as

$$\begin{aligned} f_\mathrm{d}(p_k, x_k) &= (I - \theta T_\mathrm{s} A(p_k))^{-1} \left[(1-\theta)\, T_\mathrm{s} A(p_k)\, x_k + T_\mathrm{s} f(p_k, x_k)\right] \\ B_\mathrm{d}(p_k) &= (I - \theta T_\mathrm{s} A(p_k))^{-1} T_\mathrm{s} B \end{aligned}$$

2.C Numerical evaluation of line integrals

The spatial discretization (2.43) and an equilibrium $\psi(R, Z)$ allow to write the line integrals in the measurement equation (2.23) as a linear combination of the state x_k. The output equation (2.23) is given by

$$y_k = C(p_k)\, x_k + \delta d_k$$

where $C(p_k) = \left[\begin{array}{cc} \Omega(p_k) & 0^{n_{FIR} \times 2} \end{array}\right]$ and the matrix function $\Omega : \mathcal{P} \to \mathbb{R}^{n_{FIR} \times m}$ is defined as

$$[\Omega]_{i\alpha} = \int_{L_i} \Lambda_\alpha(\rho(r, Z))\, dL \tag{2.64}$$

First, the spatial distribution of ψ is assumed to be available from real-time 2D equilibrium reconstruction on a rectangular R-Z grid of the plasma cross-section (see e.g. [Ferron et al., 1998; Moret et al., 2015]). It is assumed that $\rho(\psi)$ is known.

Next, the integrals are divided in intervals of subsequent points $X_p^{(i)} = [R_p^{(i)}\ Z_p^{(i)}]^T$, $p = 1, ..., n_\mathrm{p}$ which are defined as the intersections between the i-th chord and the rectangular grid lines.

$$[\Omega]_{i\alpha} = \sum_{p=1}^{n_\mathrm{p}-1} \int_{X_p^{(i)}}^{X_{p+1}^{(i)}} \Lambda_\alpha(\rho(X))\, dL$$

Finally, the integrals in (2.64) are numerically evaluated using the trapezoidal method as

$$[\Omega]_{i\alpha} \approx \sum_{p=1}^{n_\mathrm{p}-1} \frac{\Lambda_\alpha\left(\rho\left(X_{p+1}^{(i)}\right)\right) + \Lambda_\alpha\left(\rho\left(X_p^{(i)}\right)\right)}{2} L_p^{(i)}$$

where $\Lambda_\alpha\left(\rho\left(X_p^{(i)}\right)\right)$ is approximated by a linear interpolation between the function values $\Lambda_\alpha\left(\rho\left(X\right)\right)$ evaluated at the two *R-Z* grid points adjacent to the chord-grid intersection point $X_p^{(i)}$, and $L_p^{(i)} = \sqrt{\left(X_{p+1}^{(i)}\right)^2 + \left(X_p^{(i)}\right)^2}$, $p = 1, ..., n_\mathrm{p} - 1$ is the distance between subsequent chord-grid intersection points.

Chapter 3

Model-based real-time plasma electron density profile estimation and control on ASDEX Upgrade and TCV

Abstract Real-time plasma electron density profile estimation and control are essential in the operation of future tokamaks. In particular, the robustness against diagnostics failure and disturbances is important for long pulse operation.

A model-based approach to profile estimation is implemented on the control systems of ASDEX Upgrade and TCV, which is able to merge information from various diagnostics for both core and edge density, as well as systematically handling diagnostic failure. The model used for profile estimation is employed to tune a feedback controller before an experiment, thereby reducing the experimental time required for tuning.

Subsequently, this observer and controller have been employed in scientific experiments on ASDEX Upgrade and TCV. On ASDEX Upgrade, the density profile estimator was used in high-density pellet-fuelled discharges, providing a more reliable real-time estimate of the core density for feedback control than previously achieved. On TCV, in experiments on integrated pressure and safety factor profile control, the density profile estimator and feedback controller provide a constant density despite disturbances from time-varying ECCD power. Additionally, the real-time density profiles provide an essential input for other

This chapter is submitted to Fusion Engineering and Design. The authors of the manuscript are T.C. Blanken, F. Felici, C. Galperti, O. Kudláček, F. Janky, A. Mlynek, L. Giannone, P.T. Lang, W. Treutterer, W.P.M.H. Heemels, M.R. de Baar, the TCV team, the ASDEX Upgrade team and the EUROfusion MST1 team.

real-time plasma state estimation codes including Electron Cyclotron ray tracing codes, contributing to a complete real-time estimation of the entire plasma state.

3.1 Introduction

In future tokamak reactors such as ITER and DEMO, the plasma particle density must be controlled since it directly affects the fusion power, radiation and the non-inductive current distribution [Pironti and Walker, 2005; Wesson, 2004]. Moreover, the density restricts Electron Cyclotron (EC) heating systems (through e.g. EC cutoff) and neutral beam operation (through e.g. beam shinethrough). Additionally, future reactors will necessarily operate close to operational limits (formed by e.g. the Greenwald density limit and tearing modes) which can lead to disruptions. Therefore, these operational limits must be actively avoided, and the requirements for the control of the density on reactors will be increasingly stringent than those on present-day devices [Biel et al., 2015; Gribov et al., 2007].

In particular, the plasma density must be controlled in feedback, since shot-to-shot differences and disturbances (e.g. confinement deterioration from (unexpected) MHD activity or varying wall conditions) could otherwise result in deviations from the target density. Feedback control requires an accurate estimate of the controlled density. However, the diagnostics can have failures (e.g. , fringe jumps on interferometers) and have a finite reliability; in particular in a nuclear environment [Biel et al., 2015]. Therefore, the real-time density estimate must be resilient to common failure modes of diagnostics which could otherwise lead to loss of control and early termination of a discharge.

In recent years, successful research has been done to address the various challenges. Research on real-time density estimation has focused on static fitting methods [Fischer et al., 2010; Mlynek et al., 2011]. However, these methods are susceptible to diagnostic faults. Integrated diagnostic analysis methods for full profile estimation using Bayesian inference employing multiple diagnostics (e.g. , interferometry, Thomson scattering, ECE and/or impact excitation spectroscopy) are powerful [Fischer et al., 2010; Galante et al., 2015; Rathgeber et al., 2010; Reusch et al., 2018], but have not been done in real time for control applications. Detection of faults on density diagnostics has focussed on fringe jump detection from interferometers [Gil et al., 2010; Mlynek et al., 2011].

In work on density feedback control, the controlled density signal is often derived from a single diagnostic system or channel, and it is assumed that this measurement is reliable, see e.g. [Janky et al., 2015; Vijvers et al., 2012]. In [Lang et al., 2012], a hardwired switch from the estimate based on DCN laser interferometers [Mlynek et al., 2011] to an estimate based on CO_2/HeNe laser interferometer was used for density control where pellet injection proved problematic for the DCN system. This paper will provide a generalization of these approaches,

to allow an arbitrary number of diagnostics to be used and allow handling of a wide range of fault scenarios. In our previous work [Blanken et al., 2018b] (this thesis, Chapter 2), a model-based estimator was introduced for profile estimation, which included fringe jump correction. In this approach, a Kalman filter is used to merge interferometry measurements with a model for the density profile evolution. Thereby, it provides redundancy against diagnostic failure, and promotes smoothness of profile estimates to the extent that is in accordance with the physics-based model. The Kalman filter is a recursive Bayesian filter for linear systems [Anderson and Moore, 1979]. It is also used in the RAPTOR-observer for estimation of the temperature and q profile [Felici et al., 2014a, 2016]. Also, the method allows for fringe jump correction based on mismatches between diagnostic signals and model predictions. This real-time capable model was derived from radial transport and heuristic particle flow (e.g. recycling and molecular processes) modeling, since both full first-principle modeling and modeling based on identification from data is considered too challenging, see [Blanken et al., 2018b]. However, this model-based estimator was not yet employed in experiments. This paper provides the first results of actual application of this method in both TCV and ASDEX Upgrade.

In the existing practice of plasma density feedback control, the controller gains are often manually tuned using trial and error on multiple discharges. This is not practical for ITER and DEMO, where experimental time is costly and limited. Instead, a tuning procedure based on a model of the dynamic response of the density to actuation commands should be used. This allows to tune the controller gains before a discharge, so that the experimental time required for tuning can be reduced significantly.

This paper reports on the implementation of the observer on the real-time control systems of ASDEX Upgrade and TCV for experimental use. Moreover, the model [Blanken et al., 2018b] is employed to derive a feedback controller for TCV using robust H_∞ synthesis.

The density profile observer has been employed on ASDEX Upgrade in high-density pellet-fuelled discharges [Lang et al., 2018], which raise the central plasma density above the Greenwald limit. In order to provide diagnostic redundancy, the model-based density profile estimator [Blanken et al., 2018b] is extended with a forward model for the CO_2 interferometer and the Bremsstrahlung measurement. While [Lang et al., 2018] presented the scenario development and results, this paper provides more details on the estimator and its diagnostics integration and fault handling.

On TCV, the profile observer is combined with the density feedback controller for use in experiments on profile control [Maljaars et al., 2017]. In these experiments, the controller ensures a constant density in time despite disturbances from feedback-controlled pressure and safety factor profile using ECCD. The profile observer is included in the architecture for integrated plasma control on TCV [Blanken et al., 2018a; Vu et al., 2018] (this thesis, Chapter 4) to

provide the Greenwald density fraction.

The remainder of this paper is structured as follows. In Section 3.2, a summary of the control-oriented model, the forward diagnostics models and the density profile observer is given. In Section 3.3, the control problem in the high-density pellet-fuelled discharges, implementation of the observer on the ASDEX Upgrade control system and the density estimation and control are presented. In Section 3.4, the control problem in profile control experiments, the feedback controller design, the implementation of the observer and the controller on the TCV control system, and the results of density control are presented. In Section 3.5, the methods and experimental results are discussed. Finally, in Section 3.6, conclusions are presented.

3.2 Model-based density profile observer

A model-based observer for the density profile was introduced in [Blanken et al., 2018b]. It consists of an Extended Kalman filter (EKF) [Anderson and Moore, 1979] which incorporates the RAPDENS model. Moreover, a number of fault handling strategies are employed. A summary of the observer is given in this section.

3.2.1 RAPDENS: a control-oriented 0D+1D model of the electron density evolution

The RAPDENS model [Blanken et al., 2018b] is a control-oriented predictive model for the evolution of the electron density profile $n_e(\rho, t)$, vacuum neutral particle inventory and wall inventory. It is a physics-based dynamic self-consistent model, which includes the effects of:

- particle conservation law for radial (1D) plasma electron evolution,
- 0D models for wall and vacuum neutral particle inventories,
- semi-empirical radial diffusion-drift model,
- semi-empirical source models for inter-inventory channels, e.g. recycling and ionization,
- switched model coefficients for limited versus diverted plasmas. Similar for Ohmic or L-mode versus H-mode plasmas,
- parametrized equilibrium-related quantities given as external (time-varying) input,
- low execution time due to specific choices of temporal and spatial discretization. For example, the execution time is about 10% of the simulation time on the TCV digital control system hardware.

In this model, the electron density profile inside the confined region of the plasma is parametrized as

$$n_e(\rho, t) = \sum_{i=1}^{m} \Lambda_i(\rho)\, x_i(t) \tag{3.1}$$

where ρ is the normalized toroidal flux, $\Lambda_i(\rho)$ are cubic spline basis functions (see [Blanken et al., 2018b]) and $x_i(t)$ is the vector containing the state variables parametrizing the density. A summary of the model equations is given in Appendix 3.A. The full details and derivations are provided in [Blanken et al., 2018b]. For the applications reported in this paper, the dynamics are discretized in space and time similar to equation (3.19) as

$$f\left(x\left(t_k\right), x\left(t_{k-1}\right), p\left(t_{k-1}\right), u\left(t_{k-1}\right)\right) = 0 \tag{3.2}$$

where $x(t_k)$ is the system state at time t_k, $p(t_k)$ contains external physics quantities that influence the density evolution such as plasma current, volume and temperature, and $u(t_k)$ is the actuation input such as gas valve flux, pellet particle flux and neutral beam injection.

3.2.2 Forward synthetic diagnostic models

For the application of a state observer, synthetic models for the relations between the system state x and the measured quantities are needed. These forward synthetic diagnostic models are written in a generic form as

$$y = h(x, \zeta) \tag{3.3}$$

where y is the vector of measured quantities and ζ is a vector containing physical quantities other than the plasma density which may affect the diagnostic measurement. Device-specific functions $h(x, \zeta)$ for the ASDEX Upgrade and TCV diagnostic systems are derived in Section 3.3.2 and Section 3.4.3.

3.2.3 Profile observer design

The operation of the observer is explained next, while the relevant equations are provided in full detail in Appendix 3.B. A dynamic state observer for the density profile [Blanken et al., 2018b] incorporates an Extended Kalman filter [Anderson and Moore, 1979] based on the RAPDENS model (Section 3.2.1) and forward diagnostics models. The Kalman filter is a minimum-variance iterative estimator for linear dynamical systems [Anderson and Moore, 1979]. Since the dynamics in (3.2) are nonlinear, local linearizations are substituted in the Kalman filter equations, resulting in the Extended Kalman filter.

At every time step t_k at which the measurement y_k becomes available,

1. a one time step ahead prediction of the state, denoted[1] as $\hat{x}_{k|k-1}$, is computed based on the previous estimate $\hat{x}_{k-1|k-1}$ using the model (3.2),
2. a prediction of the measurement, denoted as $\hat{y}_{k|k-1} = h\left(\hat{x}_{k|k-1}, \hat{\zeta}_{k-1|k-1}\right)$, is computed based on the predicted state $\hat{x}_{k|k-1}$ and $\hat{\zeta}_{k-1|k-1}$ using the forward diagnostic model (3.3),
3. the difference between the measurement y_k and the predicted measurement $\hat{y}_{k|k-1}$, called the residual z_k, is computed,
4. the residual is corrected for any detected faults in the diagnostic measurements (discussed in the next subsection),
5. the posterior state estimate $\hat{x}_{k|k}$ and $\hat{\zeta}_{k|k}$ is computed by summing the predicted state $\hat{x}_{k|k-1}$ and $\hat{\zeta}_{k-1|k-1}$ with the corrected residual multiplied by the Kalman gain matrix (see (3.31) and Appendix 3.B),
6. various output signals of the observer are computed, e.g. the estimated density profile by substituting $\hat{x}_{k|k}$ in (3.1).

These steps are repeated at each time step. By proper tuning of the observer gain matrix, the state estimate $\hat{x}_{k|k}$ converges to the actual (not directly measured) state x_k of the system. In Figure 3.1, a block diagram of the observer is shown. This diagram illustrates the steps above, as well as its input and output signals, while the underlying equations are provided in Appendix 3.B.

3.2.4 Fault handling

Since information of the observer is used by the density controller and other real-time algorithms, errors in the observer results due to diagnostic faults may propagate downstream to the controller and other real-time algorithms. This can have negative consequences for the discharge. Therefore, the density profile estimates should not become invalid following diagnostics faults and faults on other input signals. Typical examples of diagnostic faults are fringe jumps on interferometers due to fast density transients and signal degradation due to hardware malfunction. Moreover, other real-time algorithms can experience numerical issues and might provide invalid inputs for the observer.

In the observer implementations on ASDEX Upgrade and TCV, two types of fault handling are considered:

1. diagnostics fault handling by real-time detection and correction of known fault modes, and
2. fault handling of the parameter values $p\,(t_k)$ by only passing values that are within specified credibility limits.

First, information about diagnostic fault detection in the ASDEX Upgrade digital control system (DCS) is communicated via dedicated validity flags for each

[1] The variable $\hat{x}_{i|j}$ denotes the estimate of quantity x at time i, given measurements available up to time j.

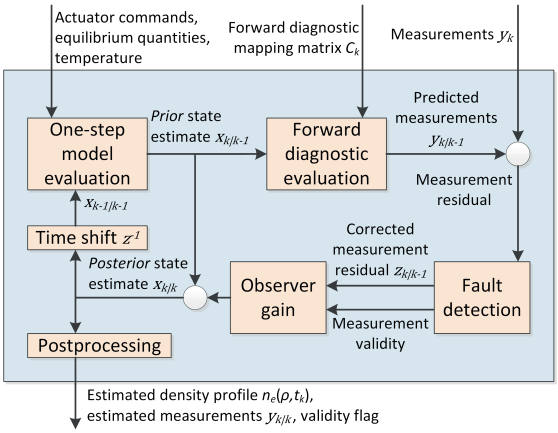

Figure 3.1 – Block diagram of the RAPDENS profile observer. This diagram illustrates the recursive Extended Kalman filter equations provided in Appendix 3.B as well as the fault detection from Section 3.2.4. The observer receives measurements, fuelling commands, as well as the forward diagnostic mapping matrix, plasma current, volume and temperature. At every iteration of the observer, a one-sample ahead prediction is made based on the nonlinear model (3.2) and a forward diagnostics model (3.3) given the state estimate at the previous time step. The state estimate is updated with information from the measurement sample y_k.

real-time signal (see [Treutterer et al., 2014a]). If a diagnostic signal has a validity flag that is not 'good' or the signal is not being produced, the corresponding entries are ignored in the observer equations. Moreover, both implementations have detection and correction schemes for fringe jumps on interferometers. This is shown in more detail in Section 3.3.2, 3.4.3 and Appendix 3.B.

Second, faults on input signals are detected by comparing the signal value to pre-configured validity limits. If a signal value is considered invalid, the previous valid value is held or a user-defined backup value is substituted. For example, if the signal of the real-time reconstructed plasma volume is below or above credible limits (e.g. due to invalid information from the real-time equilibrium reconstruction), the previous credible value is held. Examples of the handling of fault events in experiments are shown in Section 3.3.3 and 3.3.3.

3.3 Profile estimation in high-density experiments on ASDEX Upgrade

In this section, the implementation of the observer on ASDEX Upgrade and its estimation performance in experiments are presented.

3.3.1 Plasma scenario and control problem

In high-density scenarios on ASDEX Upgrade, a core density above the Greenwald limit is reached through pellet injection [Lang et al., 2018]. The scenario is a diverted H-mode at a central density of about $1.6 \times 10^{20} \frac{\#}{m^3}$ corresponding to a Greenwald fraction of $f_{\mathrm{GW}} = 1.25$.

The central electron density is required to follow a step reference signal during the current flat-top phase. Reference tracking is achieved by a feedback controller that commands the pellet launcher as the actuator, see [Lang et al., 2018]. The controlled quantity is provided in real time by the density observer, which can be either the core density, volume- or profile-averaged density. This observer should:

- minimize the profile estimation error, in particular the estimation error of the central density,
- detect and correct for measurement faults,
- be robust against model mismatches.

Moreover, the observer implementation should stay within the available computational time per cycle time of the real-time computer. The cycle time of the DCS is either 1ms or 1.5ms.

3.3.2 Implementation on the ASDEX Upgrade control system

The observer from Section 3.2 is programmed in MATLAB Simulink [The Mathworks Inc., a], then automatically converted into C code for implementation in the DCS [Treutterer et al., 2014a]. A block scheme of the implementation of the density profile observer on the DCS is shown in Figure 3.2. The observer receives:

- interferometer and Bremsstrahlung measurements (discussed next),
- a forward interferometer model C_{FIR} (discussed next) from the real-time equilibrium reconstruction JANET [Giannone et al., 2015],
- equilibrium information (plasma current I_{p}, plasma volume V_{p}, normalized poloidal flux $\rho_{\mathrm{pol}}(\rho_{\mathrm{tor}})$ and x-point presence indicator c_{LD}) from JANET [Giannone et al., 2015],
- the estimated plasma electron temperature T_{e} from the RAPTOR observer [Felici et al., 2011, 2014a].

The quantities in the latter two points are contained in the parameter p, see Section 3.2.1. In the experiments reported in this paper, the algorithm is run at a cycle time of 1.5ms.

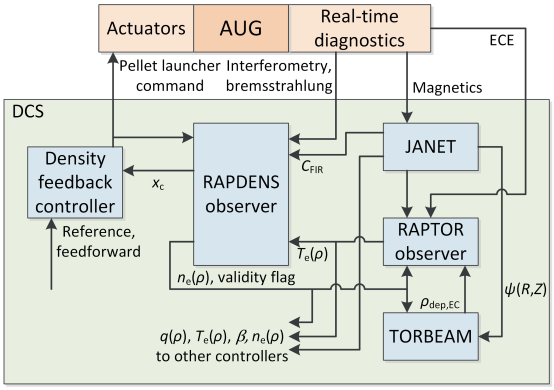

Figure 3.2 – Block diagram of the interconnection of the density profile observer on the ASDEX Upgrade digital control system (DCS) [Treutterer et al., 2014a]. The observer (see Figure 3.1) receives interferometry and bremsstrahlung measurements, a temperature profile from the RAPTOR-observer as well as the interferometry matrix C_{FIR}, plasma current and volume from the equilibrium solver. In the experiment discussed in Section 3.3.3, the estimated on-axis density is the controlled variable x_c which is provided to the feedback controller by the observer.

Forward diagnostics modeling

The diagnostics available in real time on ASDEX Upgrade are the six interferometer chords and two Bremsstrahlung measurement channels. Forward diagnostic models are constructed, which relate the state of the system to the measured quantities as expressed in Section 3.2.2.

The interferometers measure a line-integrated density. This measurement may be corrupted by fringe jumps, and can be written as $y_{\mathrm{DCN}} = \int_{L_{\mathrm{DCN}}} n_e dL + \delta d$, where δ is a constant equal to the line-integrated density corresponding to one fringe and d is an integer representing the cumulative number of fringe jumps at any point in time.

On the DCS, a similar calculation is done by a postprocessing routine of the real-time equilibrium reconstruction code [Giannone et al., 2015], but for the monomial basis functions defined on ρ_{pol} used in [Mlynek et al., 2011]. Using time-varying equilibria, this result is mapped to the basis functions on ρ_{tor} considered in this work (i.e. (3.1)). This results in a linear algebraic relation between the state x and the measurement y_{DCN}.

Since the line-integrals for the V1 interferometer line-of-sight are currently not evaluated in real-time, a different approach is taken to construct this forward model. The measured signal of V1 is assumed to be proportional to the volume-averaged density and modeled as $y_{\mathrm{DCR_V1}} = \zeta_{\mathrm{V1}} \frac{1}{V_{\mathrm{p}}} \int_{V_{\mathrm{p}}} n_e dV$ where ζ_{V1}

is a slowly-changing coefficient that is to be estimated by the observer. Also, the electronics of V1 is naturally resilient to fringe jumps because of its long wavelength [Mlynek et al., 2012].

The Bremsstrahlung depends on effective charge, electron temperature and density as $S_\mathrm{B} \propto Z_\mathrm{eff} T_e^{1/2} n_e^2$ [Wesson, 2004]. On ASDEX Upgrade, the Bremsstrahlung is measured along two lines of sight tangential to the toroidal direction. A real-time evaluation of the density basis functions over the tangential line of sight was not available, therefore a different approach was taken. Instead, it is assumed that the density dependence is a volume-averaged density dependence. Moreover, it is assumed that the effective charge and temperature change slowly with respect to the density. Accordingly, the Bremsstrahlung measurement equation is written as $y_\mathrm{Br} = \zeta_\mathrm{Br} \left(\frac{1}{V_\mathrm{p}} \int_{V_\mathrm{p}} n_e dV \right)^2$ where ζ_Br is a slowly varying coefficient that is to be estimated by the observer. Substituting the density parametrization (3.1) yields the algebraic relation between the state x and the measurement y_Br.

The above forward diagnostics models are stacked as

$$y = \begin{bmatrix} y_\mathrm{DCN_H1} \\ \vdots \\ y_\mathrm{DCN_H5} \\ y_\mathrm{DCR_V1} \\ y_\mathrm{Br1} \\ y_\mathrm{Br2} \end{bmatrix} = \begin{bmatrix} C_\mathrm{FIR} x + \delta d \\ \zeta_\mathrm{V1} C_\mathrm{p} x \\ \zeta_\mathrm{Br1} x^\mathrm{T} C_\mathrm{p}^\mathrm{T} C_\mathrm{p} x \\ \zeta_\mathrm{Br2} x^\mathrm{T} C_\mathrm{p}^\mathrm{T} C_\mathrm{p} x \end{bmatrix} \tag{3.4}$$

where $C_\mathrm{FIR}^{(i,j)} = \int_{L_{\mathrm{DCN_H}i}} \Lambda_j dL$ and $C_\mathrm{p}^{(i)} = \frac{1}{V_\mathrm{p}} \int_{V_\mathrm{p}} \Lambda_i dV$.

Fault handling

In the real-time implementation, all input signals to the RAPDENS-observer are checked for validity. If a diagnostic sign is labeled valid[2], the observer uses it as shown in Section 3.2.3. However, whenever a diagnostic signal is invalid, that diagnostic signal is ignored by the observer at that step in time. This is done by excluding the signal and its entry in the forward diagnostic model (3.4) from the observer equations (see Appendix 3.B) at that time step. In a similar way, the V1 interferometer signal is ignored whenever the total ICRH power exceeds 100kW, since the ICRH system produces electromagnetic interference on the V1 electronics, rendering the V1 signal invalid.

When large pellets are injected, the H1-H5 interferometers are often rendered unusable: numerous fringe jumps occur due to pellet-induced density transients.

[2]In this context, a signal is considered valid if it has the Confidence state `good` or `corrected` and the Production state `running`. Likewise, it is considered invalid if it has Confidence state `corrupt`, `raw` or `invalid`, or has Production state `outdated`, `timeout` or `stopped`. See [Treutterer et al., 2014a].

An example of this is shown in Section 3.3.3. The H1-H5 interferometers are considered invalid when pellets injection starts.

Moreover, the validity flags of the forward interferometry matrix C_{FIR} and the signals in p, are checked. Whenever a signal is labeled invalid, the previous (valid) signal value is held.

Moreover, a detection scheme for fringe jumps is employed. The original fringe jump detection scheme developed in [Blanken et al., 2018b] did not prove successful for a set of ASDEX Upgrade discharges. This was due to two reasons: density transients (e.g. ramping density) resulted in false positive detection of fringe jumps, and fringe jumps do not present themselves as sharp step-like characteristic on the DCN signals available on the control system but represent as a transient step signal that takes a small number of samples (2 to 4 samples). Therefore a novel detection scheme was developed, which is described next.

In order to detect a fringe jump, each channel of the DCN interferometer measurements is fed through a finite impulse response filter. This filter outputs the difference between two lines fitted on two consecutive time windows. Therefore, this filter lets steps in the signal pass, but filters out ramps and filters out the moving average: slow transients of the density are filtered out, whereas the filter output is sensitive to fringe jumps.

The filter design is best understood when formulated as a least-squares minimization problem. At every cycle of the observer, two lines of equal slope are fitted on a finite history of the measurement $y_{k-2m-1}, y_{k-2m}, ..., y_k$. The line $l_1(k) = a_1 + ck$ is fitted on the measurement series $y_{k-m}, y_{k-m+1}, ..., y_k$, and the line $l_2(k) = a_2 + ck$ is fitted on the measurement series $y_{k-2m-1}, y_{k-2m}, ..., y_{k-m-1}$. Note that both series have length m and the lines have equal slope c. If the vertical distance between the lines exceeds one fringe, it is assumed that a fringe jump has occurred at time point $k - m$. This vertical distance equals $a_2 - a_1$ and is derived from the solution of the least-squares problem

$$J_k = \min_{a_1, a_2, c} \left(\sum_{i=k-m}^{k} \left(y_i - l_1(i)\right)^2 + \sum_{i=k-2m-1}^{k-m-1} \left(y_i - l_2(i)\right)^2 \right) \tag{3.5}$$

The vertical gap at time k is denoted as $a_k = a_{2,k} - a_{1,k}$ and is derived from the solution of (3.5). It is a linear combination of the measurement series $y_{k-2m-1}, y_{k-2m}, ..., y_k$. Therefore this is implemented as a finite-impulse response filter.

Finally, the estimated number of fringes that is jumped at time step k is the quotient of the division with remainder of a_k by δ and is expressed as

$$\hat{\Delta}_k = \frac{a_k - (a_k \bmod \delta)}{\delta} \tag{3.6}$$

where $\mathrm{mod}\,(\,\cdot\,)$ denotes the modulo operation, i.e. $x \bmod y$ is the remainder after division of x by y.

In the implementation on the DCS, a window length of $m = 10$ is chosen. This results in a detection delay of $m = 10$ samples, but makes the scheme robust to signal noise.

3.3.3 Experimental results of profile estimation

Profile estimation with fringe jump correction

In this section, the real-time estimation results on a ASDEX Upgrade discharge with fringe jumps is presented. In discharge #34188, two fringe jumps occur on edge interferometer channels. These are detected and corrected for, while a number of false detections occur due to fast signal transients resembling fringe jumps.

In Figure 3.3, time traces of the diagnostic signals are shown, together with the estimated measured quantities (see (3.34) of Appendix 3.B). The comparison of the estimated profiles with offline available Thomson scattering data in Figure 3.4 indicates good estimation accuracy, despite the false jump detections. The pedestal density gradient is modeled by an appropriate reduction of the diffusivity in the model, see Appendix 3.A and [Blanken et al., 2018b].

These correct and false detections are shown in more detail in Figure 3.5. The observer is able to detect and correct for the two fringe jumps, while two false detections take place in a transient phase of the discharge. This is shown in more detail in Figure 3.5. Whereas the first two jumps are detected by a clear shift of the signal, the two false detections are caused by a sudden decrease preceded by a less sudden increase. The fast signal decrease is flagged as a fringe jump.

Profile estimation and control with fault handling

In this subsection, the real-time estimation results for a high-density scenario with NBH and ICRH is presented. This scenario (see [Lang et al., 2018]) was developed to reach a central density above the Greenwald limit using feedback control on pellet fuelling. Here, the results are presented for a different discharge than in [Lang et al., 2018].

In Figure 3.6, time traces of the diagnostics as well as real-time forward estimated measured quantities are shown for ASDEX Upgrade discharge #34114. Electromagnetic interference between the ICRH launcher and the V1 interferometer causes the latter to produce invalid signals when the ICRH is on. During the pellet injection phase, all interferometers feature fringe jumps.

Depending on the scenario on ASDEX Upgrade, pellet injection causes one or more interferometers to produce fringe jumps. On the interferometer signals sampled at the DCS cycle time of 1.5ms, this fast increase resembles a fringe jump. However, not all launched pellets arrive in the plasma. Some pellets may be partially disintegrated before reaching the plasma. Also, in some cases the

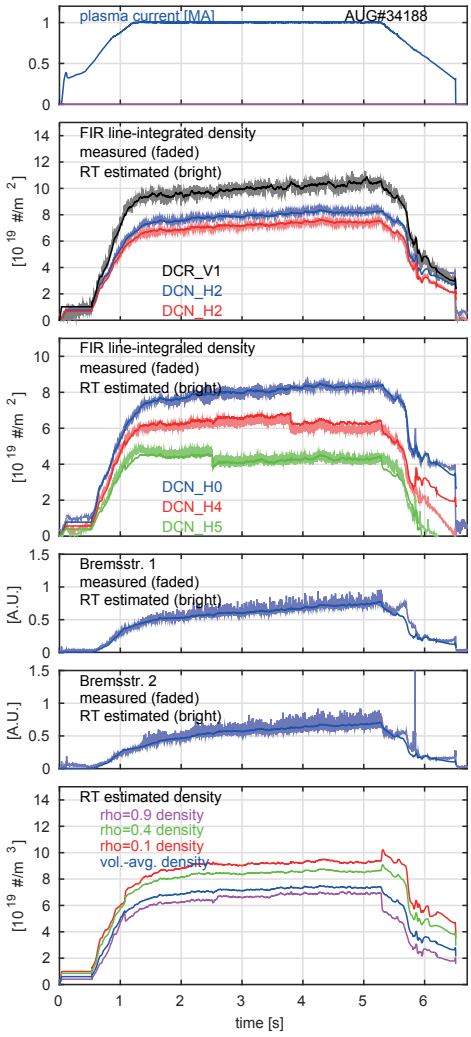

Figure 3.3 – Real-time results for AUG shot #34188. First panel: plasma current. Second to fifth panel: measured signals of the interferometers and Bremsstrahlung together with the real-time estimated diagnostics signals (computed from the estimated density profile). Sixth panel: real-time estimated density traces. Two fringe jumps occur around $t = 2.5$s and $t = 3.8$s on interferometers H5 and H4, respectively. These are detected and corrected for, as the real-time estimated forward interferometer signals follow these jumps while the estimated density is not affected. The falsely detected jumps around 5.2s and 5.9s. These affect the estimated density traces, but do not lead to significantly incorrect profiles as can be seen in Figure 3.4.

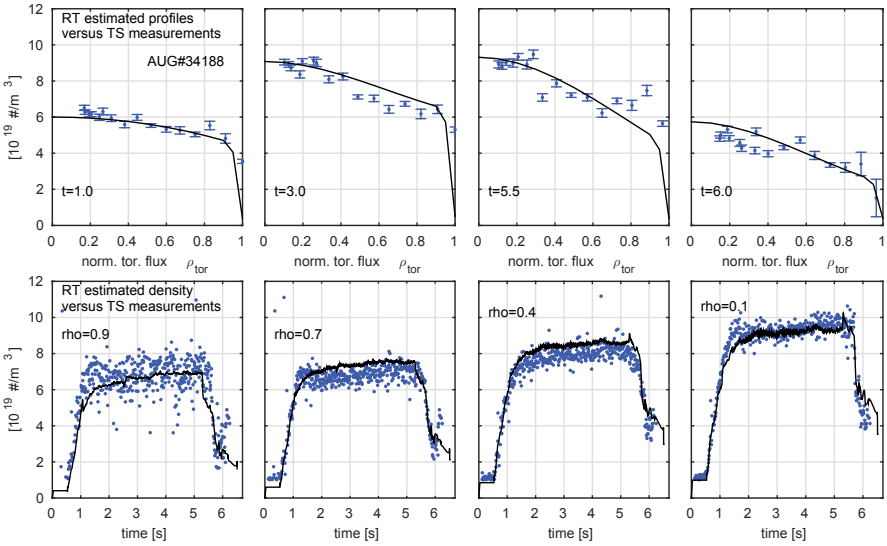

Figure 3.4 – Real-time estimated density profiles with Thomson Scattering measurements for ASDEX Upgrade shot #34188. Top row: estimated profiles at four points in time. Bottom row: time traces at four loci of the normalized toroidal flux ρ_{tor}. Despite the falsely detected fringe jumps on the edge interferometers shown in Figure 3.3, the estimated profiles show good agreement with the offline available Thomson scattering measurements.

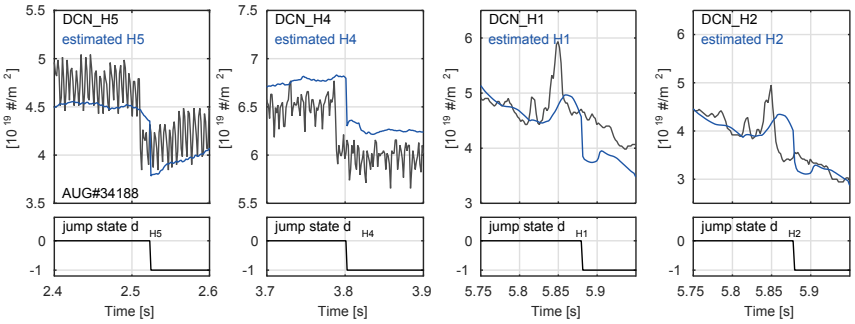

Figure 3.5 – Detailed view of detected and falsely detected fringe jumps in ASDEX Upgrade shot #34188. Top row: measured interferometer signals $y_{\mathrm{DCN},k}$ and the real-time synthetic interferometer estimates $\hat{y}_{\mathrm{DCN},k|k}$. Bottom row: estimated jump state $\hat{d}_k$. The left two columns are examples of successful fringe jump detection, while the right columns are false detections. The false detections are caused by steep transients in the interferometer signals. Note that an unavoidable delay between signal jump and detection is present.

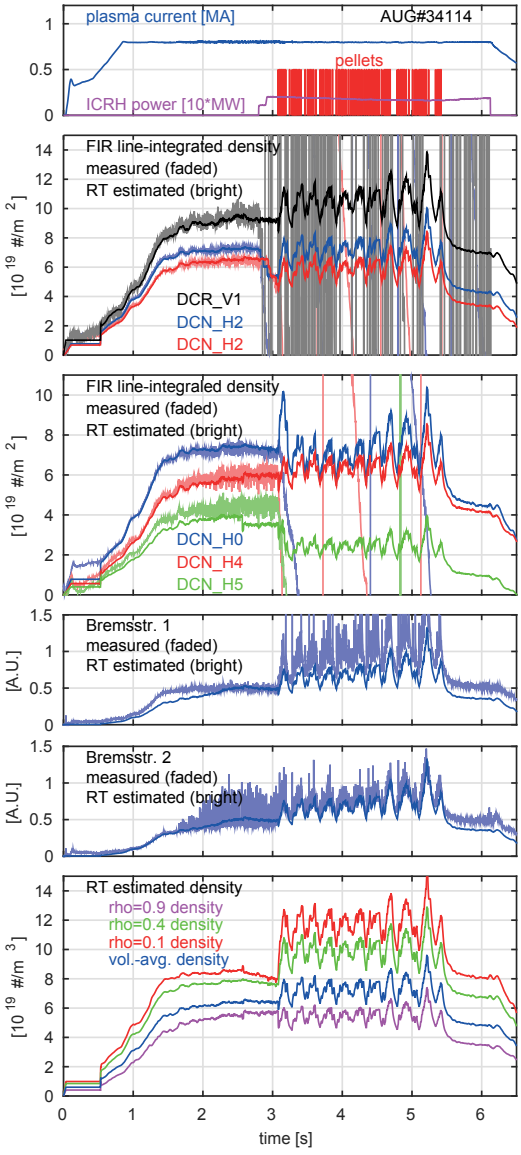

Figure 3.6 – Real-time results for ASDEX Upgrade shot #34114. Top panel: plasma current, total ICRH power and pellet firing triggers. Second to fifth panel: measured signals of the interferometers and Bremsstrahlung together with the real-time estimated diagnostics signals. Sixth panel: real-time estimated density traces.

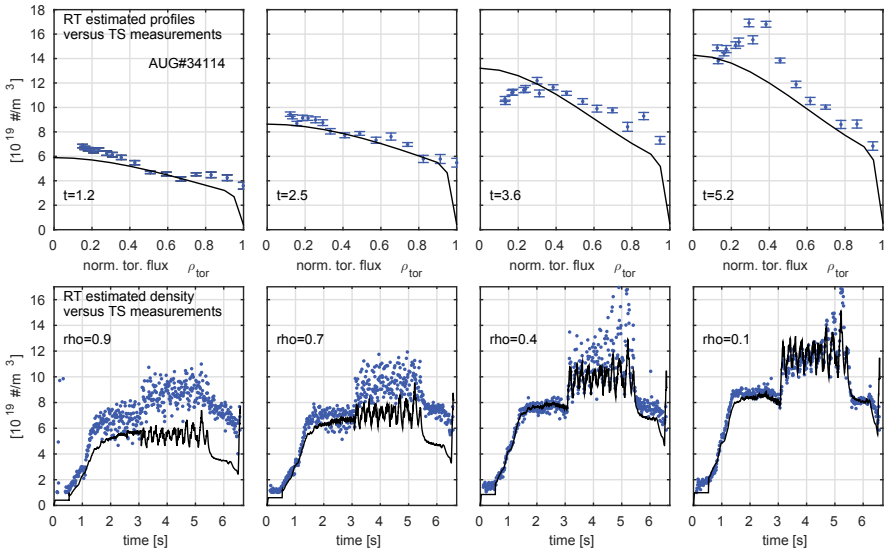

Figure 3.7 – Comparison of the real-time estimated density profiles with offline Thomson Scattering measurements for ASDEX Upgrade discharge #34114. Top row: estimated profiles at four points in time. Bottom row: time traces at four loci of the normalized toroidal flux ρ_{tor}. The estimation accuracy at the plasma core is good. However, the pedestal density is systematically underestimated. Also note that the observer cannot track the fast density profile transients due to pellet ablation.

pellet causes a change in the phase of the signal that is not detected by the electronics, yielding no signal increase despite increased line-integrated density. Effectively, this also corresponds to a fringe jump. Consequently the observer can not distinguish between two cases:

- a pellet does not reach the plasma and yields no signal increase on the interferometer,
- a pellet reaches the plasma, and yields no signal increase due to a simultaneous fringe jump that cancels out the signal increase.

On the other hand, the Bremsstrahlung diagnostic can be used for density estimation during pellet injection. The fault handling algorithm is programmed to ignore the interferometers once pellets are launched, and only the Bremsstrahlung signals are used for density estimation. Since no profile shape information can be deduced from Bremsstrahlung measurements alone, the observer relies solely on the RAPDENS model in estimating the profile shape.

In Figure 3.7, the real-time estimated density profiles at four time points and the time traces of the estimated density at four loci of the normalized toroidal

flux ρ_{tor} are shown, together with Thomson scattering data points (not available in real time at the time of writing). From the maximum density location of the Thomson scattering data in the top right panel, taken at a pellet arrival, it can be seen that the pellets ablate around $\rho = 0.3$.

From the profile plots at $t = 3.6$s and $t = 5.2$s, which is during the pellet phase, as well as the time trace of the estimated density at $\rho = 0.4$, it can be seen that the observer does not track the local density transients from pellet ablation. The observer's density estimates are only valid in a low-frequency range, since it can not track the fast transients from pellet ablation. This can be seen from the estimated density trace at $\rho = 0.4$. The high-frequency signal content originates from the Bremsstrahlung (see Figure 3.6, panel 4 and 5). Also, the profile shape estimates in the pellet injection phase rely only on the internal model and therefore does not feature the local density increase at the ablation location (see e.g. the profile estimate at $t = 5.2$s). Moreover, towards the end of the pellet phase (around $t = 5$s, see the bottom right panel), the observer underestimates the central density, as can be seen in the bottom right panel.

From the bottom left panel, it can be seen that the observer systematically underestimates the edge density. This can also be seen in the third panel of Figure 3.6, where the estimated line-integrated density for the edge line-of-sight of channel H5 is lower than measured. In Section 3.5, the performance and proposed improvements are discussed.

3.4 Density control in integrated control experiments on TCV

In this section, the design, implementation and performance of the observer and controller on TCV experiments is presented.

3.4.1 Plasma scenario and control problem

In the considered scenario, the plasma density is required to remain constant despite the presence of disturbances. The physics goal for the profile control experiment described in [Maljaars et al., 2017] is to achieve various targets for the plasma pressure and inverse safety factor profile using EC heating and current drive. The scenario is a limited L-mode at a low density of about $2 \times 10^{19} \frac{\#}{m^3}$ to maximize the EC current drive efficiency. The two available gyrotron clusters are aimed at the magnetic axis.

The density controller aims to make the average electron density track a reference. This reference density consists of a ramp followed by a step toward a constant. This constant is the desired density during for the profile control experiment. Reference tracking is to be achieved by a feedback controller using gas injection as the actuator. The controller should:

- minimize the tracking error $e = x_{\mathrm{ref}} - x_{\mathrm{c}}$ up to a bandwidth of 20Hz,
- reject disturbances from MHD activity and EC heating and current drive,
- be robust against model mismatches in the model-based tuning procedure.

The controlled quantity is provided in real time by the observer. This observer should:

- minimize the profile estimation error,
- detect and correct for measurement faults,
- be robust against model mismatches.

Moreover, the observer and controller should stay within the available computational time per 1ms cycle time of the real-time computer (see Section 3.4.3). The controller has command over one gas valve. The valve can handle an input voltage between 0V and 10V, yielding a (nonnegative) gas flow into the vacuum vessel. The mapping between input voltage u_{valve} and mass flow Γ_{valve} has been determined in calibration experiments. This nonlinear function is strictly increasing and can be written as $\Gamma_{\mathrm{valve}} = v(u_{\mathrm{valve}})$.

3.4.2 Feedback controller design

The feedback controller is designed using the model-based robust H_∞ design formalism [Morari and Zafiriou, 1989]. This approach enables to design the control law based on a linear plant model and requirements for the closed-loop response, and therefore requires minimal experimental time dedicated to controller tuning. Moreover, the robust H_∞ control method allows to account for uncertainties in the plant dynamics. Regarding the density dynamics, these uncertainties are formed by shot-to-shot differences in machine conditions, unmodeled (nonlinear) effects and coupling to plasma physics other than solely the density dynamics.

Robust control design procedure

The main ingredients and outcome of the design procedure are stated next, while the details are provided in Appendix 3.C.

The nonlinear continuous-time dynamics (3.18) are linearized around a nominal operating point (x_0, p_0). Uncertainties in the steady-state response and time scales of the dynamics are captured by including static variability in certain parameters and coefficients of the model (3.18). These are listed in Table 3.1.

A set of weighting functions that express the required closed-loop responses are specified by the user. These weighting functions impose zero steady-state tracking and disturbance rejection by penalizing the response of the closed-loop transfer functions in certain frequency ranges. The robust H_∞ design procedure for the linear feedback controller subject to the uncertain linearized plant model and the weighting functions is given in Appendix 3.C.3. It is a proportional-integral (PI) controller with additional high-frequency roll-off. The frequency response of the controller is shown in Figure 3.13.

Anti-windup compensation

Since the actuation input (the gas valve mass flow) is constrained by a lower limit and an upper limit, an anti-windup scheme has to be employed. This scheme prevents oscillations of the actuation signal (and consequently the plasma density) when the controller has saturated the actuation signal at one of its limits.

The controller (3.39) is implemented as

$$u_k = a u_{k-1} + (1-a)(K_\mathrm{P} e_k + u_{\mathrm{I},k}) \tag{3.7}$$

where K_P is the proportional gain and $a = \exp(-f_\mathrm{rolloff} T_\mathrm{s})$ where f_rolloff is the roll-off frequency and T_s is the cycle/sample time. The anti-windup is implemented in the formulation of the integral action $u_{\mathrm{I},k}$, which is evaluated as

$$u_{\mathrm{I},k} = \begin{cases} u_{\mathrm{I},k-1} + K_\mathrm{I} T_\mathrm{s} e_k & u_\mathrm{min} < u_{k-1} < u_\mathrm{max} \\ u_{\mathrm{I},k-1} & u_\mathrm{min} > u_{k-1} \vee u_{k-1} > u_\mathrm{max} \end{cases} \tag{3.8}$$

where K_I is the integral gain. Here, the integration of the error e is halted when the actuator input u is saturated.

3.4.3 Implementation on the TCV control system

The controller and the observer (described in Section 3.2) are implemented on the SCD [Anand et al., 2017], the digital control system of TCV.The observer and controller are designed in the dedicated software environment for development, testing and experimental use of control algorithms [Maljaars et al., 2017].

All real-time software is programmed in MATLAB Simulink [The Mathworks Inc., a], which allows for automated code generation for real-time use [Felici et al., 2014b]. It is worth to note that the code underlying the observer equations is the same on ASDEX Upgrade and TCV, whereas only the machine-specific diagnostic models and settings differ between the machines. This greatly enhances portability to other implementations.

An overview of the observer and controller implementation on the SCD is given in Figure 3.8. The observer is connected to other real-time algorithms. First, the real-time equilibrium reconstruction code LIUQE [Moret et al., 2015] provides equilibrium geometry information to the RAPTOR-observer and the profile controller, as well as the interferometry matrix to the density observer. Second, the real-time RAPTOR-observer [Felici et al., 2011, 2014a] provides the estimated edge electron temperature. This is estimated by merging soft X-ray measurements of the central electron temperature with the RAPTOR model in an Extended Kalman filter scheme. Also, it estimates the plasma pressure and safety factor profile for the profile controller [Maljaars et al., 2017]. Last, the measured plasma current is provided [Moret et al., 2015]. The real-time algorithms on the SCD mentioned above are run at a cycle time of 1ms.

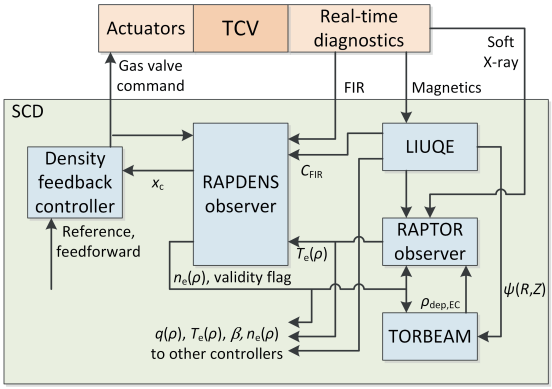

Figure 3.8 – Block diagram of the density observer and controller as implementated on the SCD. Also shown are the RAPTOR-observer and the real-time equilibrium reconstruction code LIUQE. The latter provides the interferometry matrix to the observer. Note that the profile controller for control of the plasma pressure and safety factor profile is not displayed for simplicity.

Forward diagnostics model

The TCV interferometry system measures the line-integrated electron density along fourteen vertical lines of sight [Barry et al., 1998]. These lines of sight range from (nearly) intersecting the magnetic axis to intersecting the plasma edge, both on the high and low field side. Similar to (3.4), the forward diagnostics model can be written in the form of (3.3) as

$$y = C_{\mathrm{FIR}} x + \delta d \tag{3.9}$$

where $C_{\mathrm{FIR}}^{(i,j)} = \int_{L_i} \Lambda_j dL$ where L_i is the line of sight of channel i, δ is the line-integrated density corresponding to one fringe, and d is the cumulative number of fringe jumps. The matrix C_{FIR} is computed by a postprocessing routine in the implementation of LIUQE [Moret et al., 2015] on the SCD.

Fault handling

The signals originating from the RAPTOR observer and LIUQE (see Figure 3.8) are checked for validity. For example, if LIUQE has convergence issues (reported by a dedicated output signal) the density observer holds the interferometry matrix C_{FIR}, plasma volume V_{p}, and X-point presence indicator c_{LD} to their previous valid values.

In order to filter out fringe jumps, the innovation residual z_k of the observer (see Appendix 3.B) is fed through a filter that removes multiples of one fringe. This fringe jump correction scheme is documented in [Blanken et al., 2018b].

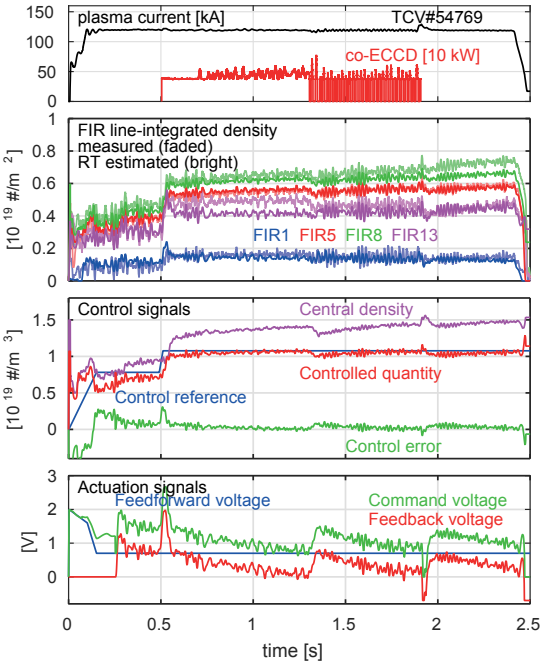

Figure 3.9 – Real-time results for TCV discharge #54769. First panel: plasma current. Second panel: measured interferometer signals and estimated line-integrals (computed from the estimated density profile). Third panel: controlled variable, reference, central density and control error. Fourth panel: feedforward, feedback and command (feedforward plus feedback) signals for the gas valve. In this experiment, the density averaged over ρ_v is controlled by a combination of feedforward and feedback. At $t = 0.25$s, the feedback controller introduced in Section 3.4.2 is activated. The estimated density profiles and Thomson scattering data are shown in Figure 3.10.

3.4.4 Experimental results of density control

In this subsection, the results of the observer and controller are presented. In these experiments the density is required to stay constant while EC heating and current drive is used to control the plasma pressure and safety factor profile (see [Maljaars et al., 2017]). The controlled variable x_c is selected to be the electron density averaged over $\rho_\mathrm{v} = \sqrt{\frac{V}{V_\mathrm{p}}}$, i.e. $\bar{n}_\mathrm{e} = \int_0^1 n_\mathrm{e}\, d\rho_\mathrm{v} = \frac{1}{2\sqrt{V_\mathrm{p}}} \int_0^1 \frac{n_\mathrm{e}}{V} \frac{\partial V}{\partial \rho_\mathrm{tor}} d\rho_\mathrm{tor}$. This quantity is somewhat equivalent to a line-average (as commonly derived from interferometry measurements), yet is not dependent on the machine-specific interferometer geometry.

In TCV discharge #54769, the feedback controller is activated at $t = 0.25$s.

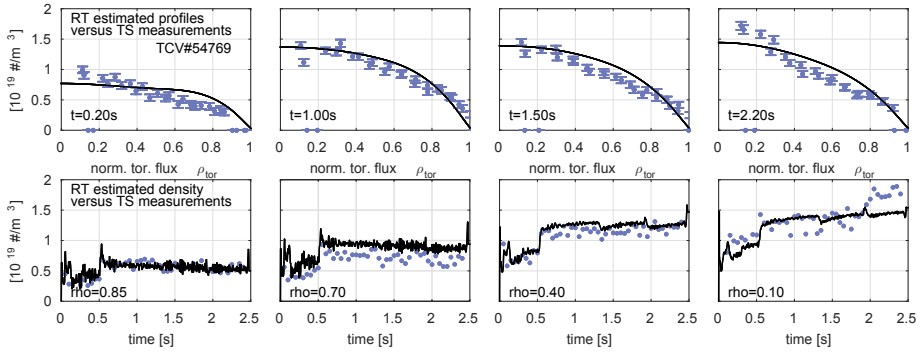

Figure 3.10 – Real-time estimated density profiles with offline Thomson Scattering measurements for TCV shot #54769. Top row: estimated profiles at four points in time. Bottom row: time traces at four loci of the normalized toroidal flux ρ_{tor}. The agreement between the estimated density and Thomson scattering data is good, despite an error in the overall profile shape. This can be attributed to the accuracy of the chosen transport and source models (see Section **??**) as well as unknown errors in the evaluation of line-integrals from real-time reconstructed equilibria.

The legacy controller [Vijvers et al., 2012] is active between 0.1s and 0.25s. A model-predictive controller [Maljaars et al., 2017] is used to control the safety factor profile using one EC cluster driving co-current. In Figure 3.9, the plasma current, EC powers and interferometry signals are shown, together with the real-time estimations from the observer. Also, the control reference and gas valve commands are shown. After initial transients, a zero tracking error e is achieved. In Figure 3.10, the real-time estimated density profiles and the time traces of the estimated density at four loci of the normalized toroidal flux ρ_{tor} are shown, together with Thomson scattering data points. These comparisons show that the observer provides an estimate with good accuracy.

In TCV discharge #55117, the feedback controller is activated at $t = 0.2$s. A controller originally developed for ITER is used (see [Kim et al., 2016]) to control the plasma pressure using one EC cluster driving co-current. In Figure 3.11, the plasma current, EC powers, rotating mode markers and interferometry signals are shown, together with the real-time estimations from the observer. Also, the control reference and gas valve commands are shown. In Figure 3.12, the real-time estimated density profiles and the time traces of the estimated density at four loci of the normalized toroidal flux ρ_{tor} are shown, together with Thomson scattering data points.

After initial density transients, the tracking error e decays to zero in the flat-top phase. At $t = 1.77$s, a rotating mode forms. The resulting thermal confinement deterioration prompts the pressure controller to increase the EC

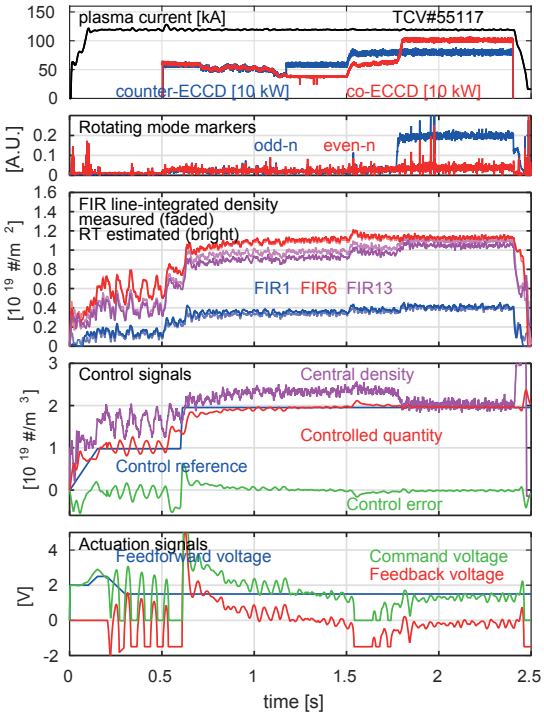

Figure 3.11 – Real-time results for TCV discharge #55117. First panel: plasma current. Second panel: presence markers of rotating modes. Third panel: measured interferometer signals and estimated line-integrals (computed from the estimated density profile). Fourth panel: controlled variable, reference, central density and control error. Fifth panel: feedforward, feedback and command signals for the gas valve. Again, the density averaged over ρ_v is controlled by a combination of feedforward and feedback. From the start of the discharge until $t = 0.25$s, the legacy density controller is active. At $t = 0.25$s, the feedback controller introduced in Section 3.4.2 is activated. The control error decreases to zero for the duration of the discharge. The estimated density profiles and Thomson scattering data are shown in Figure 3.12.

heating. At the same time, a change in the density profile shape is observed on the interferometers, as the HFS edge interferometer (#13) increases while a central and the LFS edge interferometer (#6 and #1, respectively) do not. The observer interprets this as a slightly hollow profile (see the profile at $t = 2.0$s in Figure 3.12). Interestingly, the Thomson scattering data does not show a similar hollow profile.

Between $t = 0.2$s and $t = 0.5$s, oscillations are seen in the interferometry measurements, estimated density as well as the feedback actuation. After the

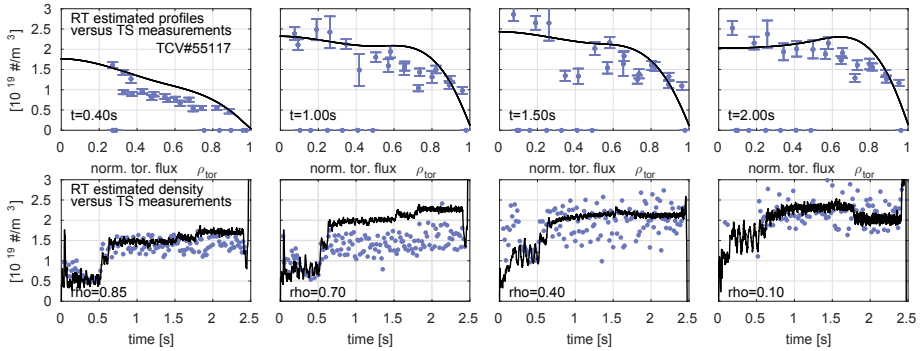

Figure 3.12 – Real-time estimated density profiles with offline Thomson Scattering measurements for TCV shot #55117. Top row: estimated profiles at four points in time. Bottom row: time traces at four loci of the normalized toroidal flux ρ_{tor}.

EC heating switches on, these oscillations are smaller and decay. Note that the oscillation are not caused by integrator windup, as it takes one period of the oscillation before the actuation command signal saturates at 0V for the first time. Multiple reasons could cause such oscillations.

- The feedback controller gains could be too aggressive for the plasma response in the ohmic phase. The gains prove satisfactory in the EC-heated phase, where the oscillation is much smaller. Note that the controller is tuned on a linearized model (see Appendix 3.C.3), linearized at an operating point in the EC-heated phase.
- The plasma dynamics of the pressure and density are coupled. The interconnection of the state observers and controllers for the pressure and density, as well as their respective computational delays, could cause the two feedback loops to become oscillatory.

Additional results of discharges with the same scenario, pressure and safety factor profile control, and density control can be found in [Maljaars et al., 2017; Mavkov et al., 2018].

3.5 Discussion

In this section, we provide a discussion of the estimation and control performance in experiments that are shown in Section 3.3 and Section 3.4.

3.5.1 Profile estimation accuracy

In Section 3.3 and 3.4, we have shown good agreement between the real-time estimated density profiles and offline Thomson Scattering measurements.

In the high-density pellet-fuelled experiments on ASDEX Upgrade, the observer systematically underestimates the edge density and does not track fast local density transients due to pellet ablation. Since many interferometers give invalid signals in this experiment, the estimate is based on a limited set of Bremsstrahlung measurements. The underestimation did not prove harmful for the experimental goal.

Moreover, the systematic integration of multiple diagnostics in a real-time estimator is novel in present-day tokamaks and will be essential in ITER and DEMO due to scarce diagnostics and harsh environment. Future addition of real-time Thomson scattering measurements can alleviate the discrepancy at the edge.

3.5.2 Control performance

The real-time estimated central density proved essential for the feedback control in the high density scenarios on ASDEX Upgrade (see [Lang et al., 2018]). The central density was maintained above the Greenwald limit for more than 2s. While alternative real-time reconstructions of the central density proved unreliable in earlier discharges (see [Lang et al., 2012, 2018]), the estimation accuracy of the proposed method is better and sufficient for the purpose of control in this experiment.

In experiments on the simultaneous control of density, pressure and safety factor profile on TCV, the feedback controller was tuned a priori using the modeled plasma response of the actuator to the controlled variable. Such a model-based tuning practice is advised for ITER and DEMO, where experimental time can not be used for controller tuning by trial and error.

Although strict requirements for control performance are not yet formed, the controller algorithms proved successful for the experimental goals.

3.5.3 Future extensions

The accuracy and robustness of real-time estimated profiles, both in the plasma core and in the edge, can be enhanced by incorporating additional diagnostics, as well as improved transport modeling. While modeling accuracy of particle transport internal to the plasma has progressed in recent years [Angioni et al., 2009], the real-time capable self-consistent modeling of recycling and pumping is still not well understood and currently requires large-scale simulations using numerical codes such as SOLPS [Wiesen et al., 2015].

The inclusion of real-time available Thomson scattering measurements on ASDEX Upgrade and TCV will greatly improve the profile estimation accuracy.

In particular, a Thomson scattering measurement sample fired after a pellet launch can prove useful for correcting any fringe jumps on the interferometers. Also, the inclusion of real-time dedicated plasma edge diagnostics will improve accuracy and robustness of the estimation of the pedestal density gradient, which is important for e.g. bootstrap current estimation.

3.6 Conclusions

Reliable real-time plasma density profile estimation is essential for the operation of next-generation tokamaks and nuclear fusion reactors. An integrated solution using all available yet scarce diagnostics should be in place to provide an accurate estimate of the electron density profile in real time. This is crucial for density control, and valuable for determining diagnostics validity and actuation constraints (e.g. ECE, ECH cut-off), and control loops for pressure and MHD.

In this paper, the successful results of a real-time density profile estimator and diagnostic fault handling algorithm in experiments on ASDEX Upgrade and TCV are presented. This observer uses multiple diagnostics and can deal with various diagnostic faults. In ASDEX Upgrade discharges on high-density pellet fuelling, the observer provides good agreement with offline Thomson scattering measurements, and provides a reliable estimate of the controlled core density for the feedback controller. In TCV discharges on integrated pressure, iota and NTM control, the density controller provides a constant density despite disturbances from time-varying ECCD power. Here also, the real-time estimated density profile shows sufficiently good agreement with Thomson scattering measurements. Shortcomings in estimation quality can be attributed to limitations of the model as well as unmodeled diagnostics characteristics.

The observer has well-defined validity limits. The estimation accuracy deteriorates when these limits are exceeded. False positives of fringe jumps occur when the signal resembles one. Also, pellet-induced transients and fringe jumps are inherently difficult to distinguish. Future work on pellet modeling and real-time pellet arrival detection can solve these difficulties.

On the one hand, given this experience, it will be important for ITER that the real-time estimated density is based on all available diagnostics to achieve accuracy, reliability and redundancy. On the other hand, future modeling advances and knowledge gained from ITER will allow real-time density estimation from a more limited set of diagnostics, such as is the case on DEMO.

3.7 Acknowledgments

This work has been carried out within the framework of the EUROfusion Consortium and has received funding from the EURATOM research and training

programme 2014-2018 under grant agreement No 633053. The views and opinions expressed herein do not necessarily reflect those of the European Commission. This work was supported in part by the Netherlands Organization for Scientific Research via F. Felici's VENI grant "Control of plasma profiles in a fusion reactor" (no. 680.47.436). This work was supported in part by the Swiss National Science Foundation.

Appendix

3.A Equation summary of RAPDENS model

In this appendix, a summary of the RAPDENS equations, governing the evolution of the plasma electron density, and its spatial and temporal discretization is given.

The evolution of the plasma density $n_e\left(\rho,t\right)$ is modeled by mass conservation and radial transport [Hinton and Hazeltine, 1976] on the domain $0<\rho<\rho_{\mathrm{e}}$ as

$$\left(\frac{\partial V}{\partial\rho}\right)^{-1}\frac{\partial}{\partial t}\left(n_{\mathrm{e}}\frac{\partial V}{\partial\rho}\right)+\left(\frac{\partial V}{\partial\rho}\right)^{-1}\frac{\partial\Gamma_{\mathrm{e}}}{\partial\rho}=S_{\mathrm{e}} \tag{3.10}$$

where $\rho=\sqrt{\Phi/\left.\Phi\right|_{\mathrm{LCFS}}}$ is the radial variable associated with the toroidal flux, $\rho_{\mathrm{e}}>1$ is an artificially extended boundary to include a scrape-off layer volume (see [Blanken et al., 2018b]) and $\frac{\partial V}{\partial\rho}$ is the radial volume derivative. The radial transport flux $\Gamma_{\mathrm{e}}\left(\rho,t\right)$ is modeled as

$$\Gamma_{\mathrm{e}}=-\frac{\partial V}{\partial\rho}\left(\left\langle\left(\nabla\rho\right)^{2}\right\rangle\chi\frac{\partial n_e}{\partial\rho}+\left\langle\left|\nabla\rho\right|\right\rangle\nu n_e\right) \tag{3.11}$$

where χ is the diffusivity and ν is the drift velocity. The boundary conditions for (3.10) are $\left.\frac{\partial n_e}{\partial\rho}\right|_{\rho=0}=0$ and $\left.n_e\right|_{\rho=\rho_{\mathrm{e}}}=0$. The net electron source $S_{\mathrm{e}}\left(\rho,t\right)$ is modeled as

$$S_{\mathrm{e}}=\ \left\langle\sigma v\right\rangle_{\mathrm{iz}}n_n n_e-\left\langle\sigma v\right\rangle_{\mathrm{rec}}n_e n_i-\frac{\left.n_e\right|_{\rho>1}}{\tau_{\mathrm{SOL}}}+S_{\mathrm{pellet}}+S_{\mathrm{NB}} \tag{3.12}$$

where $\left\langle\sigma v\right\rangle_{\mathrm{iz}}\left(T_{\mathrm{e}}\right)$ and $\left\langle\sigma v\right\rangle_{\mathrm{rec}}\left(T_{\mathrm{e}}\right)$ are the temperature-dependent ionization and recombination cross-sections [Wesson, 2004], and τ_{SOL} is the time constant for particle loss through the scrape-off layer. These sources and sinks arise from particle flows between the plasma, the vacuum and the wall. The evolution of the neutral vacuum density $n_{\mathrm{n}}\left(t\right)$ and wall inventory $N_{\mathrm{w}}\left(t\right)$ are modeled as

$$\frac{dN_{\mathrm{w}}}{dt}=\ -\frac{N_{\mathrm{w}}-c_w V_{\mathrm{v},0}n_{\mathrm{n}}}{\tau_{\mathrm{release}}}+\left(1-\frac{N_{\mathrm{w}}}{N_{\mathrm{sat}}}\right)\int_{V_{\mathrm{SOL}}}\frac{n_e}{\tau_{\mathrm{SOL}}}dV \tag{3.13}$$

$$V_{\mathrm{v}}\frac{dn_{\mathrm{n}}}{dt} = \begin{array}{l} \frac{N_{\mathrm{w}}-c_w V_{\mathrm{v},0} n_{\mathrm{n}}}{\tau_{\mathrm{release}}} + \frac{N_{\mathrm{w}}}{N_{\mathrm{sat}}}\int_{V_{\mathrm{SOL}}} \frac{n_e}{\tau_{\mathrm{SOL}}} dV \\ + \int_{V_{\mathrm{p}}} \left(\langle\sigma v\rangle_{\mathrm{rec}} n_e n_i - \langle\sigma v\rangle_{\mathrm{iz}} n_n n_e\right) dV \\ - \frac{n_{\mathrm{n}} V_{\mathrm{v},0}}{\tau_{\mathrm{pump}}} + \Gamma\big|_{\rho_{\mathrm{e}}} + \Gamma_{\mathrm{valve}} \end{array} \tag{3.14}$$

where τ_{release} is the particle release rate from the wall, N_{sat} is the inventory at which the wall is saturated, τ_{pump} is the pumping time scale, $c_w V_{v,0}$, V_{v} is the vacuum volume and $V_{\mathrm{SOL}} = \int_1^{\rho_e} \frac{\partial V}{\partial \rho} d\rho$.

The equilibrium-related quantities are parametrized as

$$\frac{\partial V}{\partial \rho} = 2\, V\big|_{\mathrm{LCFS}}(t)\, \rho \tag{3.15}$$

$$\left\langle (\nabla\rho)^2 \right\rangle = (g_1 - 1)\, \rho^{g_3} + 1 \tag{3.16}$$

$$\langle |\nabla\rho| \rangle = (g_2 - 1)\, \rho^{g_4} + 1 \tag{3.17}$$

where $g_1 = \left\langle (\nabla\rho)^2 \right\rangle\Big|_{\mathrm{LCFS}}$, $g_2 = \langle |\nabla\rho| \rangle\big|_{\mathrm{LCFS}}$, g_3 and g_4 are derived from a fixed equilibrium. Also, distributed time-varying quantities are parametrized as e.g. $S_{\mathrm{NB}} = \Lambda_{\mathrm{NB}}(\rho)\, \Gamma_{\mathrm{NB}}(t)$, and similar for the pellet deposition S_{pellet} and the neutral density n_{n} in the plasma, see also [Blanken et al., 2018b].

A system of ordinary differential equations (ODE) is constructed in [Blanken et al., 2018b] by parametrizing the spatial dependency of the electron density $n_e(\rho, t)$ (as expressed in equation (3.1)) using cubic splines [de Boor, 2001] and applying a finite-element method (see e.g. [Hughes, 1987]) to (3.10), (3.13) and (3.14). This system of ODEs is written as

$$\frac{dx}{dt} = g(x, p, u) \tag{3.18}$$

where $x(t)$ is the state vector containing $N_{\mathrm{w}}(t)$, $n_{\mathrm{n}}(t)$ and the parametrization coefficients for $n_e(\rho, t)$, $u(t) = [\Gamma_{\mathrm{valve}}(t)\ \Gamma_{\mathrm{NB}}(t)\ \Gamma_{\mathrm{pellet}}(t)]^{\mathrm{T}}$ is the input vector and $p(t)$ is the parameter vector, containing time-varying quantities I_{p}, T_e, V_{LCFS}, c_{LD}, c_{LH}, see [Blanken et al., 2018b]. A backward Euler scheme with constant time step T_{s} is employed to transform (3.18) to the nonlinear[3] discrete-time equation

$$f(x_k, x_{k-1}, p_{k-1}, u_{k-1}) = -T_{\mathrm{s}} g(x_k, p_{k-1}, u_{k-1}) + x_k - x_{k-1} = 0 \tag{3.19}$$

where $x_k = x(t_k)$ denotes the time-discretized vector and $t_k = t_0 + kT_{\mathrm{s}}$, $k = 0, 1, \cdots, t_{\mathrm{f}}/T_{\mathrm{s}}$. Linearizations of both g in (3.18) and f in (3.19) can be analytically derived. In the applications described in this paper, equation (3.19) is solved using a Newton-Raphson method.

[3] Note that for the modeling presented in this paper, the function g in (3.18) is in fact linear with respect to u.

3.B Equation summary of the observer equations

In this appendix, the observer equations based on an Extended Kalman filter for the RAPDENS dynamical model (3.19) and measurement equation (3.3) are stated.

3.B.1 Augmented system equations

The state of the system (which is to be estimated by the observer) is composed of three vectors. In the Kalman filter formalism, the state evolution and measurement are assumed to be corrupted by stochastic noise. The three parts of the state and the respective stochastic noise terms are listed below.

1. The first part is the state x_k of the RAPDENS dynamics (3.19). A term w_k^{x} is added in order to handle model uncertainties that influence the state evolution. This term is assumed to be a zero-mean white noise with covariance Q_k^{x}.
2. The second part is the vector of coefficients ζ_k in (3.3). In Section 3.3.2, ζ_k is assumed to be slowly changing with respect to the state of the system. This allows them to be estimated by the observer. It is assumed to have random walk dynamics as expressed by $\zeta_k = \zeta_{k-1} + w_k^{\mathrm{z}}$, where w_k^{z} is assumed to be zero-mean white noise with covariance Q_k^{z}.
3. The third part is the number of fringe jumps on each channel of the interferometry system (see Section 3.3.2 and Section 3.4.3). It must be stored over time in order to compensate the measurement y_{FIR} at every time step following such a jump. In Section 3.3.2, the influence of fringe jumps on the interferometry measurements is written as an additive term δd_k, where δ is a constant. This state vector d_k accumulates the jumps on each channel as $d_k = d_{k-1} + \Delta_{k-1}$, where $\Delta_k \in \mathbb{N}$. For example, a downward fringe jump on channel i at time t_k is represented by $\Delta_k^{(i)} = -1$.

Summarizing, the equations governing the state transitions are

$$f\left(x_k, x_{k-1}, p_{k-1}, u_{k-1}\right) - \frac{\partial f}{\partial x_k} w_{k-1}^{\mathrm{x}} = 0 \tag{3.20}$$

$$\zeta_k = \zeta_{k-1} + w_{k-1}^{\mathrm{z}} \tag{3.21}$$

$$d_k = d_{k-1} + \Delta_k \tag{3.22}$$

Note that in (3.20), the additive term w_k^{x} is multiplied by the derivative of f to x_k. If f would be linear with respect to its arguments, as is the case for linear dynamical systems, then the usual state-space form with additive term as used in e.g. [Anderson and Moore, 1979] is recovered. This implies that (3.20)

represents a nonlinear state transition with additive noise, as is assumed in the Extended Kalman filter formalism [Anderson and Moore, 1979].

The measurement is assumed to be corrupted by a zero-mean noise v_k with covariance R_k, and is given by

$$y_k = h\left(x_k, \zeta_k\right) + \delta d_k + v_k \tag{3.23}$$

where the additive terms w_k^{x}, w_k^{z} and v_k are assumed to be zero-mean white noise with covariances Q_k^{x}, Q_k^{z} and R_k, respectively.

The Extended Kalman filter relies on local linearizations of the relevant dynamics and measurement relation. For the purpose of readability later on, three functions related to local linearizations of (3.20) and (3.23) are defined as $\tilde{f}\left(x_k, x_{k-1}, p_{k-1}\right) = -\left(\frac{\partial f}{\partial x_k}\Big|_{x_k, p_{k-1}} \right)^{-1} \frac{\partial f}{\partial x_{k-1}}\Big|_{x_{k-1}, p_{k-1}}$, $\tilde{h}_{\mathrm{x}}(x_k, \zeta_k) = \frac{\partial h}{\partial x}\big|_{x_k, \zeta_k}$ and $\tilde{h}_{\mathrm{z}}(x_k, \zeta_k) = \frac{\partial h}{\partial \zeta}\Big|_{x_k, \zeta_k}$. Moreover, an augmented state is defined by stacking x_k and ζ_k as $\boldsymbol{x}_k = \begin{bmatrix} x_k^T & \zeta_k^T \end{bmatrix}^T$.

3.B.2 Observer equations based on an Extended Kalman filter

The observer equations consist of two distinctive parts: the model-based state prediction and the measurement-based state update. The state prediction step is based on (3.20)-(3.22) and is given by

$$f\left(\hat{x}_{k|k-1}, \hat{x}_{k-1|k-1}, p_{k-1}, u_{k-1}\right) = 0 \tag{3.24}$$

$$\hat{\zeta}_{k|k-1} = \hat{\zeta}_{k-1|k-1} \tag{3.25}$$

$$\hat{d}_{k|k-1} = \hat{d}_{k-1|k-1} \tag{3.26}$$

The covariance matrix $P_{k|k-1}$ of the prediction error of the augmented state $\hat{\boldsymbol{x}}_{k|k-1}$ is given by

$$P_{k|k-1} = F_{k-1} P_{k-1|k-1} F_{k-1}^T + Q_{k-1} \tag{3.27}$$

where the matrix F_k is derived from a local linearization of (3.20) and is given by

$$F_{k-1} = \begin{bmatrix} \tilde{f}\left(\hat{x}_{k|k-1}, \hat{x}_{k-1|k-1}, p_{k-1}\right) & 0 \\ 0 & I \end{bmatrix}$$

where I is the identity matrix and Q_k is a block-diagonal matrix with blocks Q_k^{x} and Q_k^{z}.

In the update step, the predicted estimate is adjusted according the measurement sample y_k. The innovation residual z_k is the difference between the measurement sample and the prediction of the measured quantity. The latter is

computed on the output equation (3.23). The innovation residual, its covariance matrix S_k and the *near-optimal* Kalman gain L_k are given by

$$z_k = y_k - h\left(\hat{x}_{k|k-1}, \hat{\zeta}_{k|k-1}\right) - \delta\hat{d}_{k|k-1} \tag{3.28}$$

$$S_k = R_k + H_k P_{k|k-1} H_k^T \tag{3.29}$$

$$L_k = P_{k|k-1} H_k^T \mathbb{S}_k^T \left(\mathbb{S}_k S_k \mathbb{S}_k^T\right)^{-1} \tag{3.30}$$

where the matrix H_k is derived from local linearizations of (3.23) and is given by $H_k = \left[\tilde{h}_{\mathrm{x}}\left(\hat{x}_{k|k-1}, \hat{\zeta}_{k|k-1}\right) \quad \tilde{h}_{\mathrm{z}}\left(\hat{x}_{k|k-1}, \hat{\zeta}_{k|k-1}\right)\right]$ and $\mathbb{S}_k$ is a selection matrix. Its purpose is discussed later on.

Finally, the updated estimate $\hat{\boldsymbol{x}}_{k|k}$ of the augmented state, its covariance matrix $P_{k|k}$ and the estimated fringe jump state $\hat{d}_{k|k}$ are given by

$$\hat{\boldsymbol{x}}_{k|k} = \hat{\boldsymbol{x}}_{k|k-1} + L_k \mathbb{S}_k \left(z_k - \delta\hat{\Delta}_k\right) \tag{3.31}$$

$$\hat{d}_{k|k} = \hat{d}_{k|k-1} + \hat{\Delta}_k \tag{3.32}$$

$$P_{k|k} = \left(I - L_k \mathbb{S}_k H_k\right) P_{k|k-1} \tag{3.33}$$

where $\hat{\Delta}_k$ is the vector of the estimated number of fringes jumped at time k at each interferometer channel. The expressions for $\hat{\Delta}_k$ on the ASDEX Upgrade implementation is given in equation (3.6), whereas for the TCV case it is given in [Blanken et al., 2018b].

In the diagnostic fault handling scheme of Section 3.3.2, at each time step k the validity of a measurement is assessed. If invalid, the measurement must be ignored by the observer in the update step. This is accomplished in the observer equations by a selection matrix $\mathbb{S}_k$ in equations (3.30), (3.31) and (3.33). The matrix $\mathbb{S}_k$ is constructed at every time step k by taking an identity matrix with the dimension of the total number of measurement channels and removing the rows corresponding to the invalid channels. The selection matrix $\mathbb{S}_k$ ensures that the state estimate is only updated using valid measurements in (3.31) and (3.33). Note that this implies that the Kalman gain matrix L_k constructed in (3.30) and $\mathbb{S}_k$ have time-varying dimensions.

In the observer implementations described in Section 3.3.2 and Section 3.4.3, the recursive equations (3.24)-(3.33) are computed at every cycle step. This is illustrated in Figure 3.1.

In the figures of Section 3.3.3, 3.3.3 and 3.4.4, estimated diagnostics signals are shown. These are evaluated using (3.23) as

$$\hat{y}_{k|k} = h\left(\hat{x}_{k|k}, \hat{\zeta}_{k|k}\right) + \delta\hat{d}_{k|k} \tag{3.34}$$

and represent the expected diagnostic signal based on the updated state estimates of (3.31) and (3.32).

Table 3.1 – Nominal values and uncertainty interval of uncertain coefficients and parameters in the model (3.18) for the TCV target scenario.

Coefficient / parameter	Unit	Nominal value with uncertainty interval
$\tau_{\mathrm{SOL}\to\mathrm{wall}}$	s	$2.3 \times 10^{-4} \pm 30\%$
b	$\frac{\#e}{\mathrm{s}} \frac{\mathrm{Ls}}{\mathrm{mbar}}$	$2.47 \pm 10\%$
N_{sat}	#e	$2.5 \times 10^{19} \pm 50\%$
$T_{\mathrm{e}}(\rho = 1)$	eV	$50 \pm 10\%$
V_{p}	m^3	$1.6 \pm 20\%$

3.C Details of controller design

In this appendix, the design of a feedback controller using H_∞ synthesis tools is elaborated. This state feedback controller stabilizes the closed-loop and achieves robust performance against the modeled uncertainties.

3.C.1 Uncertain plant model

The continuous-time model (3.18) is linearized around a nominal stationary operating point x_0, u_0 and written as

$$\frac{d\tilde{x}}{dt} = A\tilde{x} + B\tilde{u} = \left.\frac{dg}{dx}\right|_{x_0,u_0} \tilde{x} + \left.\frac{dg}{du}\right|_{x_0,u_0} \tilde{u} \tag{3.35}$$

where $\tilde{x} = x - x_0$ and $\tilde{u} = u - u_0$. Next, a subset of the parameters in p and coefficients (see Appendix 3.A) is considered uncertain with nominal values $\overline{p}, \overline{c}$ and uncertainty sets $\Delta p, \Delta c$. The system matrix and input matrix of the uncertain plant model are $A_{\mathrm{unc}} = A|_{p,c}$ and $B_{\mathrm{unc}} = B|_c$ where p and c are samples from the uncertainty sets $\overline{p} + \Delta p$ and $\overline{c} + \Delta c$. The nominal values and uncertainties considered in this work are shown in Table 3.1. These correspond to uncertainty in the steady-state gain and time scales of (3.35).

The controlled variable is defined as a linear combination of the plant states and is defined as $x_{\mathrm{c}} = Z\tilde{x}$. The transfer function of the uncertain plant model is denoted by $G(s)$ and is given by

$$G(s) = Z\left(sI - A_{\mathrm{unc}}\right)^{-1} B_{\mathrm{unc}} \tag{3.36}$$

The frequency response of G for various values in the uncertainty set is shown in Figure 3.13. Recall that the control error is defined as $e = x_{\mathrm{ref}} - x_{\mathrm{c}}$ where x_{ref} denotes the reference. We define P to be the open-loop tracking interconnection

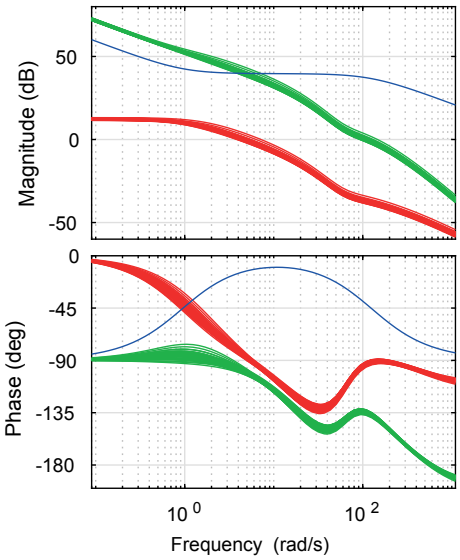

Figure 3.13 – Bode diagram of various frequency responses of the uncertain plant $G(j\omega)$ (red), controller $K(j\omega)$ (blue) and open-loop $L(j\omega)$ (green). Note that the low-frequent response of the plant G has a stable pole around 1rad/s. The pole location and steady-state response vary due to the uncertain coefficients and parameters.

of the plant G. This interconnection is given by

$$\begin{bmatrix} e \\ \tilde{u} \\ x_c \\ e \end{bmatrix} = P \begin{bmatrix} x_{\text{ref}} \\ \tilde{u} \end{bmatrix} = \begin{bmatrix} I & -G \\ 0 & I \\ 0 & G \\ I & -G \end{bmatrix} \begin{bmatrix} x_{\text{ref}} \\ \tilde{u} \end{bmatrix} \tag{3.37}$$

3.C.2 Weighting filters

In order to impose reference tracking below the required bandwidth ω_b, zero steady-state error and disturbance rejection, the tracking interconnection P with weighting filters. The augmented tracking interconnection is given by

$$P_W = \begin{bmatrix} W_S & & & \\ & W_R & & \\ & & W_T & \\ & & & I \end{bmatrix} P \tag{3.38}$$

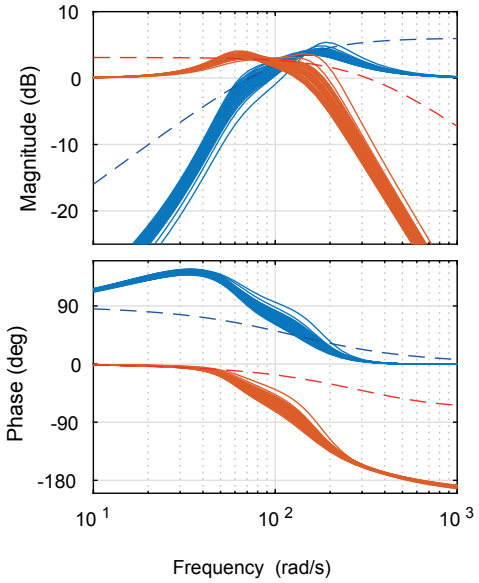

Figure 3.14 – Bode diagram of control sensitivity $S(j\omega)$ (blue) (and inverse shaping function $W_S^{-1}(j\omega)$ in dashed blue), complementary control sensitivity $T(j\omega)$ (red) (and inverse shaping function $W_T^{-1}(j\omega)$ in dashed red). The sensitivity crosses the 0dB between 65rad/s and 100rad/s.

where $W_S(s)$, $W_R(s)$ and $W_T(s)$ are the weighting filters. Here, $W_S(s)$ imposes zero steady-state error, penalizes tracking error below the bandwidth ω_b and penalizes the sensitivity above 6dB, $W_T(s)$ penalizes closed-loop gain above 3dB and $W_R(s)$ penalizes control action over all frequencies. The inverse of the filters $W_S(s)$ and $W_T(s)$ are shown in Figure 3.14.

3.C.3 Controller synthesis by H_∞ norm minimization

A controller of the form

$$K(s) = \frac{(K_\mathrm{P} s + K_\mathrm{I})\,\omega_\mathrm{rolloff}}{s\,(s + \omega_\mathrm{rolloff})} \tag{3.39}$$

is chosen. The gains K_P and K_I are to be determined by the synthesis, while ω_rolloff is fixed at 40πrad/s. The closed-loop interconnection F is defined as $F = P_W \star K$ where $\star$ denotes the Redheffer star product. The free gains are then tuned by minimizing the H_∞-norm of F using the MATLAB function `hinfstruct` from the Robust Control toolbox [The Mathworks Inc., a]. The resulting controller K stabilizes the closed-loop interconnection and achieves robust performance against the uncertainties. In Figure 3.13, the frequency response of the controller

K and open-loop transfer $L = GK$ are plotted. In Figure 3.14, the sensitivity S and complementary sensitivity T are plotted. These are defined as $S = \frac{I}{I-L}$ and $T = \frac{L}{I-L}$. These bode plots show that the sensitivity and complementary sensitivity have the desired shape, since the magnitude response is smaller than those of their respective inverse weighting filters.

Chapter 4

Real-time plasma state monitoring and supervisory control on TCV

Abstract In ITER and DEMO, various control objectives related to plasma control must be simultaneously achieved by the plasma control system (PCS), in both normal operation as well as off-normal conditions. The PCS must act on off-normal events and deviations from the target scenario, since certain sequences (chains) of events can precede disruptions. It is important that these decisions are made while maintaining a coherent prioritization between the real-time control tasks to ensure high-performance operation.

In this paper, a generic architecture for task-based integrated plasma control is proposed. The architecture is characterized by the separation of state estimation, event detection, decisions and task execution among different algorithms, with standardized signal interfaces. Central to the architecture are a plasma state monitor and supervisory controller. In the plasma state monitor, discrete events in the continuous-valued plasma state are modeled using finite state machines. This provides a high-level representation of the plasma state. The supervisory controller coordinates the execution of multiple plasma control tasks by assigning task priorities, based on the finite states of the plasma and the pulse schedule.

These algorithms were implemented on the TCV digital control system and integrated with actuator resource management and existing state estimation algorithms and controllers. The plasma state monitor on TCV can track a multi-

This chapter is accepted for publication in Nuclear Fusion. The authors of the manuscript are T.C. Blanken, F. Felici, C. Galperti, N.M.T. Vu, M. Kong, O. Sauter, M.R. de Baar, the EUROfusion MST1 team and the TCV team.

tude of plasma events, related to plasma current, rotating and locked neoclassical tearing modes, and position displacements.

In TCV experiments on simultaneous control of plasma pressure, safety factor profile and NTMs using electron cyclotron heating (ECH) and current drive (ECCD), the supervisory controller assigns priorities to the relevant control tasks. The tasks are then executed by feedback controllers and actuator allocation management. This work forms a significant step forward in the ongoing integration of control capabilities in experiments on TCV, in support of tokamak reactor operation.

4.1 Introduction

In long-pulse scenarios in tokamak reactors, multiple plasma quantities such as current, shape, kinetic profiles, impurities and various magnetohydrodynamic (MHD) activity need to be controlled simultaneously in real time [Humphreys et al., 2015; Pironti and Walker, 2005; Snipes et al., 2014]. The plasma conditions must stay at the target references despite unknown or unpredictable disturbances such as MHD activity or actuator/diagnostic failure. It is envisioned that multiple feedback controllers will operate concurrently, and that each will control a subset of the relevant plasma quantities [Snipes et al., 2017; Treutterer et al., 2014b].

What are the requirements for the plasma control system (PCS) for a tokamak reactor? First, the PCS should execute the pulse schedule during plasma operations. Second, the PCS should decide which plasma quantities must be controlled subject to not only the pulse schedule but also to the state of the plasma and the machine. Third, unforeseen events (such as MHD activity, exceeding operational limits, and deviations from the target scenario, see [De Vries et al., 2011; Humphreys et al., 2015]) must be suppressed, controlled or mitigated by the PCS [Maraschek et al., 2018; Raupp et al., 2017; Snipes et al., 2017] to maintain plasma performance and stability. If suppression of instabilities or rejection of disturbances is not possible, the PCS must decide on future action, e.g. pursue a lower performance target or initiate an emergency ramp-down.

By definition, a reactor will have limited actuation resources, and it is therefore foreseen that actuators will be shared between the controllers that execute the various control tasks [Humphreys et al., 2015]. For example, NBI, ICRH and EC systems provide heating and current drive (H&CD), allowing control of the plasma pressure, the safety factor profile and the MHD modes [Henderson et al., 2015; Snipes et al., 2012]. Depending on the plasma state and actuator availability, not all control objectives may be achieved simultaneously, so the PCS must prioritize the control tasks and allocate actuation resources to the tasks [Humphreys et al., 2015].

In present day tokamak control systems, the integration of various plasma controllers and plasma supervision for the internal plasma quantities is expand-

ing. Although advanced control of e.g. pressure and shape is done routinely, the real-time decision-making is uncommon.

Often, individual control algorithms are developed and used for specific experiments, and are not operated concurrently with other controllers. Significant research has recently been conducted towards real-time control of multiple quantities simultaneously; for instance at TCV [Kim et al., 2016; Maljaars et al., 2017; Mavkov et al., 2018; Vu et al., 2016], DIII-D [Lauret et al., 2017; Wehner et al., 2016, 2017] and in simulations for ITER [Barton et al., 2015]. While these represent important steps towards integrated plasma control, they lack dedicated task coordination logic for actuator sharing management among multiple (different) controllers. Furthermore, significant work has been done at ASDEX-Upgrade in switching actuation resources between multiple controllers for simultaneous pressure and NTM control [Rapson et al., 2016]. While this marks a major step in integrated control, the resource switching is hardcoded for the intended experiment, based on a single trigger. Accommodating additional functionality in a specific implementation often requires substantial rewriting of existing code. Moreover, in present-day practice, signals of (combinations of) individual diagnostics are used to trigger specific control/event handling algorithms. While recent research on real-time off-normal event handling on DIII-D and KSTAR [Eidietis et al., 2018] provides the required real-time decision-making, this linked individual diagnostics to specific event handling algorithms and actuators. The links between diagnostics and event handling are done in an ad-hoc fashion, and a modification of the event triggering logic requires manual adjustments of the control code. Also, algorithms are difficult to port from one tokamak to another since they depend on specific diagnostics and actuators.

Instead, it is desirable to have a generic architecture separating

- the estimation of the full generic plasma state from tokamak-specific diagnostics,
- the detection of events in the plasma (or tokamak subsystems) based on the generic state description rather than specific diagnostic signals, and
- the decision logic on how to respond to these events,

as is also elaborated in [Humphreys et al., 2015]. This allows for programming arbitrary decisions based on combinations of multiple events.

The PCS of future tokamaks is responsible for high-level discharge supervision, meaning segment scheduling, managing control objectives, but also off-normal event handling. It is important to note that these functionalities must be performed in real-time for long pulse scenarios, as opposed to inter-discharge decision-making common in today's tokamak experiments. The requirements for the supervisory control come from the quantities that should either be controlled, or the quantities that should be monitored since the PCS should respond to them. Also, the set of requirements is different for a small and flexible experimental tokamak like TCV (operated in many different scenarios with different

experimental needs on a day), than for a long-pulse experiments like ITER (performing a few scenarios for exploration) or a reactor like DEMO (performing one scenario). Because of the inherent physics coupling between many plasma quantities, information of the plasma state is needed for real-time control decisions. It is desirable to centralize all *high-level* plasma decisions so that decisions may be taken by a single algorithm that has the maximally available information about the plasma and the relevant tokamak subsystems [Raupp et al., 2017; Treutterer et al., 2017]. Here, *high-level* relates to the integrated operation and coordination across all plasma control objectives and algorithms, as opposed to the *low-level* operation of individual control algorithms and hardware control.

The aim of this paper is twofold. First, a conceptual framework for integrated control of tokamak plasmas employing full plasma state monitoring and supervisory control is presented. Second, the results of plasma state monitor and the supervisory controller at TCV applied to experimental simultaneous MHD and kinetic profile control with real-time decisions based on the NTM state are reported.

The conceptual framework has an architecture that is characterized by a strict separation between:

1. a suite of reconstruction algorithms for the plasma and actuator states,
2. a finite-state machine representation for the monitoring of these states,
3. a centralized supervisory controller for enabling and prioritizing control tasks, and
4. the algorithms responsible for the execution of the control tasks, being (feedback) controllers and actuation resource management.

The ordering in the above list is intentional: each component sequentially feeds information into the next. In Figure 4.1, we show a diagram of several high-level software components in a PCS, corresponding to the above list.

One aim of the real-time state monitoring is to automate the offline analysis of plasma events, such as carried out in [De Vries et al., 2011; Gerhardt et al., 2013], for the purpose of plasma control. The result of high-level decisions executed by the supervisory controller consists of the real-time enabling prioritized control tasks, subject to the plasma state and available resources. Each control task represents a specific objective that a (feedback) control algorithm should accomplish in the plasma (see [Vu et al., 2018]). Yet, the control task does not contain explicit directives on how a controller must execute this task, such as which actuators and control laws to use. The control task is therefore per definition *tokamak-agnostic*.

The development and application of the architecture at TCV is a collaborative effort. This paper deals primarily with the plasma state monitoring and supervisory controller, as the (compatible) actuator manager and interfaces to feedback controllers and actuators are reported in [Vu et al., 2018]. One of the difficulties encountered during development, implementation and integration of

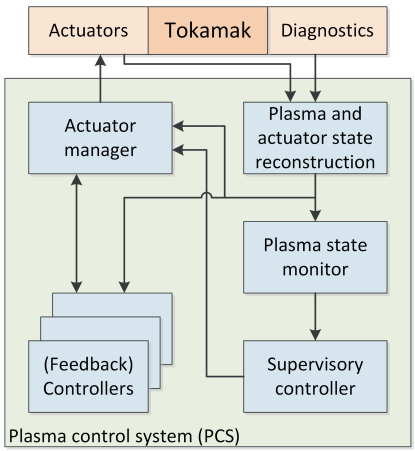

Figure 4.1 – Block diagram of (a selection of) envisioned high-level PCS functionalities. Besides standard feedback control loops, plasma state monitoring and supervision provide high-level decisions regarding multiple control tasks. Moreover, an actuator management algorithm dynamically assigns actuators to controllers, see [Vu et al., 2018]. These components for pulse supervision and control were also defined in [Humphreys et al., 2015; Treutterer et al., 2014b]. However, in this paper and in [Vu et al., 2018], signal interfaces for integrated control are defined explicitly.

these complex integrated control algorithms on the TCV control system [Anand et al., 2017] is that existing input-output signal interfaces were different among various controllers. This proved to be impractical and confusing, particularly while asserting genericity and anticipating future expansions of the control capabilities. Therefore, all signal interfaces between the finite-state machine models, the supervisory controller, the actuator management algorithm and the control algorithms are standardized [Vu et al., 2018]. This provides ease of development and scalability to additional actuators and control algorithms. The standardization defines the signal dimensions, as well as their meaning in terms of either *tokamak-agnostic* quantities (e.g. kinetic profiles, ECH deposited power and deposition location) or *tokamak-specific* quantities (e.g. ECE data, power supply voltages and mirror angles of EC launchers).

The remainder of this paper is structured as follows: in Section 4.2, the generic software architecture containing the state estimation, state monitor and supervisory control algorithms is discussed. The generic design of the state monitor and the supervisory controller are described in Section 4.3 and Section 4.4, respectively. In Section 4.5, the implementation of the state monitor and supervisory controller on TCV's control system, as well as results of finite state monitoring on TCV discharges are presented. Experimental results with the

application of the supervisory control in a TCV discharge are presented. The results of the latter sections are discussed in Section 4.6. Finally, conclusions and an outlook are given in Section 4.7.

4.2 Generic plasma control system software architecture

In this section, the proposed architecture for integrated plasma control on a PCS is presented and motivated. This architecture facilitates concurrent execution of multiple control tasks using multiple actuators. It is characterized by a strict separation of components based on their functionality as well as their degree of independence to the specifics of the tokamak diagnostics and actuators. First, the concept of control tasks is explained and their usage for handling multiple control tasks is motivated. Second, the proposed control system architecture is discussed. In particular, the functionality and input-output signals of the software components that are described in this paper are highlighted. Last, the design choice of using *tokamak-agnostic* signal interfaces between the algorithms is motivated.

4.2.1 Task-based supervisory control

In order to facilitate real-time prioritization of multiple control objectives, an abstraction of the representation of these objectives is proposed, called control tasks. As explained in more detail in [Vu et al., 2018], a control task is defined as a specific objective that should be accomplished in the plasma. Examples of various control tasks are confinement mode control, NTM suppression, NTM preemption, sawtooth pacing, safety factor profile control and impurity removal control. The supervisory control algorithm enables and prioritizes each control task, based on the discharge time, pulse schedule, the state of the plasma as well as the state of the actuators. These priorities represent the (relative) importance of the tasks. Many other research has addressed these tasks, yet with ad-hoc implementations for the specific task and binary prioritizations of tasks, see e.g. [Rapson et al., 2016].

The design choice of abstracting the task execution to facilitate the coordination of integrated plasma control and exception handling has several advantages compared to existing solutions. These are:

- the supervisory decision logic on task priorities may be designed and interpreted more easily, since these decisions do not involve the specifics of the task execution by the responsible controller,
- the tasks are generic and similar among different tokamaks, such that the generic supervisory controller may be used for different devices,

- different feedback controllers may be used interchangeably for a given control task, without changing the supervisory logic,
- since functionalities (e.g. state estimation, task decision logic and task execution) are disentangled and reside in different algorithms with generalized input-output interfaces, the algorithms may be developed separately. This enhances interchangeability and portability of algorithms.

Ultimately, these priorities are taken into account by the actuator management algorithm, which assigns the scarce actuators to the tasks. These latter tasks are executed by controller algorithms given the assigned resources. In the actuator manager, the priorities are used as input to an optimization problem, together with factors such as actuator availability, (possibly conflicting) requirements, and actuation requests from controllers, to assign actuation resources to each task. Examples of such optimization algorithms are presented in [Maljaars and Felici, 2017; Rapson et al., 2015; Vu et al., 2018].

Still, while the supervisory controller determines the priority of tasks, it does not produce explicit commands and directives on how the controllers must accomplish this task, e.g. which specific actuators and control laws to use. This abstraction of the objectives decouples the design of the supervisory control algorithm from the specifics of the task execution, which is handled by the controllers. When enabled, each control task will be executed by one (feedback) controller algorithm.

4.2.2 Control system software architecture

Different architectures for real-time supervisory control and actuator allocation are possible [Maljaars and Felici, 2017]. Although distributed supervisory control among the controllers is more easy to design for local optimality, they may take decisions that are globally contradictory or counterproductive. For instance, for the suppression of NTMs using ECH it may be needed to temporarily reduce the plasma kinetic pressure, overriding the normal reference for a pressure controller. In contrast, all decision-making can be merged in a single centralized supervisory controller, avoiding contradictory actions by consistent globally optimal decision-making. In this work, the latter centralized supervisor is considered.

In Figure 4.2, a block diagram of the software components and signals is presented, which includes three layers. These layers, the software components, their functions and their input and output signals are introduced next.

Tokamak-agnostic signal definitions between algorithms

The components seen in Figure 4.2 are grouped among three distinct layers, namely a *tokamak-specific layer*, an *interface layer* and a *tokamak-agnostic layer*. Algorithms in the *interface layer* form the boundary between the signals

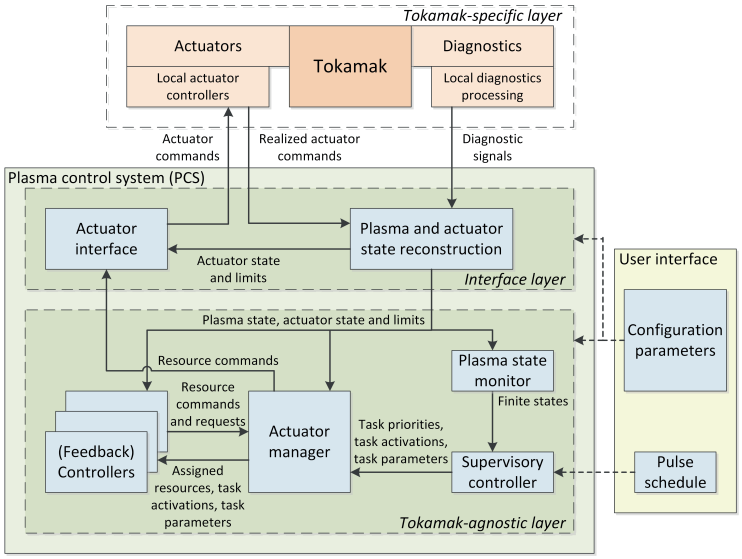

Figure 4.2 – Block diagram of the generic architecture of a plasma control system. This architecture facilitates event detection, integrated control, exception handling and actuator sharing. All signals in the *tokamak-agnostic layer* are defined in terms of generic quantities, while algorithms in the *interface layer* form the boundary between the *tokamak-agnostic* and *tokamak-specific* signal quantities.

from device-specific hardware (e.g. the diagnostics and actuators in the *tokamak-specific layer*) and signals in the *tokamak-agnostic layer*. The algorithms in the *tokamak-agnostic layer* are characterized by an input-output interface where signals are defined in terms of plasma states (e.g. kinetic profiles, equilibrium and MHD states) and actuation resource signals (e.g. injected heating power and deposition location in terms of normalized radius), rather than device-specific diagnostics signals (e.g. ECE data, line-integrated density) and device-specific actuator signals (e.g. power supply voltages, EC mirror angles). In [Vu et al., 2018], the architecture and the design choices for these software layers are further motivated.

Plasma and actuator state reconstruction

As introduced in Section 4.1, a single unified representation of the physical state of the plasma and actuators is chosen in order for a single centralized agent to make decisions about all control tasks, as well as providing the plasma state to all controller algorithms for the purpose of feedback control.

In this paper, the state of a system is defined as the (smallest) set of (in-

ternal) physical quantities that describe the dynamical evolution in time of the system sufficiently for the purpose of control. The choice of what quantities are represented in the state depend on the level of detail required for the application. For typical control tasks on tokamaks, the state of the plasma and tokamak is roughly represented by the plasma equilibrium, the currents in the conducting structures, all kinetic and magnetic profiles (including fast ions or runaway electrons), the presence, type and amplitude of MHD modes, the availability of actuator systems, and angles of movable mirrors and waveguide switches. These are chosen because they are the typical quantities that a control system may attempt to manipulate or may need to react to, and are generic for all tokamaks. The representation of this state in the control system software is a parametrization of this physical state.

Note that it may or may not be possible to reconstruct the state of the plasma based on diagnostic measurements, depending on the quality and quantity of diagnostic signals, as well as the modeling understanding of the underlying physics that determine the state evolution. This is discussed in more detail in [Felici et al., 2011, 2016].

All algorithms that estimate the continuous real-valued state of the plasma and actuators based on the specific diagnostic and actuator signals are grouped in the plasma and actuator state reconstruction. The state reconstruction algorithms are typically equilibrium reconstruction (e.g. EFIT [Ferron et al., 1998] and RT-LIUQE [Moret et al., 2015]), MHD analysis (e.g. [van den Brand et al., 2016; Galperti et al., 2014]), profile estimators (e.g. the RAPTOR-observer [Felici et al., 2014a, 2016]), ray-tracing codes (e.g. RT-TORBEAM [Poli et al., 2018]), and more. The resulting state contains the estimates of kinetic profiles, equilibrium, MHD states, absorbed auxiliary heating power, actuator state, among others. This is the common state fed to all other algorithms.

Depending on the requirements, these state estimates should probably be available at different sample rates. For example for the purpose of control and plasma monitoring, the vertical position must be computed at a higher rate than plasma equilibria. The proposed framework is not restricted to a single sample rate.

Plasma state monitor

Since the decisions about control tasks are taken in the supervisory controller based on discrete assessments of the condition of the plasma, a translation of the continuous representation of the state (e.g. values of physical quantities) to a discrete representation is made. In the plasma state monitor, this discrete state representation is formed using finite state machines (see [Cassandras and Lafortune, 2008]) representing the state of the plasma and the actuators at every time step during a plasma discharge. The finite state machines represent all the states of the plasma that the PCS should respond to or control. In Section 4.3,

the plasma state monitor is discussed in more detail.

Supervisory controller

The supervisory controller is responsible for all real-time decision-making regarding the coordination of all control tasks, as is also mentioned in [Raupp et al., 2017; Treutterer et al., 2014b, 2017].

The proposed supervisory controller has explicitly defined inputs and output signal interfaces to other algorithms in the PCS. It produces the task priorities, the task activation as well as quantities specific to eask task (e.g. references, parameter settings), based on the discrete state of the plasma and the pulse schedule. These task priorities form the basis on which actuators are allocated in real time to the control tasks and their executing control algorithms. In Section 4.4, the proposed supervisory controller is discussed more in detail.

Actuator manager, actuator interface and controller algorithms

An actuator management algorithm (e.g. [Maljaars and Felici, 2017; Rapson et al., 2015; Vu et al., 2018]) assigns the available actuation resources (in terms of heating power, current drive, fuelling) to the control tasks, based on the task priority, actuator availability and requests from controller algorithms. A set of (feedback) controllers is responsible for the execution of the tasks, using the assigned actuation resources. The focus of this work is on the plasma state estimation and monitoring, and supervisory control. The design of a compatible actuator manager and the interface to controller algorithms and actuator hardware can be found in [Vu et al., 2018].

4.3 Design of a generic plasma state monitor

In this section, the architecture and design of a plasma state monitor, containing finite-state models, are presented. These models are *tokamak-agnostic*, meaning that they can represent the state of any tokamak plasma. Plasma states and events (such as those in [De Vries et al., 2011; Gerhardt et al., 2013]) are formalized using the concept of finite state machines (FSM) [Cassandras and Lafortune, 2008].

The list of FSMs needed to represent a tokamak plasma for the purpose of real-time control and event handling should be dictated by requirements. The required FSMs are determined by the quantities that need to be controlled or the events that should be monitored since the PCS may need to respond to them (e.g. limit violations, deviations from the target scenario, hardware faults). This list poses requirements on which plasma quantities should be estimated in real time and their reconstruction accuracy. The required quantities will be the confinement mode, detachment state, proximity of quantities (e.g. current,

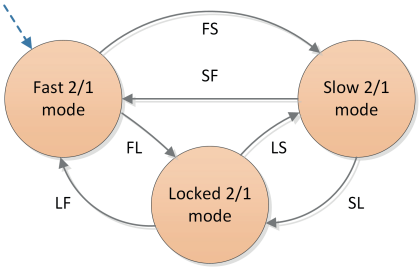

Figure 4.3 – The finite state machine representation of the 2/1 mode frequency. The transitions are triggered on conditional tests, specified in Table 4.1. These state transitions are triggered on the estimated 2/1 mode amplitude and frequency, as well as the estimated $n = 1$ locked mode amplitude. The dashed arrow indicates the initially active state. An non-exhaustive list of required finite state machines, their states and input signals are given in the respective columns of Table 4.2.

Table 4.1 – The conditions for the transitions of the finite state machine in Figure 4.3. These transitions use the plasma state signals $f_{2/1\text{mode}}$, $A_{2/1\text{mode}}$ and $A_{n=1\text{LM}}$, see Table 4.2. Note that small numbers ϵ_A and ϵ_f are added to the signal thresholds on reciprocal transitions, e.g. FS and SF. The resulting hysteresis prevents fast switching between states due to small signal variations. Furthermore, the threshold values are chosen such that $f^{\text{thresh,FS}}_{2/1\text{mode}} > f^{\text{thresh,SL}}_{2/1\text{mode}} + \epsilon_\text{f}$. Similar conditions are formulated for all FSMs in Table 4.2.

Transition	Conditional test
FS	$f_{2/1\text{mode}} < f^{\text{thresh,FS}}_{2/1\text{mode}}$ AND $A_{2/1\text{mode}} > A^{\text{thresh,FS}}_{2/1\text{mode}} + \epsilon_\text{A}$
SF	$f_{2/1\text{mode}} > f^{\text{thresh,FS}}_{2/1\text{mode}} + \epsilon_\text{f}$ OR $A_{2/1\text{mode}} < A^{\text{thresh,FS}}_{2/1\text{mode}}$
FL, SL	$f_{2/1\text{mode}} < f^{\text{thresh,SL}}_{2/1\text{mode}}$ OR $A_{n=1\text{LM}} > A^{\text{thresh}}_{n=1\text{LM}} + \epsilon_\text{A}$
LF	$f_{2/1\text{mode}} > f^{\text{thresh,FS}}_{2/1\text{mode}} + \epsilon_\text{f}$ AND $A_{\text{n=1LM}} < A^{\text{thresh}}_{\text{n=1LM}}$
LS	$f_{2/1\text{mode}} > f^{\text{thresh,SL}}_{2/1\text{mode}} + \epsilon_\text{f}$ AND $f_{2/1\text{mode}} < f^{\text{thresh,FS}}_{2/1\text{mode}} + \epsilon_\text{f}$ AND $A_{n=1\text{LM}} < A^{\text{thresh}}_{n=1\text{LM}}$

q_{95}, internal inductance, shape parameters, pressure, density, rotation, NTM amplitude and frequency, locked mode amplitude and phase) to their respective physics and operational limits, deviations of the controlled quantities from their references/targets, among others.

In general, each plasma state or set of physically related states that the PCS should respond to is modeled by a single FSM. Discrete quantities such as confinement mode (ohmic, L-mode, ELMy H-mode, quiescent H-mode) and number of X-points may be directly represented by FSMs. In line with modular modeling practice [Baeten et al., 2016; Cassandras and Lafortune, 2008],

each FSM should represent one quantity (or component) and be as small as possible (atomic), avoiding unnecessary large FSMs which could be divided in sub-FSMs. This prevents redundancy among the FSMs. The combination (or synchronous composition, see [Cassandras and Lafortune, 2008]) of all individual FSMs represents the full system.

As an example, the finite state machine for the rotational frequency of a 2/1 mode, which may be indicative of the mode locking, is depicted in Figure 4.3 and is further detailed in Section 4.3.2. Its transition conditions are listed in Table 4.1. The meaning of the finite states depends on the requirements for (supervisory) control. For example, the states slow can represent a mode that is predicted to lock within a set amount of time, while the state fast can represent a mode that does not pose immediate threat of locking. Although the threshold values of the transition conditions are specific to the application on a tokamak, they represent physics quantities rather than device-specific measured quantities.

A number of FSMs representing the plasma may be considered for the purpose of integrated plasma control. In Table 4.2, an overview of finite state machines F, their states S and their input signals u is given. This table provides an initial set of plasma states which should be used for decision-making in integrated plasma control. Yet, the table is in no way complete or exhaustive. FSMs for additional plasma quantities may be added, for example for (low) plasma rotation, (excessive) tile temperature at strike point locations, MHD mode classification ((neoclassical) tearing mode, resistive wall mode, external kink, etc) and normalized beta limit proximity and violation. In Figure 4.4, the input signals u and output signals Y of the plasma state monitor, which contains the finite state machines, are depicted. These FSMs are briefly introduced next.

4.3.1 Plasma current segment

A simple set of discharge segment labels are considered in this work, namely the ramp-up, flat-top, ramp-down, as well as the absence of plasma. The observation of these discharge phases may be important for enabling control tasks. For instance, fusion power production may only be initiated in a reactor once the plasma is observed to be in flat-top and the current is constant.

In this paper, it is chosen to derive the discharge segment from the measured plasma current and its time derivative. Thresholds tests on the sign and absolute value of the time derivative of the plasma current cue the transitions between the ramp-up, flat-top or ramp-down states. The plasma is considered absent when the absolute value of the measured plasma current is below a given threshold.

4.3.2 Rotating modes

A number of states of rotating modes are considered, being the magnetic perturbation amplitude, frequency and rotational acceleration of the magnetic per-

Table 4.2 – Non-exhaustive list of finite state machines F that should be considered for representing a tokamak plasma for the purpose of control and event handling, with signals u used for the state transitions. Note that duplicates for different m/n numbers of MHD modes are listed.

Finite state machine F name	States S	Used input signals from u
Plasma current segment	• no plasma, • ramp-up, • flat-top, • ramp-down	measured plasma current I_P and time derivative $\frac{d}{dt} I_\mathrm{P}$
Mode amplitude m/n={2/1, 3/1, 3/2}	• nomode, • small, • large	mode amplitude $A_{(m/n)\mathrm{NTM}}$
Mode frequency m/n={2/1, 3/1, 3/2}	• locked, • slow, • fast	mode frequency $f_{(m/n)\mathrm{NTM}}$, mode amplitude $A_{(m/n)\mathrm{NTM}}$ and locked mode amplitude $A_{(n)\mathrm{LM}}$
Mode acceleration m/n={2/1, 3/1, 3/2}	• locking, • stationary, • unlocking	NTM acceleration $\frac{d}{dt} f_{(m/n)\mathrm{NTM}}$ and locked mode amplitude $A_{(n)\mathrm{LM}}$
Locked mode amplitude $n = \{1, 2, 3\}$	• noLM, • LM	locked mode amplitude $A_{(n)\mathrm{LM}}$
Position error (slow/static): vertical and radial	• negative displ., • no displ., • positive displ.	vertical and radial position error $Z_{\mathrm{A,e}}$, $R_{\mathrm{A,e}}$
Position oscillations: vertical and radial	• no oscillations, • oscillatory	vertical and radial position oscillation amplitude $A_{\mathrm{Z,osc}}$, $A_{\mathrm{R,osc}}$
Vertical displacement event	• no VDE, • VDE	vertical displacement indicator $Z_{\mathrm{A,e}} \frac{d}{dt} Z_{\mathrm{A,e}}$
Greenwald density limit ratio	• below limit, • close to limit, • above limit	Greenwald fraction f_GW
Electron density control error	• below control specification, • close to zero, • above control specification	electron density error $n_{\mathrm{e,ref}} - n_\mathrm{e}$
Confinement mode	• ohmic, • L-mode, • I-mode, • ELMy H-mode • quiescent H-mode	auxiliary heating power, H-mode detection, ELM frequency, electron density profile $n_\mathrm{e}(\rho)$, electron temperature profile $T_\mathrm{e}(\rho)$
Magnetic configuration mode	• limited, • lower/upper single null, • double null	reconstructed equilibrium
Detachment mode	• no detachment, • marginally detached, • detached	detachment detection, detachment front location
Sawtooth frequency	• no ST, • slow ST, • fast ST	sawtooth frequency f_ST
Current density profile class	• inductive, • hybrid, • reverse-shear	normalized magnetic shear $s = \frac{\rho}{q} \frac{\partial q}{\partial \rho}$
Internal transport barrier location	• no ITB, • ITB collocated with q_min location, • ITB non-collocated with q_min loc.	electron temperature profile gradient $\frac{\partial T_\mathrm{e}}{\partial \rho}$, current density profile $q(\rho)$
Thermal radiation	• close to expected radiation, • excessive radiation, • core radiative collapse	radiated power fraction, electron temperature gradient, tungsten density profile

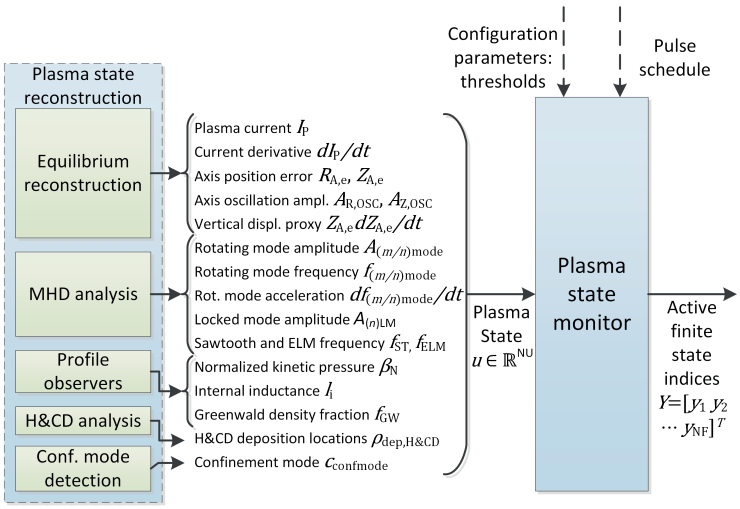

Figure 4.4 – Block diagram of the generic plasma state monitor. Only the signals that can be estimated in real time on TCV at present are listed, which is a subset of those listed in Table 4.2. See Section 4.5 for the set of signals and FSMs that are implemented on TCV.

turbation. In this paper, the m/n=2/1, 3/1 and 3/2 modes are considered, with separate finite state machines for each mode and each of the aforementioned quantities, see Table 4.2. The mode presence, i.e. an amplitude labeled as 'small' or 'large' may be interpreted as either the 'MHD' or 'NTM' events from [De Vries et al., 2011], can lead to a disruption. The mode acceleration, i.e. the time derivative of its frequency, is considered since it may be indicative (in combination with the frequency) of mode locking and unlocking. In Figure 4.3, the finite state machine for the rotational frequency of a 2/1 mode is shown. Note that the 'locked' state in the mode frequency FSMs corresponds to the 'ML' label in [De Vries et al., 2011]. The FSMs for the modes require the reconstructed continuous-valued magnetic perturbation amplitude, frequency and acceleration of each of the m/n modes as input signals.

In order to avoid redundancy among the FSMs, only the mode amplitude FSM indicates the mode presence. Recall that the combination (or synchronous product [Cassandras and Lafortune, 2008]) of the finite state machines characterizes the full system, thereby eliminating the need for redundancy among atomic FSMs.

4.3.3 Locked modes

In this work, the presence of toroidally resolved locked modes is considered, specifically the $n = \{1, 2, 3\}$ modes. A mode lock is often a precursor to a disruption [De Vries et al., 2011; Sweeney et al., 2017], and its presence may require an emergency rampdown in a reactor.Thresholds on the magnetic perturbation amplitude determine the transitions between the states listed in Table 4.2. The presence of any locked mode corresponds to the 'ML' label in [De Vries et al., 2011].

4.3.4 Plasma position displacements and oscillations

Concerning the plasma position, different states and events may be considered, such as position displacements with respect to their references, vertical displacement events in disruptions, and plasma position oscillations. The latter may occur in TCV due to challenges in vertical stabilization control. In a reactor, problems with plasma position control may require a modification of the internal inductance or elongation to avoid a disruption. A vertical displacement event corresponds to the 'VDE' label, while the vertical position displacements and oscillations are related to the 'VSC' (vertical stability control problem) label in [De Vries et al., 2011].

Threshold checks on the reconstructed position errors w.r.t. the references, $Z_{\mathrm{err}} = Z_{\mathrm{reconstr}} - Z_{\mathrm{ref}}$ and $R_{\mathrm{err}} = R_{\mathrm{reconstr}} - R_{\mathrm{ref}}$, determine the transitions between the position displacement states listed in Table 4.2. Threshold checks on the amplitude of observed oscillations determine the transition between the oscillation states. Moreover, threshold checks on the multiplication $Z_{\mathrm{err}} \frac{d}{dt} Z_{\mathrm{err}}$ indicates unstable vertical displacement events seen in disruption, as is also done in [Gerhardt et al., 2013].

4.3.5 Plasma kinetic quantity deviations and limits

The proximity to and excursions of known operational and physics limits related to kinetic quantities may be used to trigger recovery actions. These limits may include the Greenwald density limit, limits on q_{95}, and normalized kinetic pressure limits. Also, deviations of controlled kinetic quantities w.r.t. their references indicate control problems or indicate that a controller is outside its designed operational space, and may be used to trigger recovery actions [Humphreys et al., 2015]. Threshold checks on reconstructed (quantities derived from) kinetic profiles may determine the transitions between operational states.

Table 4.3 – Abstract examples of supervisory control decision logic. The task activation conditions in the second column are conditional tests on the discharge time t and the active finite states Y, which were introduced in Section 4.3 and listed in Table 4.2. If a condition holds, the priority is assigned to the corresponding task. Different exclusive conditions may result in different priorities for a task, as seen here for Task 1. Moreover, in the case that a controller can execute one out of several tasks, exclusive conditions among these activation conditions ensure that only one task becomes active at a time. This is shown here for Task 2 and 3.

Task	Activation condition	Priority
Task 1	$y_1 ==$ state2 OR $y_2 ==$ state1	$p_{\text{Task1}} = c_1$
	$y_1 ==$ state1 AND $y_2 \neq$ state1 AND $t_{1,1} < t < t_{1,2}$	$p_{\text{Task1}} = c_2$
Task 2	$y_2 ==$ state2 AND $t_{2,1} < t < t_{2,2}$	$p_{\text{Task2}} = c_3$
Task 3	$y_2 \neq$ state2 AND $t_{3,1} < t < t_{3,2}$	$p_{\text{Task3}} = c_4$

4.4 Design of a generic supervisory controller

In this section, the supervisory control algorithm, as mentioned in Section 4.2, is presented. The function of the supervisory controller is to coordinate the execution of various control objectives in the plasma. The supervisory controller prioritizes the various control tasks and activates the low-level controllers responsible for executing the tasks. The priorities are taken into account by the actuator management system; they are an input to the merit function that determines optimal allocations of actuation resources to tasks. This output of the supervisory controller depends on a combination of a preprogrammed response in time, and on states observed in the plasma. For example, the transition to high confinement mode will be programmed by a feedforward waveform for auxiliary heating power; while the observation of an unexpected backtransition should prompt the PCS to allocate additional resources for central heating power or adapt the pressure reference.

4.4.1 Task-based coordination of controller algorithms

Each control task can be executed by one or more low-level controllers. For example, the task for plasma kinetic pressure control can be executed by either pure feedforward control, or the combination of a feedforward and feedback controller. A single low-level controller may perform multiple control tasks, although not necessarily simultaneously. Rules in the supervisory controller ensure that only viable sets of control tasks are activated at a time. For instance, we consider the stabilization and preemption of one NTM to be mutually exclusive: only one of these tasks can be executed by the NTM controller simultaneously for a given rational q surface. Mutual exclusive conditions for the activation of these tasks impose that only one is enabled at a time for a given rational q surface.

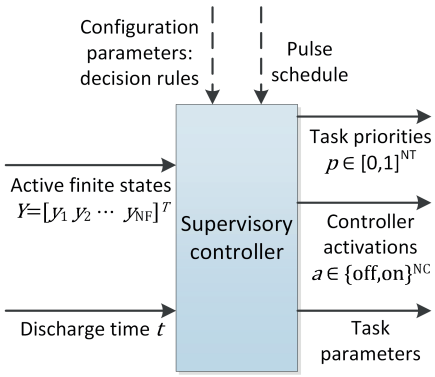

Figure 4.5 – Block diagram of the input and output signals of the supervisory controller. The indices of active finite states originate from the plasma state monitor, discussed in Section 4.3.

For each control task, the supervisory controller executes a set of conditional logic expressions, which depend on the active plasma states and the discharge time. The outcome of each conditional expression enables the task and assigns a priority to it, or disables the task. As an example, Table 4.3 shows abstract examples of decision rules in the proposed supervisory controller.

4.4.2 Supervisory control outputs

The supervisory controller produces multiple outputs, as shown in Figure 4.5. First, it produces the priority for each control task, which is in the range $[0, 1]$. In the proposed framework, these priorities represent the (relative) importance of tasks, and the values are used by the actuator manager to determine an optimal allocation of actuation resources to tasks [Vu et al., 2018]. When a given task priority is larger than zero, the corresponding task is activated and the task execution by the appropriate feedback control algorithm is enabled.

Second, the supervisory controller activates the controller algorithms if the discharge time is within a pre-set activation time window. This allows a control algorithm to run in the background even if none of its tasks are active and it is not in command of any actuation. Last, the supervisory controller sends out a number of signals and parameters that are specific to each control task and are related to its execution. For instance, for a plasma pressure control task, this may include the reference signal for the controlled quantity, while for NTM control tasks this may include the $q = m/n$ target and maximum heating power. Some of these task-specific parameters are discussed in [Vu et al., 2018].

The supervisory input-output relation can be formally expressed as a task priority function $p = g_{\mathrm{P}}(t, Y)$ and a controller activation function $a = g_{\mathrm{A}}(t)$.

Table 4.4 – Decision logic for the simulation in Figure 4.6. Note that all conditions belonging to the same task are mutually exclusive.

Control task	Activation condition	Priority
2/1 mode stabilization	2/1ampl==large & 2/1freq==slow	$p_1 = 1$
	2/1ampl==small & 2/1freq==slow	$p_1 = 0.9$
	2/1ampl==large & 2/1freq==fast	$p_1 = 0.8$
	2/1ampl==small & 2/1freq==fast	$p_1 = 0.7$
2/1 mode preemption	$0.4 < t < 0.8$	$p_2 = 0.5$
2/1 surface pointing	$1 < t < 3$	$p_3 = 0.45$
3/2 mode stabilization	3/2ampl==large & 3/2freq==slow	$p_4 = 0.95$
	3/2ampl==small & 3/2freq==slow	$p_4 = 0.85$
	3/2ampl==large & 3/2freq==fast	$p_4 = 0.75$
	3/2ampl==small & 3/2freq==fast	$p_4 = 0.65$
Kinetic pressure control	$0.35 < t < 1$	$p_5 = 0.6$
Safety profile control	$0.35 < t < 1$	$p_6 = 0.3$

Here, $p \in P$ is the vector of control task priorities where, $P = [0,1]^{N_\mathrm{T}}$, N_T is the number of control tasks, and $a \in A$ is the vector of controller activations, where $A = \{\mathrm{off}, \mathrm{on}\}^{N_\mathrm{C}}$ and N_C is the number of (feedback) controllers. Furthermore, t is the discharge time and $Y = \begin{bmatrix} y_1 & y_2 & \dots & y_{N_\mathrm{F}} \end{bmatrix}^T$ is the column of all active state indices.

4.4.3 Supervisory controller simulation

To illustrate the input-output behaviour, capabilities and possibilities of the chosen architecture of the supervisory controller, we present a simulation with synthetic plasma state signals and a predefined set of decision rules.

The input data consists of artificial signals of appearing and disappearing rotating modes, both $m/n = 2/1$ and $3/2$ with varying amplitude and rotational frequency. The supervisory control rules are listed in Table 4.4 and represent the preprogrammed response for kinetic pressure, safety factor profile control, mode preemption and idle EC beam pointing as well as the real-time response to observed rotating modes. In this simulation example, the real-world problem of prioritizing the suppression and preemption of modes versus kinetic pressure and q-profile control is displayed. Specifically the case where the rotational frequency and amplitude of the modes determines their relative priority: although a $2/1$ mode is more important to suppress than a $3/2$ mode, a sufficiently small and fast $2/1$ mode is less important to suppress given limited resources than a slow, large $3/2$ mode. Although unfavorable safety factor profiles cause rotating modes to appear and therefore control of the safety factor profile is important, the stabilization of modes (when they appear) is valued more important in this

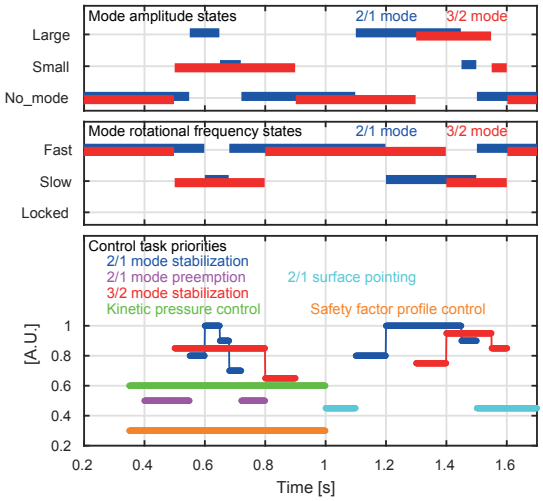

Figure 4.6 – Simulation of the supervisory controller with artificial plasma state signals, illustrative of the supervisory control possibilities. In the top two panels, synthetic rotating mode state signals are given. In the other panel, the priorities for the various control tasks are shown, computed using the decision rules in Table 4.4. Note that depending on the amplitude and frequency of the 2/1 and 3/2 mode, the supervisory controller prioritizes the stabilization of either mode over the other.

case. Therefore the mode stabilization tasks receive a higher priority when a mode is present.

The decision rules internal to the supervisory controller consider the amplitude and frequency of two distinct NTMs, as well as time-based triggers, to prioritize $N_C = 6$ control tasks related to NTM, pressure, and safety factor control. These rules are listed in Table 4.4.

In Figure 4.6, we show the artificial plasma states and resulting control task priorities from the simulation. In this simulation example, the suppression of two appearing and disappearing rotating modes is prioritized over the scheduled tasks of pressure and safety factor profile control.

4.5 Implementation and results on TCV

The plasma state monitor and the supervisory controller have been implemented on the TCV digital control system [Anand et al., 2017] and used in experiments. In this section, the implementation and interfacing to other real-time algorithms is discussed, as well as results of experiments on integrated control on TCV.

4.5.1 Implementation of the plasma state monitor and supervisory controller on the TCV control system

The real-valued plasma state estimates, used in the plasma state monitor described in Section 4.3, are derived from various existing real-time reconstruction algorithms on the TCV control system. These algorithms and their outputs relevant to this work are:

- the rotating mode analysis based on singular value decomposition [Galperti et al., 2014, 2017], producing the likelihoods that the two most dominant modes have mode number m/n=2/1, 3/2 or 3/1,
- a newly implemented phase-locked loop, providing the rotating mode frequency,
- the standard odd-n and even-n rotating mode amplitudes,
- the real-time mode lock analysis, producing the locked mode amplitude for $n = 1$, $n = 2$ and $n = 3$,
- the real-time event detector [Shousha et al., 2018], providing the confinement mode and ELM frequency,
- the real-time equilibrium reconstruction code LIUQE [Moret et al., 2015], producing the plasma current centroid position,
- the measurement of the plasma current, based on spatial integration of magnetic probe measurements surrounding the plasma (see [Moret et al., 2015]),
- the real-time EC raytracing code TORBEAM [Poli et al., 2018], producing the power deposition locations of injected EC beams,
- the RAPTOR-observer [Felici et al., 2011, 2016], estimating the electron temperature profile, safety factor profile and derived quantities such as kinetic normalized pressure and internal inductance,
- the RAPDENS-observer [Blanken et al., 2018b] (this thesis, Chapter 3), estimating the electron density profile.

In Figure 4.7, these reconstruction algorithms, as well as newly implemented postprocessing blocks, the plasma state monitor and the supervisory controller are shown, with the relevant input and output signals. Note that in this setup indeed the reconstruction algorithms are *specific* to TCV, while the finite state machines in the plasma state monitor contain no details of TCV hardware and are truly *tokamak-agnostic*. The FSMs in the plasma state monitor are implemented using the MATLAB Stateflow Toolbox [The Mathworks Inc., b]. The relevant computational node hosting the plasma state monitor, supervisory controller and actuator management runs at a cycle rate of 1kHz.

On the output side, the supervisory controller is interfaced with the actuator manager [Vu et al., 2018] and ultimately to individual controllers, being the interchangeable profile controllers [Kim et al., 2016; Maljaars et al., 2017; Mavkov et al., 2018; Vu et al., 2016] and the NTM controller [Kong et al., 2017]. Next,

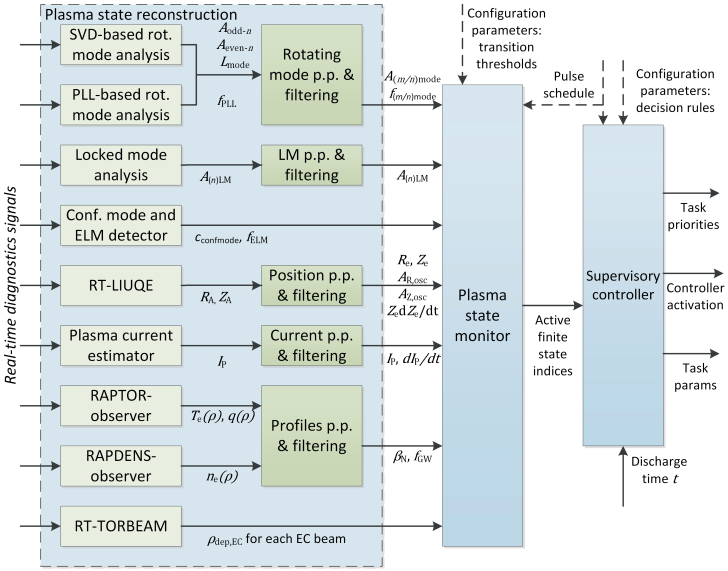

Figure 4.7 – Block diagram of software components related to the plasma state monitor and supervisory control on the TCV digital control system. Various reconstruction algorithm outputs are filtered and processed in order to yield suitable inputs to the finite-state machines. The outputs of the supervisory controller are sent to the actuation resource management and feedback controllers [Vu et al., 2018], as shown in Figure 4.2.

the postprocessing and interface of the reconstruction algorithms to the plasma state monitor, corresponding to the finite state machines that are used in the results, are discussed.

Rotating mode analysis

A rotating MHD analysis algorithm based on a singular value decomposition (SVD), see [Galperti et al., 2014, 2017], is combined with a phase-locked loop to provide information about rotating modes, both using a set of in-vessel poloidal field coils.

The amplitude of odd-n and even-n rotating modes is computed in the standard way by taking the root mean square value of the difference and sum of two toroidally opposed in-vessel poloidal field coils, respectively. These amplitudes are low-pass filtered with a cut-off frequency of 100Hz. Then, a poloidal mode number is assigned to these odd-n and even-n amplitudes yielding m/n numbers, by selecting the maximum over the likelihoods that the two most dominant rotating modes have mode numbers m/n=2/1, 3/1 or 3/2. These likelihoods are provided by the SVD-based algorithm.

Note that for the mode amplitude, we consider the amplitude of the magnetic perturbation measured at the coil locations. At present, there is no reconstruction of the magnetic perturbation at the location of the mode.

In this work, the rotating mode frequency is estimated by a phase-locked loop (PLL) [Best, 2007]. It synchronizes an oscillator to the most dominant periodic component in an appropriate linear combination of toroidally separated poloidal field coil signals. In TCV, rotating modes appear in a wide frequency range up to 10kHz. The PLL is designed to estimate the mode frequency in the range between 500Hz and 10kHz. In the present implementation of the SVD-based analysis, a zero-crossing detector provides an estimate of the rotating mode frequency. Since the PLL does not rely on zero-crossing detection, it is more robust to noise. The resulting mode frequency is low-pass filtered at a cut-off frequency of 100Hz to smooth over multiple periods of the mode. Similarly as above, a poloidal mode number m is assigned to the estimated frequency by selecting the maximum of the likelihoods. The mode acceleration is computed by numerical derivation of the mode frequency. Additional low-pass filtering at a cut-off frequency of 50Hz is applied to reject the noise amplification caused by the numerical differentiation. The reconstructed mode amplitude, frequency and acceleration then feed to the FSMs for the rotating modes, as discussed in Section 4.3.2.

Locked mode analysis

A recently implemented real-time mode lock indicator for toroidally resolved mode numbers on TCV's control system is used [Anand et al., 2017]. The amplitude of locked modes is computed in real time, and is fed to the FSMs for locked modes, see Section 4.3.3. Note that the computation yields the magnetic perturbation amplitude at the coil locations. There is no reconstruction of the physical mode magnitude.

Equilibrium reconstruction and measured plasma current

The magnetic axis position is provided by real-time LIUQE [Moret et al., 2015] and is subtracted from the reference position and low-pass filtered with a time constant of 100ms. It is then fed to the position excursion FSMs, see Section 4.3.4. The position oscillation amplitude in both the radial and vertical directions are computed as the square root of the signal power in the frequency range between 10Hz and 100Hz, with the latter obtained through band-pass filtering. These feed to the FSMs for position oscillations, introduced in Section 4.3.4. Moreover, the vertical velocity is numerically derived from the vertical position. Similar to [Gerhardt et al., 2013], the multiplication $Z_{\mathrm{err}} dZ_{\mathrm{err}}/dt$ is used to indicate unstable vertical movement events, as mentioned in Section 4.3.4.

The plasma current and its time-derivative are used for the plasma current segment states in Section 4.3.1. The plasma current is estimated by the trapeze approximation (see [Moret et al., 2015]). The time-derivative of the plasma current is numerically computed and is low-pass filtered with a second-order filter at a cut-off frequency of 20Hz is applied to reject the noise amplification from numerical differentiation.

4.5.2 Real-time detection of NTMs and locked modes on TCV

In this subsection, the capabilities of the state monitor to detect behaviour of several quantities related to MHD and plasma position control problems is demonstrated.

The results of the plasma state monitoring in TCV discharge #57382 are depicted in Figure 4.8. In this discharge, a 2/1 NTM grows in amplitude, while accelerating and decelerating, before locking. Subsequently, the rotating mode reappears, before a VDE develops and the plasma disrupts. These consecutive events are flagged by the state monitor.

In Figure 4.9, the results of plasma state monitoring results in TCV discharge #59183 are shown. In this discharge, a 2/1 NTM accelerates to twice its initial frequency. Subsequently it disappears while a $n = 2$ locked mode appears at 1.6s. Although further analysis in [Sheikh et al., 2018] reveals that the mode spins up and locks consecutively between 1.6s and 2s, these events happen too fast for the real-time MHD analysis to pick up. These fast transients can be seen in the magnetics spectogram. In the last phase of the discharge, radial and vertical position oscillations develop, before disrupting.

Design tradeoffs exist between the detection delay and detection accuracy. In the present implementation, all input signals u are filtered in order to reduce fast switching between finite states due to signal noise. Similarly, a delay is introduced in filtering out the noise introduced by the numerical derivation of the NTM acceleration from its frequency. These delays introduced by the filters propagate to the state monitor, and will cause delayed (re)actions by the supervisory controller and the task-executing algorithms. For the present purposes of control-focused experiments on TCV, 10ms of delay between the physical event and a supervisory control decision is acceptable.

4.5.3 Experimental results of integrated kinetic profile and NTM control on TCV

In this subsection, the capabilities of the supervisory controller in a TCV discharge to provide prioritized control task is demonstrated. A low-density limited discharge is considered for simultaneous control of the plasma pressure, safety factor profile and NTMs. The goal is to control the plasma pressure and safety

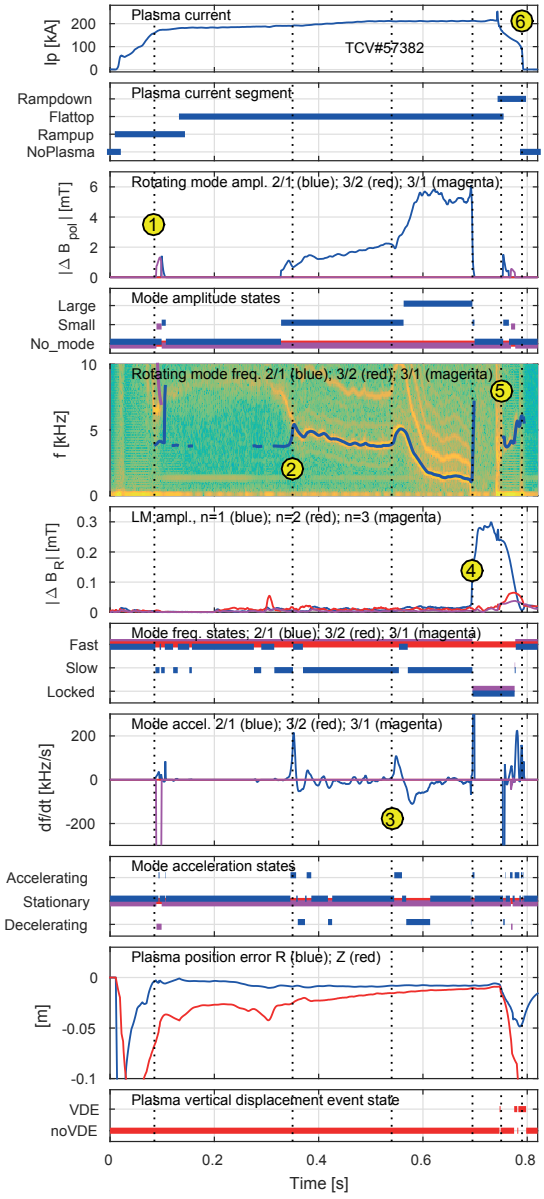

Figure 4.8 – Result of event detection for TCV#57382. At time point ①, a 2/1 mode briefly appears. Around $t = 0.33$s it appears again and is detected at time point ②. The mode briefly accelerates and decelerates after time point ③, before locking at $t = 0.69$s at time point ④. The rotating mode reappears at time point ⑤ after which a VDE develops and the plasma disrupts at time point ⑥.

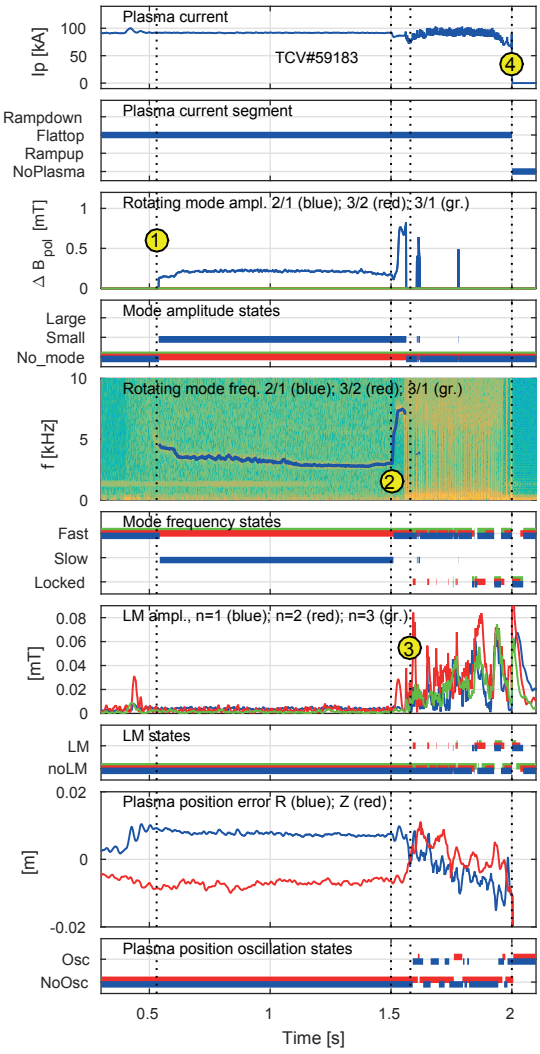

Figure 4.9 – Result of event detection for TCV#59183. A 2/1 NTM appears around 0.55s (time point ①). After a deliberate massive neon injection at $t = 1.5$s (time point ②), the NTM accelerates to 6kHz. At time point ③, the 2/1 NTM disappears while an $n = 2$ locked mode appears. Between 1.6s and 2s, the mode consecutively unlocks and locks [Sheikh et al., 2018], while the plasma position is oscillating. At time point ④ the plasma disrupts.

Table 4.5 – Implemented decision logic for the experimental result in Figure 4.10.

Task	Activation condition	Priority
2/1 NTM stabilization	2/1ampl==large OR 2/1ampl==small	$p_1 = 1$
2/1 NTM preemption	2/1ampl==noNTM AND $0.8 < t < 2$	$p_2 = 0.5$
Beta control	$0.25 < t < 2$	$p_3 = 0.6$
Safety profile control	$0.25 < t < 2$	$p_4 = 0.3$

factor profile, while suppressing NTMs. The supervisory controller assigns the priorities to the tasks. Then, the actuation resource management distributes command over two EC power supplies and the poloidally steerable mirrors on three launchers among the controller algorithms.

In the present implementation on TCV, two controllers are interfaced to the supervisory controller and the actuator management, and a set of control tasks are designated to each controller (see also [Vu et al., 2018]). The control tasks related to rotating mode control, executed by the NTM controller [Kong et al., 2017] are:

- NTM suppression/stabilization at a specified $q = m/n$ target,
- NTM preemption at a specified $q = m/n$ target,
- flux surface tracking, i.e. aiming an EC launcher at a specified q surface without power injection.

The control tasks related to kinetic profile control, executed by the (interchangeable) profile controllers [Kim et al., 2016; Maljaars et al., 2017; Mavkov et al., 2018; Vu et al., 2016] are:

- Plasma pressure β control,
- Inverse safety factor profile $\iota = 1/q$ control.

For the present purposes, the supervisory control decisions are programmed by the user. The supervisory decision logic related to the tasks is shown in Table 4.5. Note that the supervisory controller ensures that at most one of the preemption task and stabilization task of the 2/1 mode is active at a time: the activating conditions for these two tasks are mutually exclusive.

In Figure 4.10, the experimental results of TCV discharge #57813 are presented. Although the mode is not stabilized within the time of the discharge. Still, the supervisory controller evolves the task priorities among the relevant control tasks as intended by the user. It first enables the preemption of a 2/1 mode with limited power on launcher #6. At 1.3s, a 2/1 mode is observed and the supervisor enables the mode suppression task instead of the mode preemption task. This prompts the actuator manager to grant full power availability on launcher #6 to the NTM controller.

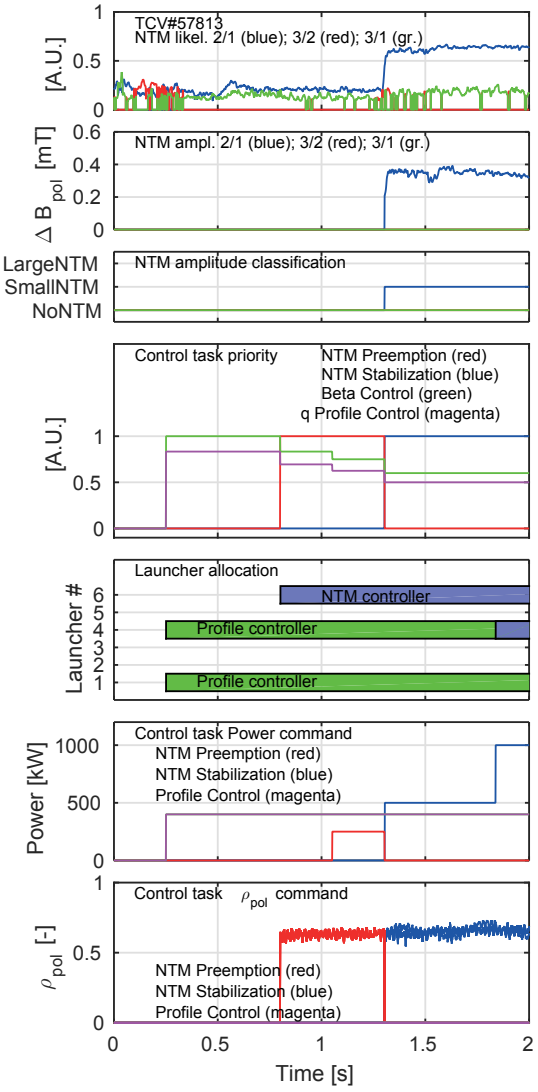

Figure 4.10 – Experimental result of simultaneous pressure and NTM control on TCV #57813. The supervisory controller executes the decision logic shown in Table 4.5. Furthermore, the actuator manager distributes the available EC launchers and power supplies to the NTM controller and the profile controller. The appearance of an NTM prompts the supervisory controller to assign top priority to the stabilization task.

Due to technical limitations of the EC system, the gyrotrons of launcher #4 and #6 are on the same power supply such that equal power is delivered by these launchers. Yet, they are not depositing power on the same location. At 1.8s, the actuator manager assigns a second EC launcher (#4) to the mode suppression task. This prompts the NTM controller to direct launcher #4 to the resonant surface, where launcher #4 was previously aimed at the magnetic axis. This experiment demonstrates the succesful execution of the implemented supervisory control rules, and showcases its capability to manage the execution of multiple control tasks by multiple controllers.

4.6 Discussion

In this work, we provide a supervisory control framework that deals with several aspects of advanced plasma control. The supervisory controller needs to be programmed by the user according to the intended experimental needs, similar to [Eidietis et al., 2018; Rapson et al., 2016]. However, extending the method to include a complete set of functionalities as required in a reactor is challenging. First, design of a supervisory controller for a highly complex system is difficult due to the large dimension of the state space [Wonham et al., 2017]. Second, manual design of a supervisory controller for large systems may lead to a supervisor that contains blocking situations, i.e. when the system ends up in a state from which it cannot be driven toward a desired state. A tailored solution from the control engineering community is the requirement-driven design procedure [Baeten et al., 2016; Ramadge and Wonham, 1987], which provides an optimized supervisory controller that is guaranteed to be non-blocking, correct and controllable. This solution may be the topic of future work. Yet, the current proposed method remains generic, promising and flexible to be extended using a requirement-driven design procedure.

In this work, the fact that the signal thresholds that determine the state transitions must be specified by the user implies that the physical meaning of the finite states is arbitrary. In other research, the semantics of events was expressed in terms of a statistical proximity to disruptions [De Vries et al., 2011; Gerhardt et al., 2013]. For future applications of supervisory control in tokamaks, the meaning of finite states must be dictated by requirements on the real-time control capability, which includes proximity to disruptions.

In the present implementation on TCV, the set of finite state machines does not cover the complete set of plasma, hardware and control system states that is relevant for real-time control as required in future tokamaks and reactors. As such, this research forms a proof of concept for supervised plasma control. For the purposes of experimental tokamaks, only coverage of states related to the intended experiments is needed, as done in this work and [Eidietis et al., 2018; Rapson et al., 2016]. In [De Vries et al., 2011; Gerhardt et al., 2013], larger sets of events are considered, in an offline analysis focussed on disruption causes.

Yet, our work can be extended with additional finite state representations for the plasma, and is valuable for the application of event detection to coordination of all relevant control tasks in future reactors.

Moreover, the selection of available diagnostics and reconstruction algorithms determines the physical meaning of the discrete states. In this work, several states are expressed in terms of plasma quantities, such as plasma current, position, density, temperature, safety factor and EC beam deposition. However, the real-time MHD analysis provides the amplitude of NTMs and locked modes as being the perturbation amplitude as observed at the magnetic field coils, rather than the island width or the magnetic field perturbation amplitude local to the mode. This implies that these quantities are not (yet) *tokamak-agnostic*. For the present experimental purposes on TCV, this does not limit the applicability. Yet, in the future a *tokamak-agnostic* state representation is valuable. This allows for developed and proven controller algorithms that take *tokamak-agnostic* state quantities as input to be ported to other tokamak PCS's.

4.7 Conclusions and outlook

4.7.1 Conclusions

In next-generation tokamaks and reactors, the plasma control system should deal with the magnetic control as well as a number of control tasks associated with the performance and stability of the plasma. These control tasks will rely on a limited shared set of actuators. Supervisory control is a necessary component in future tokamak reactor control systems.

At present, state-of-the-art supervisory control for advanced plasma control on tokamaks is done at ASDEX-Upgrade and DIII-D. In our work, feedback controllers are integrated in a generic architecture for advanced plasma control to allow for the real-time coordination of multiple objectives. This work extends the research at DIII-D by a strict separation between event detection and execution, which allows for a modular and extendable architecture.

This paper shows the design, implementation and experimental demonstration of a generic plasma state monitor and supervisory controller. This supervisory controller sets the relative priority of various control tasks, based on a set of finite states of the plasma. These priorities determine how the available actuators are allocated to the tasks, which is computed by an actuator allocation algorithm. The signal thresholds that determine the boundaries between the finite states must be specified by the user, and need to be adjusted according to the experimental needs of the user. In this way, the supervisory controller ensures that the most important task at any time has highest priority, since it coordinates all tasks. Abstracting the integration of controllers and actuators using tasks and their prioritization yields a less complex control system design in (future) machines, where the number of actuators, controller algorithms and

tasks (control functionalities) is much larger than in present-day devices.

In the implementation on TCV, the monitored discrete states are the real-time estimated NTM state, discharge segment, locked mode amplitude and plasma position excursions, oscillations and vertical displacement events.

This work showed that the proposed framework can be used to carry out experiments on TCV with real-time centralized prioritization of control tasks, which can be programmed by the user. In this paper, we have shown real-time event detection and supervisory control for a set of plasma states. More specifically, we have demonstrated examples of rotating mode, mode lock and plasma displacement monitoring, as well as an experimental result of supervisory control of multiple control tasks based on NTM occurence. In the latter, the supervisory controller distributes priority among NTM control tasks and kinetic profile control tasks.

The plasma state monitor and supervisory controller are suited to perform physics experiments on TCV. Moreover, this work supports the integration of control capabilities for ITER and DEMO.

4.7.2 Outlook

In the future, depending on the real-time available diagnostic signals and plasma state reconstruction algorithms, the number of state machines and discrete states can be extended at will to monitor more complex situations. This is facilitated by the generic architecture of the proposed PCS. Our generic layout can be easily extended with additional discrete states that cover the entire range of physical and technical events. The latter includes both hardware as well as control system events and states.

The semantics of the discrete states may be refined using physics interpretation, statistical analysis [De Vries et al., 2011; Gerhardt et al., 2013], as well as hardware and software design specifications [Humphreys et al., 2015]. Future applications of the finite-state modeling framework include development of generic algorithms to assess the plasma health and proximity to disruptions based on tokamak-independent representations of the plasma state, from physics interpretation or statistics. These can be tested on existing devices before being ported to larger machines.

In this work, some of the plasma states are not defined in terms of *tokamak-agnostic* quantities. In the future, a real-time reconstruction of the MHD mode width based on the equilibrium and coil geometry can provide a *tokamak-agnostic* interpretation of the MHD states.

The supervisory control framework should be tested on a larger set of discharges, such that its performance can be quantified in a statistical sense.

Note that the control tasks in this work are limited to control of performance and stability quantities. First, additional tasks may be added, e.g. related to control of other MHD and impurity removal [Snipes et al., 2010]. Second, the

domain of tasks may be extended to include plasma termination and emergency handling tasks [Humphreys et al., 2015; Raupp et al., 2017; Woo et al., 2018].

4.8 Acknowledgments

The authors gratefully acknowledge the contributions of Dr. M. Maraschek of IPP Garching for development of the locked mode detection algorithm, as well as Dr. M. Reich and Dr. E. Poli of IPP Garching for their assistance in porting RT-TORBEAM to TCV. The authors also gratefully acknowledge W.P.M.H. Heemels of Eindhoven University of Technology and J. Berkery of Columbia University for useful discussions and comments. This work has been carried out within the framework of the EUROfusion Consortium and has received funding from the EURATOM research and training programme 2014-2018 under grant agreement No 633053. The views and opinions expressed herein do not necessarily reflect those of the European Commission. This work was supported in part by the Netherlands Organization for Scientific Research via F. Felici's VENI grant: "Control of plasma profiles in a fusion reactor" (no. 680.47.436). This work was supported in part by the Swiss National Science Foundation.

Chapter 5

Conclusions, discussion and recommendations

In this thesis two important objectives related to control of tokamak plasmas were addressed, which are stated in Section 1.4. First, algorithms for estimation and feedback control of the plasma density in tokamaks were developed and validated experimentally. Second, a control system architecture for the integration of plasma monitoring, supervision, control and actuator management was proposed and applied in experiments. In this chapter, these contributions are summarized and conclusions regarding the objectives set in Section 1.4 are drawn. Furthermore, the achievements are discussed and recommendations for future research are given.

5.1 Conclusions

Reliable real-time estimation and control of the plasma density profile is essential for the operation of next-generation tokamaks and nuclear fusion reactors. In reactor-relevant plasma scenarios, a high density in the plasma core must be achieved and the sensitivity of the density control to disturbances should be minimized. The density profile must be estimated in real time using all available yet scarce measurements. This is crucial for density feedback control, and also valuable for determining measurements validity, auxiliary heating constraints, and control of pressure and magnetohydrodynamics. The first research objective, which is set in Section 1.4, is:

Research objective 1: Develop model-based techniques for the estimation and control of the spatial distribution of the plasma particle density in tokamaks.

This objective has been addressed by the following contributions. In Chapter 2, a control-oriented model for the evolution of the plasma electron density was developed. From this model, a density profile observer was derived using Kalman filtering and applied to TCV data in simulations. In Chapter 3, the observer was applied in experiments on ASDEX Upgrade and TCV. Also, a model-based feedback controller for the profile-averaged density was applied to density control in TCV experiments.

On ASDEX Upgrade, the observer was successful in estimating the core density in high-density pellet-fuelled discharges. This observer uses multiple measurement signals and can deal with various measurement errors. The estimated profiles were compared to offline available Thomson scattering measurements. While the estimation accuracy at the plasma core meets the requirements for the experiment, the plasma edge density is underestimated. This is due to an inaccurate modeling of the H-mode transport barrier. Also, density transients due to pellet ablation are not estimated; while the density transient due to pellet arrival can be modeled, there is no real-time detection of pellet arrival at present. The observer provides reliable estimates in presence of measurement faults. False positives of fringe jumps occur when the measurement signal resembles one, due to transient phases in discharges. Moreover, pellet-induced transients and fringe jumps prove difficult to distinguish on the interferometry signals available to the PCS.

On TCV, the observer and the feedback controller were used in experiments on integrated profile control. The agreement of the real-time estimated density profile with offline available Thomson scattering measurements is sufficient within the scientific goal of the experiments. Shortcomings in estimation quality are attributed to limitations of the source models and measurement models. A feedback controller was tuned on the density evolution model using H_∞-norm minimization to provide low-frequency tracking and disturbance rejection. In experiments, it is successful in ramping up the plasma density to the desired constant value and maintaining this density with zero steady-state error for the duration of the flat top phase, despite the presence of disturbances from ECCD.

The second research objective that is set in Section 1.4 is:

Research objective 2: Develop a control system architecture including a plasma supervision system that allows operating a tokamak close to operational limits.

This objective has been addressed by the contributions in Chapter 4. First, a plasma control system architecture for task-based supervisory control was de-

veloped. The proposed architecture is characterized by a separation of algorithms for state estimation, supervision, actuator management and (feedback) controllers. In order to provide a generic solution allowing for future extensions and portability to other tokamaks, the finite state definitions, signal interfaces and task definitions in this architecture are device-independent. In other words, they do not depend on the specific measurements and actuators of a given tokamak.

Second, finite state models were developed that represent the uncontrollable behavior of the plasma. In particular, the finite states represent distinct operational regimes, proximity to operational limits and deviations from references. In the proposed architecture, a suite of state reconstruction codes provide the continuous-valued state. From this, the discrete state of the plasma is derived. The supervisory controller has user-defined decision rules based on the discrete state for the activation and prioritization of control tasks.

Third, the proposed architecture was implemented on the plasma control system of TCV, and applied in experiments on integrated control of kinetic pressure and neoclassical tearing modes. The plasma state monitor and supervisory controller provide satisfactory behavior in detecting the presence of neoclassical tearing modes and in prioritizing the appropriate control tasks to suppress NTMs and control the pressure using the available actuation resources.

The estimation and control algorithms developed in these chapters form a substantial step towards model-based control and integration of control and supervision on tokamaks. Given the generality of the developed framework, the proposed methods and algorithms can be extended for the application to ITER and DEMO.

5.2 Discussion

In this thesis, a number of techniques is employed for model-based control of tokamak plasmas. These techniques are evaluated in view of other efforts in modeling and control of tokamaks.

5.2.1 Control-oriented real-time capable density profile evolution modeling

The RAPDENS model is capable of simulating the electron density of a discharge period faster than physical time. In this thesis, the models are based on first principles, empirical modeling and heuristics. While this allows for self-consistency (i.e. no density measurements are needed to set boundary conditions) the accuracy is limited. Higher accuracy is obtained by full physics codes, such as SOLPS [Wiesen et al., 2015, 2017], CRONOS [Artaud et al., 2010], ASTRA [Pereverzev and Yushmanov, 2002] and METIS [Artaud et al., 2018]. Except for the latter, these are not real-time capable at present. In the

latter, the density evolution must be prescribed. The practice of control-oriented real-time capable modeling is essential for control applications, observer design, co-simulation or faster than real-time predictions.

The RAPDENS code shares a number of design features with the RAPTOR code [Felici and Sauter, 2012; Felici et al., 2011] for the evolution of the poloidal flux and the electron temperature, as well as derived quantities such as normalized pressure, safety factor profile and internal inductance. Recently the equations for the transport of density and temperature of multiple particle species in the main plasma were added [Felici et al., 2018a]. Both codes are physics-based, real-time capable, and return local linearizations of the nonlinear dynamics. These qualities have led to various applications in plasma control [Felici et al., 2018b; Maljaars et al., 2017; Ravensbergen et al., 2018; Teplukhina et al., 2017].

The RAPDENS model was constructed to be device-independent and portable to different devices, such as ITER. This is done in two ways. First, the code for the one-step ahead prediction of the state (as used in the observer implementations) receives all machine parameters and signal dimensions via configuration parameters, rather than being hard-coded. Second, all device-specific routines (such as input signal checks and forward measurement model evaluations) are separated from the model and observer codes. In the observer implementations on ASDEX Upgrade and TCV, the device-specific routines are coded in separate Simulink blocks. Hence, the implementations are device-independent, allowing for easy adaptations to different models, devices, diagnostics and actuators.

5.2.2 Results of density estimation and control

The experimental results of real-time density profile estimation and density control presented in this thesis are successful within the scientific goals of the respective experiments.

Still there is room for improvement in the profile estimation accuracy. Naturally, offline profile fit methods that include Thomson scattering data (such as [Fischer et al., 2010]) perform better. However, real-time Thomson scattering is not available at the time of writing on neither TCV nor ASDEX Upgrade.

In ASDEX Upgrade discharges, the edge density is underestimated when compared to Thomson scattering measurements, but the core density is estimated with sufficient accuracy. In TCV discharges, sufficient estimation accuracy of the profile was obtained after careful tuning of the covariance matrices of the Extended Kalman filter. In general, the transport coefficients in the RAPDENS model must be tuned such that it matches a (reference) discharge in a predictive simulation. The inaccuracies in the model used in the profile observer contribute to inaccuracies in the profile estimation. This indicates the limitations of the model at present.

Moreover, inaccuracies in real-time equilibrium reconstructions can propa-

gate to the forward measurement models. Detailed evaluation of the accuracy of (real-time) equilibrium reconstructions is a difficult subject that would benefit from further attention.

An ad-hoc forward measurement model for Bremsstrahlung was used in the density profile observer. The use of this model is justified under the assumption that the plasma equilibrium, temperature and effective charge change slowly in time with respect to the plasma density. In cases where this assumption does not hold, the profile estimates from the observer may be inaccurate. Explicitly integrating the estimation of density, temperature and effective charge with time-varying equilibria can resolve this issue. This is proposed in [Fischer et al., 2010; Reusch et al., 2018], but is not implemented in a real-time observer.

Although the observer does not detect all fringe jumps in the interferometry measurements on ASDEX Upgrade, the profile estimation results remains within reason. This is unlike a previous method [Mlynek, 2010], which proved vulnerable to multiple simultaneous fringe jumps. In feedback control experiments on TCV, the control error converges to zero during the flat-top. However, oscillatory behavior during ramp-up indicate that the controller gains are too high for the response in this part of the discharge. Better tuning would reduce these oscillations.

In ITER and DEMO, the experimental time available for controller tuning is costly and limited. Feedback controllers must perform adequately on first deployment. The proposed feedback controller does not explicitly account for actuator limits and the constraint of one-sided actuation, such that the addition of an anti-windup scheme is necessary to prevent integrator windup. While it therefore does not give significant performance improvements over other design methods, its design procedure demonstrates the tuning and testing based on a model of the system response. Such model-based design and testing procedures are increasingly used in the field of tokamaks [Boyer and Schuster, 2015; Boyer et al., 2014; Felici et al., 2018b; Goumiri et al., 2016; Maljaars et al., 2017; Moreau et al., 2015; Ravensbergen et al., 2018; Wehner et al., 2017], and are essential for ITER and beyond.

In this thesis, the estimation and control of the electron density is considered. The ion densities of the main fuel species (deuterium and tritium) and impurities (e.g. tungsten) could be added similarly for the purpose of prediction, estimation, monitoring and/or control.

5.2.3 Considerations of the applied estimation and control techniques

Model-based design techniques were used for the density profile observer and feedback controller. While the observer uses Extended Kalman filtering, derived from a model in time domain, the feedback control law is designed using a frequency-domain design approach. This was done for the following reasons:

- the feedback control problem of a volume- or profile-averaged density is a SISO problem. Loop-shaping or H_∞-norm minimization are intuitive methods to solve this problem.
- the profile estimation problem is a distributed problem: a parameterization of the profile using multiple coefficients must be estimated from multiple measurements and a prediction model. Kalman filtering is a straightforward method to solve this problem.
- the recursive Extended Kalman filter equations allow for easy incorporation of time-varying covariance matrices and time-varying measurement channel selection. This is needed when the measurements become unavailable during operation, or noise increases.

One can argue whether both observer and feedback controller can be designed using similar techniques, i.e. either using time-domain techniques (e.g. LQG, LQR, Kalman filtering, model-predictive control [Maciejowski, 2002; Mayne et al., 2000]) or frequency-domain techniques (e.g. loop-shaping, H_∞-norm minimization [Skogestad and Postlethwaite, 2001]). A number of challenges are to be taken into consideration for doing so. These are discussed next.

The dynamics of tokamak plasmas are inherently nonlinear. This can prove difficult for frequency-domain approaches to estimation and control, which traditionally assume linear dynamics. Moreover, in many control challenges in tokamaks, the transient response is as important as the steady-state responses. Examples of transient behavior in tokamak plasmas that require an emphasis on the design of the responsible controller include plasma ramp-up and ramp-down, confinement regime transitions, magnetic configuration transitions and disturbances on the kinetic profiles from MHD events.

Density control on ITER will have to be treated as a multivariable problem: the core density must be controlled to achieve the desired fusion power, while the edge density must be controlled to achieve beneficial divertor conditions and to limit the heat flux onto plasma-facing components [Gribov et al., 2007].

Model predictive control (MPC) is an attractive option for feedback controller design in tokamaks. It can explicitly handle actuation constraints and state constraints by optimizing a future input sequence to avoid such constraints and minimize the (future) control error and actuator inputs. In the case of density control, it can be required to take the actuation constraints such as minimum and maximum fuelling by gas puffing and pellet injection into account. Also, it can be required to take state constraints such as low plasma density (leading to neutral beam shinethrough) and high density (e.g. the Greenwald limit and ECH reflection) into account. However, accurate models must be available in order to apply MPC. These must be capable of self-consistently predicting the relevant state (the density profile, wall inventory and neutral density) evolution on a time horizon in the order of the retention and recycling timescale (i.e. the time scale on which the wall absorbs and releases particles), but with resolution of the particle confinement time. The former is in the order of 100ms to seconds

on TCV and ASDEX Upgrade, while the latter is in the order of 10ms [Weisen et al., 1996]. Accurate models for the dynamic evolution of the wall inventory that can be used for real-time predictions on the recycling time scale do not exist. Moreover, there is at present no effective way of measuring the wall inventory in real time. This poses a challenge in the application of MPC to density control. However, with certain modeling improvements and research efforts proposed in Section 5.3, the RAPDENS code can qualify for model predictive density control on tokamaks.

The range of scenarios that will be done in ITER is limited compared to present-day experimental tokamaks. The latter is aimed at physics exploration in a wider range of operating conditions. This implies that if a single scenario is repeated many times and the wall conditions do not change significantly between discharges, then the predictive quality of control-oriented models tuned on a set of discharges improves. This will be even more true for DEMO and prototype fusion reactors which will essentially operate at one operating point. Iterative learning control (ILC) [Bristow et al., 2006], as applied to density control in [Ravensbergen et al., 2018], can prove valuable for control of repeated discharges.

5.2.4 Plasma state monitoring and supervisory control

A supervisory control system will form an integral part of the ITER control system [Kurihara et al., 2008; Raupp et al., 2014, 2017; Treutterer et al., 2017; Walker et al., 2014]. The supervisory controller will not only be responsible for coordinating all control loops in normal operation, but will also be responsible for off-normal event handling and disruption avoidance. The integration of controller algorithms on the ITER plasma control system (PCS) to simultaneously control all relevant plasma quantities is a major challenge compared to current practice, where feedback controllers are often developed and used individually.

In Chapter 4, a demonstration of task-based supervisory control on TCV was shown. This was done in close collaboration with [Vu et al., 2018], in which additional experimental results on TCV are shown. The jointly proposed architecture integrates plasma state monitoring, supervisory control, and actuator management and allocation. Moreover, it incorporates device-independent finite-state models and device-independent signal interfaces between the various algorithms. This allows portability to different tokamaks, and ease of integrating existing controllers in the implementation. These qualities imply that the architecture and algorithms developed on present-day tokamaks can be exploited for use on the ITER PCS. It can be tested on various ITER scenarios in simulations on the PCS simulation platform (PCSSP) [Walker et al., 2015].

In this work, the supervisory control laws are user-specified. This is in contrast with requirement-driven synthesis techniques [Wonham et al., 2017]. However, the application of supervisory control to tokamaks in this thesis is novel

and marks a first step. Moreover, the modeling of discrete events using finite state machines as done in this thesis allows the application of dedicated supervisor control synthesis tools [Wonham et al., 2017]. These provide an efficient and systematic way to generate supervisory controllers for discrete event systems subject to formal requirements [Baeten et al., 2016; Ramadge and Wonham, 1987]. Numerous applications of this procedure exist in control engineering research for industrial systems [Korssen et al., 2017; Reniers et al., 2017; van der Sanden et al., 2015; Theunissen et al., 2014]. Especially for large complex systems with many requirements such as ITER and DEMO, such synthesis tools will be essential since the design, validation and testing of a supervisory controller are otherwise too complex and error-prone to do manually.

5.2.5 Extension to other fields

The tools developed in this thesis can be applied outside of nuclear fusion science. Control of distributed systems is becoming increasingly important in high-tech industry. For example in precision motion systems, spatial temperature variations can cause mechanical displacements leading to reduced accuracy. In order to obtain higher accuracy, the thermal dynamics can be modeled and the temperature distributions can be controlled, see [Bikcora et al., 2014; Evers et al., 2018; Habets et al., 2016; van den Hurk et al., 2018; Morishima et al., 2015; Veldman et al., 2018]. Also, for high-bandwidth motion systems, the flexible modes of mechanical structures must be identified, estimated and suppressed [Oomen, 2018]. Another example is local hyperthermia for improved cancer treatment [Deenen et al., 2018; Issels, 2008; Luo et al., 2015]. In this application, human body tissue must be locally heated while keeping the surrounding tissue at body temperature.

The observer developed in this thesis used a discretized PDE model. This can also be applied in the above cases, where the underlying dynamics are governed by PDEs.

5.3 Recommendations

Based on the achieved results, the expertise gained during development and testing of the control algorithms, and the requirements of future tokamaks, a number of future research directions are recommended.

5.3.1 Density estimation in fusion reactors

For the purpose of redundancy, it is recommended that as many as possible measurements systems on ITER are available in real time to the PCS, rather than the minimum set of measurements dedicated to control. It is wise for long pulse operation to integrate all available measurements in a density profile observer,

in case one or more fails during a discharge due to e.g. neutron irradiation or thermal loads. A method based on Bayesian inference, such as Kalman filtering [Anderson and Moore, 1979] or as used in [Fischer et al., 2010; Reusch et al., 2018], is recommended. The need to integrate multiple diagnostics depends on the requirements for estimation and control. This illustrated next.

Different measurements systems have different qualities that make them attractive for density profile estimation. Interferometers typically have high temporal resolution. However, long wavelength interferometers can be sensitive to fringe jumps, in particular induced by pellet injection [Lang et al., 2012]. For ITER, a dispersion interferometer is designed and a tangential array of interferometers/polarimeters is designed [Akiyama et al., 2016; Van Zeeland et al., 2018]. Both are insensitive by design to fringe jumps and mechanical vibrations [Akiyama et al., 2015; Van Zeeland et al., 2006], but offer limited spatial resolution. On the other hand, Thomson scattering measurements on present-day devices typically have a lower temporal resolution (which can be limiting for feedback control) than interferometers, but have better spatial resolution. The ITER Thomson scattering system is designed with a higher repetition rate (50-100Hz) [Bassan et al., 2016; Scannell et al., 2017]. Last, Bremsstrahlung measurements can be incorporated. However, it is recommended to explicitly integrate the estimation of density, temperature and effective charge in a Bayesian framework [Reusch et al., 2018] since the Bremsstrahlung depends (nonlinearly) on these quantities.

In ITER and DEMO, the real-time density profile estimate should be based on all available core and edge measurements. Future advances in control-oriented modeling as described later in this section will also improve the accuracy of model-based density profile observers. This is particularly important in DEMO, where measurements are limited.

5.3.2 Model predictive control of density in fusion reactors

Since ITER and DEMO are necessarily operated close to operational limits, the control of the plasma density must not only achieve zero steady-state error with respect to the reference, but also attenuate disturbances, avoid density limits and reduce control errors as much as possible through plasma transients like confinement regime transitions (such as low to high confinement transitions and backtransitions). Model predictive control is an attractive option for density control on ITER, since actuation limits and state limits are explicitly taken into account [Maciejowski, 2002; Mayne et al., 2000]. However, it requires the development of accurate models as discussed in the next section.

5.3.3 Real-time capable density profile evolution modeling for control

Better predictive accuracy of the density profile evolution model RAPDENS and accuracy of the associated observer and controller designs can be obtained by the combination of multiple efforts:

- particle transport modeling via semi-empirical scalings (e.g. a Bohm-gyroBohm-like model [Erba et al., 1998], a critical-gradient model [Hillesheim et al., 2013; Jenko et al., 2001], or empirical scaling [Witrant et al., 2007]), via identification from data (e.g. [van Berkel et al., 2014a,b]) or via reduced models from gyrokinetics [Angioni et al., 2011] (as done in e.g. [Citrin et al., 2015]). See also [Angioni et al., 2009] for an overview.
- inclusion of the coupled dynamics of the profiles of density, momentum and/or temperature for multiple particle species. Recently this was initiated in [Felici et al., 2018a], although self-consistent models of particle sources arising from particle recycling, wall retention and fuelling are not (yet) used.
- real-time capable modeling of scrape-off layer and wall dynamics (such as recycling, retention and pumping) through reduced-order models of particle kinetics in e.g. SOLPS [Reiter et al., 2005; Wiesen et al., 2015] or understanding and analysis of experiments e.g. [Asakura, 2004; Brezinsek et al., 2013; Loarer et al., 2007; Rohde et al., 2009a,b]. In particular, the effects of confinement transitions on these dynamics must be explicitly modeled with sufficient predictive capability for control purposes.

The latter may also prove useful for model-based control of the detachment front location and heat flux on divertor tiles.

5.3.4 Finite state modeling, state monitoring and supervisory control in fusion reactors

In order to extend the supervisory control presented in this thesis, a number of improvements can be made. These are in the realm of finite state modeling, as well as design of supervisory controllers.

The set of finite states considered in Chapter 4 partially correspond those considered in [De Vries et al., 2011; Gerhardt et al., 2013], which represent disruption causes. In future work, the finite state models should be extended to cover a more complete set of plasma and hardware states, covering more operational limits, deviations from references, hardware/actuator states and controller algorithm states.

Manual design of a supervisory controller for large systems may lead to a supervisor that contains blocking situations, i.e. when the system ends up in a state from which it cannot be driven toward a desired state. Moreover, it is hard

to verify that all requirements are satisfied for large-scale complex systems [Wonham et al., 2017]. In order to generate supervisory controllers for large complex tokamaks such as ITER and DEMO, a requirement-driven design procedure is recommended [Baeten et al., 2016; Van Beek et al., 2014; Wonham et al., 2017]. This can produce a supervisory controller that is guaranteed to be non-blocking, correct and controllable with respect to the formal requirements.

One important step is the definition of formal requirements for a supervisory controller. This will allow the design as well as validation of the supervisor against those requirements. Ultimately, the supervisory controller can be tested in simulation on the PCSSP in various realistic ITER scenarios. These scenarios should not only include nominal operation, but also physical and technical events that could lead to disruptions, such as unexpected MHD activity, large impurity influxes and actuator failure.

Although many questions and ideas for future work are raised by this work, this thesis provides contributions to the modeling, estimation and control of tokamak plasmas that are important to produce energy from nuclear fusion.

Bibliography

Akiyama, T., Yasuhara, R., Kawahata, K., Nakayama, K., et al., Development of dispersion interferometer for magnetic confinement plasmas and high-pressure plasmas, *Journal of Instrumentation*, 10(09):P09022–P09022, 2015, doi:10.1088/1748-0221/10/09/P09022.

Akiyama, T., Sirinelli, A., Watts, C., Shigin, P., et al., Design of a dispersion interferometer combined with a polarimeter to increase the electron density measurement reliability on ITER, *Review of Scientific Instruments*, 87(11):11E133, 2016, doi:10.1063/1.4962050.

Anand, H., Coda, S., Felici, F., Galperti, C., and Moret, J.M., A novel plasma position and shape controller for advanced configuration development on the TCV tokamak, *Nuclear Fusion*, 57(12), 2017, doi:10.1088/1741-4326/aa7f4d.

Anderson, B.D.O., and Moore, J.B., *Optimal filtering*, Prentice-Hall, Inc., 1979.

Angioni, C., Fable, E., Greenwald, M., Maslov, M., et al., Particle transport in tokamak plasmas, theory and experiment, *Plasma Physics and Controlled Fusion*, 51(12):124017, 2009, doi:10.1088/0741-3335/51/12/124017.

Angioni, C., McDermott, R., Fable, E., Fischer, R., et al., Gyrokinetic modelling of electron and boron density profiles of H-mode plasmas in ASDEX Upgrade, *Nuclear Fusion*, 51(2): 023006, 2011, doi:10.1088/0029-5515/51/2/023006.

Artaud, J., Basiuk, V., Imbeaux, F., Schneider, M., et al., The CRONOS suite of codes for integrated tokamak modelling, *Nuclear Fusion*, 50(4):043001, 2010, doi:10.1088/0029-5515/50/4/043001.

Artaud, J., Imbeaux, F., Garcia, J., Giruzzi, G., et al., METIS: a fast integrated tokamak modelling tool for scenario design, *Nuclear Fusion*, 58(10):105001, 2018, doi:10.1088/1741-4326/aad5b1.

Asakura, N., Wall pumping and saturation in divertor tokamaks, *Plasma Physics and Controlled Fusion*, 46(12B):B335–B347, 2004, doi:10.1088/0741-3335/46/12B/029.

Baeten, J.C.M., van de Mortel-Fronczak, J.M., and Rooda, J.E., Integration of Supervisory Control Synthesis in Model-Based Systems Engineering, In *Complex Systems*, pages 39–58. Springer, Cham, 2016, ISBN 978-0521462457, doi:10.1017/CBO9780511758744.

Barry, S., *The extension of the FIR interferometer of TCV to a polarimeter and measurements of the Faraday rotation caused by the poloidal magnetic field*, PhD thesis, University of Ireland, Cork, 1999.

Barry, S., Nieswand, C., Bühlmann, F., Prunty, S.L., and Mansfield, H.M., Improvement of interferometric measurements on far-infrared polarimeter interfermeter systems, *Review of Scientific Instruments*, 67(5):1814, 1998, doi:10.1063/1.1146979.

Barton, J.E., Boyer, M.D., Shi, W., Schuster, E., et al., Toroidal current profile control during low confinement mode plasma discharges in DIII-D via first-principles-driven model-based robust control synthesis, *Nuclear Fusion*, 52(12):123018, 2012.

Barton, J.E., Besseghir, K., Lister, J., and Schuster, E., Physics-based control-oriented modeling and robust feedback control of the plasma safety factor profile and stored energy dynamics in ITER, *Plasma Physics and Controlled Fusion*, 57(11):115003, 2015, doi:10.1088/0741-3335/57/11/115003.

Bassan, M., Andrew, P., Kurskiev, G., Mukhin, E., et al., Thomson scattering diagnostic systems in ITER, *Journal of Instrumentation*, 11(01):C01052–C01052, 2016, doi:10.1088/1748-0221/11/01/C01052.

Bell, M., The Tokamak Fusion Test Reactor, In *Magnetic Fusion Energy*, chapter 6, pages 119–166. Woodhead Publishing, 2016, doi:10.1016/B978-0-08-100315-2.00006-4.

Belo, P., Romanelli, M., Parail, V., Corrigan, G., et al., Coupled core/SOL modelling of fuelling requirements during the current ramp-up of ITER L-mode plasmas, In *42nd EPS Conference on Plasma Physics*. European Physical Society (EPS), 2015.

van Berkel, M., Vandersteen, G., Geerardyn, E., Pintelon, R., et al., Frequency domain sample maximum likelihood estimation for spatially dependent parameter estimation in PDEs, *Automatica*, 50(8):2113–2119, 2014a, doi:10.1016/J.AUTOMATICA.2014.05.027.

van Berkel, M., Zwart, H.J., Hogeweij, G.M.D., Vandersteen, G., et al., Estimation of the thermal diffusion coefficient in fusion plasmas taking frequency measurement uncertainties into account, *Plasma Physics and Controlled Fusion*, 56(10):105004, 2014b, doi:10.1088/0741-3335/56/10/105004.

Best, R.E., *Phase-Locked Loops: Design, Simulation, and Applications, Sixth Edition*, McGraw-Hill, London, 2007, ISBN 9780071493758.

Biel, W., de Baar, M.R., Dinklage, A., Felici, F., et al., DEMO diagnostics and burn control, *Fusion Engineering and Design*, 96:8–15, 2015, doi:10.1016/j.fusengdes.2015.01.046.

Bikcora, C., Weiland, S., and Coene, W.M.J., Thermal Deformation Prediction in Reticles for Extreme Ultraviolet Lithography Based on a Measurement-Dependent Low-Order Model, *IEEE Transactions on Semiconductor Manufacturing*, 27(1):104–117, 2014, doi:10.1109/TSM.2014.2298360.

Blanken, T.C., Felici, F., Galperti, C., Vu, N.M.T., et al., Real-time plasma state monitoring and supervisory control on TCV, *Nuclear Fusion*, 2018a, doi:10.1088/1741-4326/aaf451.

Blanken, T.C., Felici, F., Rapson, C.J., de Baar, M.R., and Heemels, W.P.M.H., Control-oriented modeling of the plasma particle density in tokamaks and application to real-time density profile reconstruction, *Fusion Engineering and Design*, 126:87–103, 2018b, doi:10.1016/j.fusengdes.2017.11.006.

Blum, J., Boulbe, C., and Faugeras, B., Reconstruction of the equilibrium of the plasma in a tokamak and identification of the current density profile in real time, *Journal of Computational Physics*, 231(3):960–980, 2012, doi:doi:10.1016/j.jcp.2011.04.005.

Boboc, A., Gelfusa, M., Murari, A., Gaudio, P., and the JET EFDA contributors, Recent developments of the JET far-infrared interferometer-polarimeter diagnostic, *Review of Scientific Instruments*, 81(10), 2010, doi:10.1063/1.3478146.

Boivin, R., Diagnostics for magnetic fusion power plants, In *Magnetic Fusion Energy*, chapter 18, pages 549–575. Woodhead Publishing, 2016, doi:10.1016/B978-0-08-100315-2.00018-0.

Boncagni, L., Pucci, D., Piesco, F., Zarfati, E., et al., A control approach for plasma density in tokamak machines, *Fusion Engineering and Design*, 88(6):1097–1100, 2013, doi:10.1016/j.fusengdes.2013.03.025.

de Boor, C., *A practical guide to splines*, volume 27 of *Applied Mathematical Science*, Springer-Verlag, 2001.

Boozer, A.H., Theory of tokamak disruptions, *Physics of Plasmas*, 19(5):058101, 2012, doi:10.1063/1.3703327.

Boyer, M.D., and Schuster, E., Nonlinear burn condition control in tokamaks using isotopic fuel tailoring, *Nuclear Fusion*, 55(8):083021, 2015, doi:10.1088/0029-5515/55/8/083021.

Boyer, M.D., Barton, J., Schuster, E., Walker, M.L., et al., Backstepping control of the toroidal plasma current profile in the DIII-D Tokamak, *IEEE Transactions on Control Systems Technology*, 22(5):1725–1739, 2014, doi:10.1109/TCST.2013.2296493.

Braams, C., and Stott, P., *Nuclear Fusion*, Taylor & Francis, 2002, ISBN 978-0-7503-0705-5, doi:10.1201/9781420033786.

van den Brand, H., de Baar, M.R., Lopes Cardozo, N.J., and Westerhof, E., Evaluating neoclassical tearing mode detection with ECE for control on ITER, *Nuclear Fusion*, 53(1): 013005, 2013, doi:10.1088/0029-5515/53/1/013005.

van den Brand, H., de Baar, M.R., van Berkel, M., Blanken, T.C., et al., A model-based, multichannel, real-time capable sawtooth crash detector, *Plasma Physics and Controlled Fusion*, 58(7), 2016, doi:10.1088/0741-3335/58/7/075002.

Brelen, H.E.O., An adaptive plasma density controller at JET, *Fusion Technology*, 27:162–170, 1994.

Brezinsek, S., Loarer, T., Philipps, V., Esser, H., et al., Fuel retention studies with the ITER-Like Wall in JET, *Nuclear Fusion*, 53(8):083023, 2013, doi:10.1088/0029-5515/53/8/083023.

Bristow, D., Tharayil, M., and Alleyne, A., A survey of iterative learning control, *IEEE Control Systems*, 26(3):96–114, 2006, doi:10.1109/MCS.2006.1636313.

Cassandras, C.G., and Lafortune, S., editors, *Introduction to Discrete Event Systems*, Springer US, Boston, MA, 2008, ISBN 978-0-387-33332-8, doi:10.1007/978-0-387-68612-7.

Chiang, K.L., Hallock, G.A., Wootton, A.J., and Wang, L., Fast Tokamak plasma flux and electron density reconstruction technique, *Review of Scientific Instruments*, 68(1):894–897, 1997, doi:http://dx.doi.org.dianus.libr.tue.nl/10.1063/1.1147714.

Citrin, J., Breton, S., Felici, F., Imbeaux, F., et al., Real-time capable first principle based modelling of tokamak turbulent transport, *Nuclear Fusion*, 55(9):092001, 2015, doi:10.1088/0029-5515/55/9/092001.

Coda, S., Ahn, J., Albanese, R., Alberti, S., et al., Overview of the TCV tokamak program: scientific progress and facility upgrades, *Nuclear Fusion*, 57(10):102011, 2017, doi:10.1088/1741-4326/aa6412.

De Vries, P.C., Johnson, M.F., Alper, B., Buratti, P., et al., Survey of disruption causes at JET, *Nuclear Fusion*, 51(5):053018, 2011, doi:10.1088/0029-5515/51/5/053018.

Deenen, D., Maljaars, E., Sebeke, L., de Jager, A., et al., Offset-Free Model Predictive Control for Enhancing MR-HIFU Hyperthermia in Cancer Treatment, In *IFAC Conference on Nonlinear Model Predictive Control (NMPC)*, Madison, USA, 2018.

Donné, A.J.H., High spatial resolution interferometry and polarimetry in hot plasmas, *Review of Scientific Instruments*, 66:3407–3423, 1995, doi:10.1063/1.1145516.

Donné, A.J.H., Costley, A.E., Barnsley, R., Bindslev, H., et al., Chapter 7: Diagnostics, *Nuclear Fusion*, 47(6):S337–S384, 2007, doi:10.1088/0029-5515/47/6/S07.

Donné, A.J.H., Barth, C.J., and Weisen, H., Chapter 4: Laser-aided plasma diagnostics, *Fusion Science and Technology*, 53(2):397–430, 2008, doi:10.13182/FST08-A1676.

Eidietis, N., Choi, W., Hahn, S., Humphreys, D., et al., Implementing a finite-state off-normal and fault response system for disruption avoidance in tokamaks, *Nuclear Fusion*, 58(5): 056023, 2018, doi:10.1088/1741-4326/aab62c.

Erba, M., Aniel, T., Basiuk, V., Becoulet, A., and Litaudon, X., Validation of a new mixed Bohm/gyro-Bohm model for electron and ion heat transport against the ITER, Tore Supra and START database discharges, *Nuclear Fusion*, 38(7):1013, 1998, doi:10.1088/0029-5515/38/7/305.

Evers, E., de Jager, A., and Oomen, T., Improved Local Rational Method by incorporating system knowledge: with application to mechanical and thermal dynamical systems, In *18th IFAC Symposium on System Identification*, Stockholm, Sweden, 2018.

Felici, F., *Real-time control of tokamak plasmas: from control of physics to physics-based control*, PhD thesis, École Polytechnique Fédérale de Lausanne (EPFL), CH-1015 Lausanne, Switzerland, 2011.

Felici, F., and Sauter, O., Non-linear model-based optimization of actuator trajectories for tokamak plasma profile control, *Plasma Physics and Controlled Fusion*, 54(2), 2012, doi:10.1088/0741-3335/54/2/025002.

Felici, F., Sauter, O., Coda, S., Duval, B.P., et al., Real-time physics-model-based simulation of the current density profile in tokamak plasmas, *Nuclear Fusion*, 51(8):083052, 2011, doi:10.1088/0029-5515/51/8/083052.

Felici, F., De Baar, M.R., and Steinbuch, M., A dynamic state observer for real-time reconstruction of the tokamak plasma profile state and disturbances, In *Proceedings of the American Control Conference*, pages 4816–4823. IEEE, 2014a, ISBN 978-1-4799-3274-0, doi:10.1109/ACC.2014.6858781.

Felici, F., Le, H.B., Paley, J.I., Duval, B.P., et al., Development of real-time plasma analysis and control algorithms for the TCV tokamak using Simulink, *Fusion Engineering and Design*, 89(3):165–176, 2014b, doi:10.1016/j.fusengdes.2013.11.010.

Felici, F., Blanken, T.C., Maljaars, E., van den Brand, H., et al., Real-time model-based plasma state estimation, monitoring and integrated control in TCV, ASDEX-Upgrade and ITER, In *26th IAEA Fusion Energy Conference*, pages EX/P8–33, 2016.

Felici, F., Citrin, J., Teplukhina, A.A., Redondo, J., et al., Real-time-capable prediction of temperature and density profiles in a tokamak using RAPTOR and a first-principle-based transport model, *Nuclear Fusion*, 58(9):096006, 2018a, doi:10.1088/1741-4326/aac8f0.

Felici, F., Kudlacek, O., Ravensbergen, T., Treutterer, W., et al., Model-based design, simulation and testing of an electron temperature profile controller on ASDEX Upgrade, *submitted to Nuclear Fusion*, 2018b.

Feng, Y., Wolle, B., and Hübner, K., New, simplified technique for calculating particle source rates due to neutral beam injection into tokamaks, *Computer Physics Communications*, 88 (2-3):161–172, 1995, doi:10.1016/0010-4655(95)00013-6.

Ferron, J.R., Walker, M.L., Lao, L.L., St. John, H.E., et al., Real time equilibrium reconstruction for Tokamak discharge control, *Nuclear Fusion*, 38.7:1055, 1998, doi:10.1088/0029-5515/38/7/308.

Fielding, S.J., McCracken, G.M., and Stott, P.E., Recycling in gettered and diverted discharges in DITE tokamak, *Journal of Nuclear Materials*, 76 & 77:273–278, 1978, doi:10.1016/0022-3115(78)90157-5.

Fischer, R., and Dinklage, A., Integrated data analysis of fusion diagnostics by means of the Bayesian probability theory, *Review of Scientific Instruments*, 75(10):4237–4239, 2004, doi:10.1063/1.1787607.

Fischer, R., Wendland, C., Dinklage, A., Gori, S., et al., Thomson scattering analysis with the Bayesian probability theory, *Plasma Physics and Controlled Fusion*, 44(8):306, 2002, doi:10.1088/0741-3335/44/8/306.

Fischer, R., Fuchs, C.J., Kurzan, B., Suttrop, W., et al., Integrated Data Analysis of Profile Diagnostics at ASDEX Upgrade, *Fusion Science and Technology*, 58(2):675–684, 2010, doi:10.13182/FST10-110.

Freidberg, J.P., *Plasma Physics and Fusion Energy*, Cambridge University Press, 2007, ISBN 9780511755705, doi:10.1017/CBO9780511755705.

Furno, I., Weisen, H., Carey, C., Angioni, C., et al., A new method for the inversion of interferometry data using basis functions derived from singular value decomposition of local measurements in tokamak plasmas, *Plasma Physics and Controlled Fusion*, 47(1):49–69, 2005, doi:10.1088/0741-3335/47/1/004.

Galante, M., Reusch, L., Den Hartog, D., Franz, P., et al., Determination of Z eff by integrating measurements from x-ray tomography and charge exchange recombination spectroscopy, *Nuclear Fusion*, 55(12):123016, 2015, doi:10.1088/0029-5515/55/12/123016.

Galperti, C., Marchetto, C., Alessi, E., Minelli, D., et al., Development of real-time MHD markers based on biorthogonal decomposition of signals from Mirnov coils, *Plasma Physics and Controlled Fusion*, 56(11), 2014, doi:10.1088/0741-3335/56/11/114012.

Galperti, C., Coda, S., Duval, B.P., Llobet, X., et al., Integration of a Real-Time Node for Magnetic Perturbations Signal Analysis in the Distributed Digital Control System of the TCV Tokamak, *IEEE Transactions on Nuclear Science*, 64(6):1446–1454, 2017, doi:10.1109/TNS.2017.2711625.

Gerhardt, S.P., Bell, R.E., Diallo, A., Gates, D., et al., Disruptions, disruptivity and safer operating windows in the high-β spherical torus NSTX, *Nuclear Fusion*, 53(4):043020, 2013, doi:10.1088/0029-5515/53/4/043020.

Giannone, L., Fischer, R., McCarthy, P., Odstrcil, T., et al., Improvements for real-time magnetic equilibrium reconstruction on ASDEX Upgrade, *Fusion Engineering and Design*, 100:519–524, 2015, doi:10.1016/j.fusengdes.2015.07.029.

Gil, C., Boboc, A., Barbuti, A., Pastor, P., and the JET EFDA Contributors, Analysis of the JET FIR interferometer beam phase changes during plasmas and application for fast fringe jump corrections by electronics, *Journal of Physics: Conference Series*, 227:012032, 2010, doi:10.1088/1742-6596/227/1/012032.

Goumiri, I.R., Rowley, C.W., Sabbagh, S.A., Gates, D.A., et al., Modeling and control of plasma rotation for NSTX using neoclassical toroidal viscosity and neutral beam injection, *Nuclear Fusion*, 56(3):036023, 2016, doi:10.1088/0029-5515/56/3/036023.

Greenwald, M., Terry, J., Wolfe, S., Ejima, S., et al., A new look at density limits in tokamaks, *Nuclear Fusion*, 28(12):2199–2207, 1988, doi:10.1088/0029-5515/28/12/009.

Gribov, Y., Humphreys, D., Kajiwara, K., Lazarus, E.A., et al., Chapter 8: Plasma operation and control, *Nuclear Fusion*, 47(6):S385, 2007, doi:10.1088/0029-5515/47/6/S08.

Habets, M., Scholten, J., Weiland, S., and Coene, W., Multi-mirror adaptive optics for control of thermally induced aberrations in extreme ultraviolet lithography, In *Proc. SPIE 9776, Extreme Ultraviolet (EUV) Lithography VII*, volume 9776, page 97762D. International Society for Optics and Photonics, 2016, doi:10.1117/12.2219168.

la Haye, R.J., Neoclassical tearing modes and their control, *Physics of Plasmas*, 13(5):055501, 2006, doi:10.1063/1.2180747.

Hender, T.C., Wesley, J.C., Bialek, J., Bondeson, A., et al., Chapter 3: MHD stability, operational limits and disruptions, *Nuclear Fusion*, 47(6):S128–S202, 2007, doi:10.1088/0029-5515/47/6/S03.

Henderson, M., Saibene, G., Darbos, C., Farina, D., et al., The targeted heating and current drive applications for the ITER electron cyclotron system, *Physics of Plasmas*, 22(2): 021808, 2015, doi:10.1063/1.4908598.

Hennen, B.A., Westerhof, E., Nuij, P.W.J.M., Oosterbeek, J.W., et al., Real-time control of tearing modes using a line-of-sight electron cyclotron emission diagnostic, *Plasma Physics and Controlled Fusion*, 52(10):104006, 2010, doi:10.1088/0741-3335/52/10/104006.

Hillesheim, J.C., DeBoo, J.C., Peebles, W.A., Carter, T.A., et al., Experimental characterization of multiscale and multifield turbulence as a critical gradient threshold is surpassed in the DIII-D tokamak, *Physics of Plasmas*, 20(5):056115, 2013, doi:10.1063/1.4807123.

Hinton, F.L., and Hazeltine, R.D., Theory of plasma transport in toroidal confinement systems, *Review of Modern Physics*, 48(2):239–308, 1976, doi:10.1103/RevModPhys.48.239.

Horton, L., and JET Contributors, Joint European Torus, In *Magnetic Fusion Energy*, chapter 8, pages 215–259. Woodhead Publishing, 2016, doi:10.1016/B978-0-08-100315-2.00008-8.

Hughes, T.J.R., *The Finite Element Method*, Englewood Cliffs, NJ: Prentice Hall, 1987.

Humphreys, D., Ambrosino, G., De Vries, P., Felici, F., et al., Novel aspects of plasma control in ITER, *Physics of Plasmas*, 22(2):021806, 2015, doi:10.1063/1.4907901.

van den Hurk, D., Weiland, S., and van Berkel, K., Modeling and localized feedforward control of thermal deformations induced by a moving heat load, In *2018 SICE International Symposium on Control Systems (SICE ISCS)*, pages 171–178, Tokyo, Japan, 2018. IEEE, ISBN 978-4-9077-6458-6, doi:10.23919/SICEISCS.2018.8330172.

Hutchinson, I.H., *Principles of Plasma Diagnostics*, Cambridge University Press, Cambridge, 2002, ISBN 9780511613630, doi:10.1017/CBO9780511613630.

IAEA, Summary of the ITER Final Design Report, Technical report, International Atomic Energy Agency, Vienna, 2001.

Intergovernmental Panel on Climate Change, Climate Change 2007: Synthesis Report., Technical report, IPCC, Geneva, 2007.

Intergovernmental Panel on Climate Change, Global Warming of 1.5C, an IPCC special report on the impacts of global warming of 1.5C above pre - industrial levels and related global greenhouse gas emission pathways, in the context of strengthening the global response to the threat of climate chang, Technical report, IPCC, Geneva, 2018.

International Energy Agency, World Energy Outlook, Technical report, Paris, 2016.

Issels, R., Hyperthermia adds to chemotherapy, *European Journal of Cancer*, 44(17):2546–2554, 2008, doi:10.1016/J.EJCA.2008.07.038.

Janky, F., Hron, M., Havlicek, J., Varavin, M., et al., Plasma density control in real-time on the COMPASS tokamak, *Fusion Engineering and Design*, 96:637–640, 2015, doi:10.1016/j.fusengdes.2015.04.065.

Jenko, F., Dorland, W., and Hammett, G.W., Critical gradient formula for toroidal electron temperature gradient modes, *Physics of Plasmas*, 8(9):4096–4104, 2001, doi:10.1063/1.1391261.

Juhn, J.W., Hwang, Y.S., Hahn, S.H., Nam, Y.U., et al., A global particle/balance model for Wall Interaction Analysis Associated with Open- and Closed/loop density control experiments in KSTAR, In *24th IAEA Fusion Energy Conference*, 2012.

Keilhacker, M., Gibson, A., Gormezano, C., and Rebut, P.H., The scientific success of JET, *Nuclear Fusion*, 41(12):1925–1966, 2001, doi:10.1088/0029-5515/41/12/217.

Kim, D., Kim, S., Felici, F., Maljaars, E., and Sauter, O., An active feedback plasma profile control approach applied to TCV plasmas and perspectives toward ITER, In *43rd EPS Conference on Plasma Physics*. European Physical Society (EPS), 2016.

Kirneva, N.A., Behn, R., Canal, G.P., Coda, S., et al., High density experiments in TCV ohmically heated and L-mode plasmas, *Plasma Physics and Controlled Fusion*, 57(2): 025002, 2015, doi:10.1088/0741-3335/57/2/025002.

Kong, M., Sauter, O., Blanken, T.C., Felici, F., et al., Real-time control of neoclassical tearing modes and its integration with multiple controllers in the TCV tokamak, In *44th EPS Conference on Plasma Physics*, page 152, Belfast, Northern Ireland (UK), 2017. European Physical Society (EPS).

Koponen, J.P.T., and Dumbrajs, O., Electron density profile reconstruction from multichannel microwave interferometer data at W7-AS, *Review of Scientific Instruments*, 68:4038–4042, 1997, doi:10.1063/1.1148378.

Korssen, T., Dolk, V., van de Mortel-Fronczak, J., Reniers, M., and Heemels, M., Systematic Model-Based Design and Implementation of Supervisors for Advanced Driver Assistance Systems, *IEEE Transactions on Intelligent Transportation Systems*, 19(2):1–12, 2017, doi:10.1109/TITS.2017.2776354.

Kurihara, K., Lister, J.B., Humphreys, D.A., Ferron, J.R., et al., Plasma control systems relevant to ITER and fusion power plants, *Fusion Engineering and Design*, 2008, doi:10.1016/j.fusengdes.2008.06.027.

Lang, P.T., Suttrop, W., Belonohy, E., Bernert, M., et al., High-density H-mode operation by pellet injection and ELM mitigation with the new active in-vessel saddle coils in ASDEX Upgrade, *Nuclear Fusion*, 52(2):023017, 2012, doi:10.1088/0029-5515/52/2/023017.

Lang, P.T., Blanken, T.C., Dunne, M., McDermott, R.M., et al., Feedback controlled, reactor relevant, high-density, high-confinement scenarios at ASDEX Upgrade, *Nuclear Fusion*, 58 (3), 2018, doi:10.1088/1741-4326/aaa339.

Lauret, M., Lennholm, M., de Baar, M.R., and Heemels, W.P.M.H., Pacing control of sawtooth and ELM oscillations in tokamaks, *Plasma Physics and Controlled Fusion*, 58(12):124004, 2016, doi:10.1088/0741-3335/58/12/124004.

Lauret, M., Wehner, W., Schuster, E., Holcomb, C.T., et al., Current profile and energy control in DIII-D plasmas using discrete-time variable-structure control, In *2017 25th Mediterranean Conference on Control and Automation (MED)*, pages 99–104. IEEE, 2017, ISBN 978-1-5090-4533-4, doi:10.1109/MED.2017.7984102.

Loarer, T., Brosset, C., Bucalossi, J., Coad, P., et al., Gas balance and fuel retention in fusion devices, *Nuclear Fusion*, 47(9):1112–1120, 2007, doi:10.1088/0029-5515/47/9/007.

Loarte, A., Lipschultz, B., Kukushkin, A.S., Matthews, G.F., et al., Chapter 4: Power and particle control, *Nuclear Fusion*, 47(6):S203, 2007, doi:10.1088/0029-5515/47/6/S04.

Luo, X., de Jager, A., Heijman, E., and Heemels, W.P.M.H., Set-Based MPC with an Application to Enhanced Local Hyperthermia for Cancer Treatment, In *IFAC Conference on Nonlinear Model Predictive Control (NMPC)*, pages 477–482, Seville, Spain, 2015.

Luxon, J., A design retrospective of the DIII-D tokamak, *Nuclear Fusion*, 42(5):313, 2002, doi:10.1088/0029-5515/42/5/313.

Maciejowski, J.M., *Predictive control with constraints*, Pearson Education Ltd., 2002.

Mackay, D., *Sustainable Energy - without the hot air*, UIT Cambridge Ltd., Cambridge, 2009, ISBN 978-0-9544529-3-3.

Maddison, G.P., Turner, A., Fielding, S.J., and You, S., Global modelling of tank gas density and effects on plasma density control in MAST, *Plasma Physics and Controlled Fusion*, 48 (1):71–107, 2006, doi:10.1088/0741-3335/48/1/007.

Maljaars, E., and Felici, F., Actuator allocation for integrated control in tokamaks: architectural design and a mixed-integer programming algorithm, *Fusion Engineering and Design*, 122:94–112, 2017, doi:10.1016/J.FUSENGDES.2017.09.004.

Maljaars, E., Felici, F., de Baar, M.R., van Dongen, J., et al., Control of the tokamak safety factor profile with time-varying constraints using MPC, *Nuclear Fusion*, 55(2):023001, 2015, doi:10.1088/0029-5515/55/2/023001.

Maljaars, E., Felici, F., Blanken, T.C., Galperti, C., et al., Profile control simulations and experiments on TCV: A controller test environment and results using a model-based predictive controller, *Nuclear Fusion*, 57(12), 2017, doi:10.1088/1741-4326/aa8c48.

Maraschek, M., Gude, A., Igochine, V., Zohm, H., et al., Path-oriented early reaction to approaching disruptions in ASDEX Upgrade and TCV in view of the future needs for ITER and DEMO, *Plasma Physics and Controlled Fusion*, 60(1):014047, 2018, doi:10.1088/1361-6587/aa8d05.

Mavkov, B., Witrant, E., Prieur, C., Maljaars, E., et al., Experimental validation of a Lyapunov-based controller for the plasma safety factor and plasma pressure in the TCV tokamak, *Nuclear Fusion*, 58(5):056011, 2018, doi:10.1088/1741-4326/aab16a.

Mayne, D.Q., Rawlings, J.B., Rao, C.V., and Scokaert, P.O.M., Constrained model predictive control: stability and optimality, *Automatica*, 36(6):789–814, 2000, doi:10.1016/S0005-1098(99)00214-9.

McCracken, G.M., and Stott, P.E., *Fusion: the energy of the universe*, Academic Press, 2nd edition, 2012, ISBN 9780123846563.

Mechoud, S., Witrant, E., Dugard, L., and Moreau, D., Joint diffusivity and source estimation in tokamak heat transport, In *American Control Conference (ACC)*, Washington DC, United States, 2013. IEEE, doi:10.1109/ACC.2013.6580566.

Mlynek, A., *Real-time control of the plasma density profile on ASDEX Upgrade*, PhD thesis, Ludwig-Maximilians-Universität München, 2010.

Mlynek, A., Reich, M., Giannone, L., Treutterer, W., et al., Real-time feedback control of the plasma density profile on ASDEX Upgrade, *Nuclear Fusion*, 51(4):43002, 2011, doi:10.1088/0029-5515/51/4/043002.

Mlynek, A., Pautasso, G., Maraschek, M., Eixenberger, H., and Upgrade, T.A., Infrared Interferometry with Submicrosecond Time Resolution in Massive Gas Injection Experiments on ASDEX Upgrade, *Fusion Science and Technology*, 61(4):290–300, 2012, doi:10.13182/FST12-A13582.

Mlynek, A., Casali, L., Ford, O., and Eixenberger, H., Fringe jump analysis and implementation of polarimetry on the ASDEX Upgrade DCN interferometera), *Review of Scientific Instruments*, 85(11):11D408, 2014, doi:10.1063/1.4890574.

Morari, M., and Zafiriou, E., *Robust Process Control*, Prentice Hall, Englewood Cliffs, 1989.

Moreau, D., Walker, M.L., Ferron, J., Liu, F., et al., Integrated magnetic and kinetic control of advanced tokamak plasmas on DIII-D based on data-driven models, *Nuclear Fusion*, 53 (6), 2013, doi:doi:10.1088/0029-5515/53/6/063020.

Moreau, D., Artaud, J., Ferron, J., Holcomb, C., et al., Combined magnetic and kinetic control of advanced tokamak steady state scenarios based on semi-empirical modelling, *Nuclear Fusion*, 55(6):063011, 2015, doi:10.1088/0029-5515/55/6/063011.

Moreno, V.M., and Pigazo, A., editors, *Kalman Filter Recent Advances and Applications*, InTechOpen, 2009, ISBN 978-953-307-000-1, doi:10.5772/56411.

Moret, J.M., Duval, B.P., Le, H.B., Coda, S., et al., Tokamak equilibrium reconstruction code LIUQE and its real time implementation, *Fusion Engineering and Design*, 91:1–15, 2015, doi:10.1016/j.fusengdes.2014.09.019.

Morishima, T., van Ostayen, R., van Eijk, J., and Munnig Schmidt, R.H., Thermal displacement error compensation in temperature domain, *Precision Engineering*, 42:66–72, 2015, doi:10.1016/J.PRECISIONENG.2015.03.012.

Murari, A., Zabeo, L., Boboc, A., Mazon, D., and Riva, M., Real-time recovery of the electron density from interferometric measurements affected by fringe jumps, *Review of Scientific Instruments*, 77(7):73505, 2006, doi:10.1063/1.2219731.

Neu, R., Kallenbach, A., Zohm, H., and the ASDEX Upgrade team, ASDEX Upgrade, In *Magnetic Fusion Energy*, chapter 5, pages 93–118. Woodhead Publishing, 2016, doi:10.1016/B978-0-08-100315-2.00005-2.

Olofsson, K.E., Choi, W., Humphreys, D.A., La Haye, R.J., et al., Electromechanical modelling and design for phase control of locked modes in the DIII-D tokamak, *Plasma Physics and Controlled Fusion*, 58(4):045008, 2016, doi:10.1088/0741-3335/58/4/045008.

Oomen, T., Advanced Motion Control for Precision Mechatronics: Control, Identification, and Learning of Complex Systems, *IEEJ Journal of Industry Applications*, 7(2):127–140, 2018, doi:10.1541/ieejjia.7.127.

Paley, J.I., Coda, S., Duval, B., Felici, F., and Moret, J.M., Architecture and commissioning of the TCV distributed feedback control system, *17th IEEE-NPSS Real Time Conference, RT10*, 2010, doi:10.1109/RTC.2010.5750487.

Pankin, A., McCune, D., Andre, R., Bateman, G., and Kritz, A., The tokamak Monte Carlo fast ion module NUBEAM in the national transport code collaboration library, *Computer Physics Communications*, 159(3):157–184, 2004, doi:doi:10.1016/j.cpc.2003.11.002.

Park, H.K., A new asymmetric Abel-inversion method for plasma interferometry in tokamaks, *Plasma Physics and Controlled Fusion*, 31:2035, 1989, doi:10.1088/0741-3335/31/13/007.

Pereverzev, G., and Yushmanov, P.N., ASTRA Automated System for TRansport Analysis in a Tokamak, Technical Report 5/98, IPP Report, 2002.

Pironti, A., and Walker, M.L., Control of tokamak plasmas, *Control Systems, IEEE*, 25(5): 24–29, 2005, doi:10.1109/MCS.2005.1512793.

Pochelon, A., Goodman, T., Henderson, M., Angioni, C., et al., Energy confinement and MHD activity in shaped TCV plasmas with localized electron cyclotron heating, *Nuclear Fusion*, 39, 1999.

Poli, E., Bock, A., Lochbrunner, M., Maj, O., et al., TORBEAM 2.0, a paraxial beam tracing code for electron-cyclotron beams in fusion plasmas for extended physics applications, *Computer Physics Communications*, 225:36–46, 2018, doi:10.1016/j.cpc.2017.12.018.

Quarteroni, A., Sacco, R., and Fausto, S., *Numerical Mathematics*, Springer, 2007.

Ramadge, P.J., and Wonham, W.M., Supervisory Control of a Class of Discrete Event Processes, *SIAM Journal on Control and Optimization*, 25(1):206–230, 1987, doi:10.1137/0325013.

Rapson, C.J., Reich, M., Stober, J., and Treutterer, W., Actuator management for ECRH at ASDEX Upgrade, *Fusion Engineering and Design*, 96-97:694–697, 2015, doi:10.1016/j.fusengdes.2015.01.007.

Rapson, C.J., Felici, F., Galperti, C., Lang, P.T., et al., Experiments on actuator management and integrated control at ASDEX Upgrade, *Fusion Engineering and Design*, 123:603–606, 2016, doi:10.1016/j.fusengdes.2017.03.014.

Rathgeber, S.K., Fischer, R., Fietz, S., Hobirk, J., et al., Estimation of profiles of the effective ion charge at ASDEX Upgrade with Integrated Data Analysis, *Plasma Physics and Controlled Fusion*, 52(9):095008, 2010, doi:10.1088/0741-3335/52/9/095008.

Raupp, G., Walker, M.L., Ambrosino, G., De Tommasi, G., et al., Event generation and simulation of exception handling with the ITER PCSSP, In *Fusion Engineering and Design*, volume 89, 2014, ISBN 09203796, doi:10.1016/j.fusengdes.2014.04.068.

Raupp, G., Pautasso, G., Rapson, C.J., Treutterer, W., et al., Preliminary exception handling analysis for the ITER plasma control system, *Fusion Engineering and Design*, 123:541–545, 2017, doi:10.1016/j.fusengdes.2017.05.013.

Ravensbergen, T., de Vries, P.C., Felici, F., Blanken, T.C., et al., Density control in ITER: an iterative learning control and robust control approach, In *Nuclear Fusion*, volume 58, page 016048, 2018, doi:10.1088/1741-4326/aa95ce.

Reiter, D., Baelmans, M., and Börner, P., The EIRENE and B2-EIRENE Codes, *Fusion Science and Technology*, 47(2):172–186, 2005, doi:10.13182/FST47-172.

Reniers, M., van de Mortel-Fronczak, J., and Roelofs, K., Model-Based Engineering of Supervisory Controllers for Cyber-Physical Systems, In *Industrial Internet of Things*, pages 111–136. Springer, Cham, 2017, ISBN 978-3-319-42559-7, doi:10.1007/978-3-319-42559-7_5.

Reusch, L.M., Nornberg, M.D., Goetz, J.A., and Den Hartog, D.J., Using integrated data analysis to extend measurement capability (invited), *Review of Scientific Instruments*, 89 (10):10K103, 2018, doi:10.1063/1.5039349.

Riccardo, V., Chapter 7: Disruption Studies in JET, *Fusion Science and Technology*, 53(4): 1064–1079, 2008, doi:10.13182/FST08-A1747.

Rohde, V., Kallenbach, A., Mertens, V., Neu, R., and the ASDEX Upgrade Team, Wall retention of deuterium and gaseous impurities in all tungsten ASDEX Upgrade, *Plasma Physics and Controlled Fusion*, 51(12):124033, 2009a, doi:10.1088/0741-3335/51/12/124033.

Rohde, V., Mayer, M., Mertens, V., Neu, R., et al., Dynamic and static deuterium inventory in ASDEX upgrade with tungsten first wall, *Nuclear Fusion*, 49(8):085031, 2009b, doi:10.1088/0029-5515/49/8/085031.

Romanelli, M., Parail, V., da Silva Aresta Belo, P., Corrigan, G., et al., Modelling of plasma performance and transient density behaviour in the H-mode access for ITER gas fuelled scenarios, *Nuclear Fusion*, 55(9), 2015, doi:doi:10.1088/0029-5515/55/9/093008.

Sánchez, J., Nuclear fusion as a massive, clean, and inexhaustible energy source for the second half of the century: brief history, status, and perspective, *Energy Science & Engineering*, 2(4):165–176, 2014, doi:10.1002/ese3.43.

van der Sanden, B., Reniers, M., Geilen, M., Basten, T., et al., Modular model-based supervisory controller design for wafer logistics in lithography machines, In *2015 ACM/IEEE 18th International Conference on Model Driven Engineering Languages and Systems, MODELS 2015*, pages 416–425, Ottawa, Canada, 2015. IEEE, ISBN 9781467369084, doi:10.1109/MODELS.2015.7338273.

Scannell, R., Maslov, M., Naylor, G., O'Gorman, T., et al., Design advances of the Core Plasma Thomson Scattering diagnostic for ITER, *Journal of Instrumentation*, 12(11): C11010–C11010, 2017, doi:10.1088/1748-0221/12/11/C11010.

Sheikh, U.A., Duval, B.P., Galperti, C., Maraschek, M., et al., Disruption avoidance through the prevention of NTM destabilization in TCV, *Nuclear Fusion*, 58(10):106026, 2018, doi:10.1088/1741-4326/aad924.

Shousha, R., Akkermans, G.R.A., Felici, F., Blanken, T.C., et al., A real-time model-based detector of LH-transitions, HL-transitions and ELMs and its applications to TCV, *to be submitted to Nuclear Fusion*, 2018.

Skogestad, S., and Postlethwaite, I., *Multivariable Feedback Control Analysis and Design*, John Wiley & Sons, Inc., second edition, 2001.

Snipes, J.A., Gribov, Y., and Winter, A., Physics requirements for the ITER plasma control system, *Fusion Engineering and Design*, 85(3-4):461–465, 2010, doi:10.1016/j.fusengdes.2010.01.019.

Snipes, J.A., Beltran, D., Casper, T., Gribov, Y., et al., Actuator and diagnostic requirements of the ITER Plasma Control System, *Fusion Engineering and Design*, 87(12):1900–1906, 2012, doi:10.1016/j.fusengdes.2012.04.002.

Snipes, J.A., Bremond, S., Campbell, D.J., Casper, T., et al., Physics of the conceptual design of the ITER plasma control system, In *Fusion Engineering and Design*, volume 89, pages 507–511. Elsevier Ltd, 2014, ISBN 09203796, doi:10.1016/j.fusengdes.2014.01.063.

Snipes, J.A., Albanese, R., Ambrosino, G., Ambrosino, R., et al., Overview of the preliminary design of the ITER plasma control system, *Nuclear Fusion*, 57(12):125001, 2017, doi:10.1088/1741-4326/aa8177.

Stangeby, P.C., *The plasma boundary of magnetic fusion devices*, CRC Press, 2000, ISBN 9780750305594.

Sweeney, R., Choi, W., La Haye, R.J., Mao, S., et al., Statistical analysis of m/n = 2/1 locked and quasi-stationary modes with rotating precursors at DIII-D, *Nuclear Fusion*, 57 (1):016019, 2017, doi:10.1088/0029-5515/57/1/016019.

Tamain, P., Tsitrone, E., Ghendrih, P., Gunn, J., et al., Thermal interaction of plasma with gas puffing, *Journal of Nuclear Materials*, 363-365(1-3):844–848, 2007, doi:10.1016/j.jnucmat.2007.01.235.

Teplukhina, A.A., Sauter, O., Felici, F., Merle, A., et al., Simulation of profile evolution from ramp-up to ramp-down and optimization of tokamak plasma termination with the RAPTOR code, *Plasma Physics and Controlled Fusion*, 59(12):124004, 2017, doi:10.1088/1361-6587/aa857e.

The ITER Organization, ITER, URL `https://www.iter.org/proj/inafewlines`.

The Mathworks Inc., MATLAB, a, URL `https://mathworks.com`.

The Mathworks Inc., MATLAB Stateflow, b, URL `https://mathworks.com/products/stateflow`.

Theunissen, R.J.M., Petreczky, M., Schiffelers, R.R.H., van Beek, D.A., and Rooda, J.E., Application of Supervisory Control Synthesis to a Patient Support Table of a Magnetic Resonance Imaging Scanner, *IEEE Transactions on Automation Science and Engineering*, 11(1):20–32, 2014, doi:10.1109/TASE.2013.2279692.

Treutterer, W., Cole, R., Lüddecke, K., Neu, G., et al., ASDEX Upgrade Discharge Control SystemA real-time plasma control framework, *Fusion Engineering and Design*, 89(3):146–154, 2014a, doi:10.1016/j.fusengdes.2014.01.001.

Treutterer, W., Humphreys, D., Raupp, G., Schuster, E., et al., Architectural concept for the ITER Plasma Control System, In *Fusion Engineering and Design*, volume 89, pages 512–517. Elsevier Ltd, 2014b, ISBN 09203796, doi:10.1016/j.fusengdes.2014.02.079.

Treutterer, W., Rapson, C.J., Raupp, G., Snipes, J., et al., Towards a preliminary design of the ITER plasma control system architecture, *Fusion Engineering and Design*, 115:33–38, 2017, doi:10.1016/j.fusengdes.2016.12.026.

Van Beek, D.A., Fokkink, W.J., Hendriks, D., Hofkamp, A., et al., CIF 3: Model-based engineering of supervisory controllers, In *Lecture Notes in Computer Science (including subseries Lecture Notes in Artificial Intelligence and Lecture Notes in Bioinformatics)*, volume 8413 LNCS, pages 575–580. 2014, ISBN 9783642548611, doi:10.1007/978-3-642-54862-8_48.

Van Zeeland, M.A., Boivin, R.L., Carlstrom, T.N., Deterly, T., and Finkenthal, D.K., Fiber optic two-color vibration compensated interferometer for plasma density measurements, *Review of Scientific Instruments*, 77(10):10F325, 2006, doi:10.1063/1.2336437.

Van Zeeland, M.A., Carlstrom, T.N., Finkenthal, D.K., Akiyama, T., et al., Tests of a full-

scale ITER toroidal interferometer and polarimeter (TIP) prototype on the DIII-D tokamak (invited), *Review of Scientific Instruments*, 89(10):10B102, 2018, doi:10.1063/1.5037461.

Veldman, D., Fey, R., Zwart, H., van de Wal, M., et al., Semi-analytic approximation of the temperature field resulting from moving heat loads, *International Journal of Heat and Mass Transfer*, 122:128–137, 2018, doi:10.1016/J.IJHEATMASSTRANSFER.2018.01.085.

Vijvers, W.A.J., Felici, F.A.A., Le, H.B., Duval, B.P., et al., Non-linear digital real-time control in the TCV tokamak, In *39th EPS Conference on Plasma Physics 2012 (EPS 2012) and the 16th International Congress on Plasma Physics*, Stockholm, Sweden, 2012. European Physical Society (EPS).

de Vries, P., Snipes, J., Zabeo, L., Gribov, J., et al., Preparing the Plasma Control System final design for ITER first plasma operations, *Fusion Engineering and Design*, 129:334–340, 2018, doi:10.1016/J.FUSENGDES.2017.12.020.

Vu, N.M.T., Nouailletas, R., Lefèvre, L., and Felici, F., Plasma q-profile control in tokamaks using a damping assignment passivity-based approach, *Control Engineering Practice*, 54: 34–45, 2016, doi:10.1016/j.conengprac.2016.05.003.

Vu, N.M.T., Blanken, T.C., Kong, M., Maljaars, E., et al., Tokamak-agnostic actuator management for multitask integrated control with application to TCV, *submitted to Nuclear Fusion*, 2018.

Walker, M.L., Ambrosino, G., De Tommasi, G., Humphreys, D.A., et al., A simulation environment for ITER PCS development, *Fusion Engineering and Design*, 89(5):518–522, 2014, doi:10.1016/j.fusengdes.2014.02.009.

Walker, M.L., Ambrosino, G., De Tommasi, G., Humphreys, D.A., et al., The ITER Plasma Control System Simulation Platform, *Fusion Engineering and Design*, 96-97:716, 2015, doi:10.1016/j.fusengdes.2015.01.009.

Wehner, W., Lauret, M., Schuster, E., Ferron, J.R., et al., Predictive control of the Tokamak q profile to facilitate reproducibility of high-qmin steady-state scenarios at DIII-D, In *2016 IEEE Conference on Control Applications, CCA 2016*, pages 629–634. IEEE, 2016, ISBN 9781509007554, doi:10.1109/CCA.2016.7587900.

Wehner, W., Barton, J., and Schuster, E., Combined rotation profile and plasma stored energy control for the DIII-D tokamak via MPC, In *Proceedings of the American Control Conference*, pages 4872–4877. IEEE, 2017, ISBN 9781509059928, doi:10.23919/ACC.2017.7963709.

Weisen, H., Dutch, M.J., Hofmann, F., Martin, Y., et al., Effect on confinement of edge-localized modes in TCV, *Plasma Physics and Controlled Fusion*, 38:1415–1419, 1996.

Weisen, H., Alberti, S., Berry, S., Behn, R., et al., Effect of plasma shape on confinement and MHD behaviour in TCV, *Plasma Physics and Controlled Fusion*, 39(12B):B135–B144, 1997, doi:10.1088/0741-3335/39/12B/011.

Weiwen, X., Zetian, L., Xuantong, D., Zhongbing, S., and Zhuravlev, V., Microwave Reflectometry for Plasma Density Profile Measurements on HL-2A Tokamak, *Plasma Science and Technology*, 8(2):133, 2006.

Wesson, J.A., *Tokamaks*, Oxford University Press Inc., New York, third edition, 2004.

Wiesen, S., Reiter, D., Kotov, V., Baelmans, M., et al., The new SOLPS-ITER code package, *Journal of Nuclear Materials*, 463, 2015, doi:10.1016/j.jnucmat.2014.10.012.

Wiesen, S., Köchl, F., Belo, P., Kotov, V., et al., Control of particle and power exhaust in pellet fuelled ITER DT scenarios employing integrated models, *Nuclear Fusion*, 57(7), 2017, doi:10.1088/1741-4326/aa6ecc.

Willensdorfer, M., Wolfrum, E., Scarabosio, A., Aumayr, F., et al., Electron density evolution after LH transitions and the LH/HL cycle in ASDEX Upgrade, *Nuclear Fusion*, 52(11): 114026, 2012, doi:10.1088/0029-5515/52/11/114026.

Willensdorfer, M., Fable, E., Wolfrum, E., Aho-Mantila, L., et al., Particle transport analysis of the density build-up after the L-H transition in ASDEX Upgrade, *Nuclear Fusion*, 53(8): 093020, 2013, doi:10.1088/0029-5515/53/9/093020.

Witrant, E., Joffrin, E., Brémond, S., Giruzzi, G., et al., A control-oriented model of the current profile in tokamak plasma, *Plasma Physics and Controlled Fusion*, 49(7):1075–1105, 2007, doi:10.1088/0741-3335/49/7/009.

Witvoet, G., Steinbuch, M., de Baar, M., Doelman, N., and Westerhof, E., Sawtooth period control strategies and designs for improved performance, *Nuclear Fusion*, 52(7):074005, 2012, doi:10.1088/0029-5515/52/7/074005.

Wong, Y., Hallock, G., Rowan, W., and Wootton, A., Plasma density feedback control in the TEXT tokamak, *Journal of Nuclear Materials*, 196-198:1018–1021, 1992, doi:10.1016/S0022-3115(06)80187-X.

Wonham, W.M., Cai, K., and Rudie, K., Supervisory Control of Discrete-Event Systems: A Brief History 1980-2015, *IFAC-PapersOnLine*, 50(1):1791–1797, 2017, doi:10.1016/j.ifacol.2017.08.164.

Woo, M.H., Hahn, S.H., Jeon, Y.M., Kim, J., et al., Implementation of the forced landing scheme under off-normal events in KSTAR, *Fusion Engineering and Design*, 128:168–174, 2018, doi:10.1016/j.fusengdes.2018.02.023.

Xu, C., Ou, Y., and Schuster, E., Transport Parameter Estimations of Plasma Transport Dynamics Using the Extended Kalman Filter, *IEEE Transactions on Plasma Science*, 38 (3):359–364, 2010, doi:10.1109/TPS.2009.2038220.

Zabeo, L., Murari, A., Innocente, P., Joffrin, E., et al., Different approaches to real time correction of fringe jumps in interferometers for nuclear fusion, *Review of Scientific Instruments*, 2004.

Zabolotsky, A., Weisen, H., Karpushov, A., the TCV team, and the JET EFDA contributors, Influence of particle sources on electron density peaking in TCV and JET, *Nuclear Fusion*, 46(5):594–607, 2006, doi:10.1088/0029-5515/46/5/010.

Zohm, H., *Magnetohydrodynamic Stability of Tokamaks*, Wiley, 2014, ISBN 9783527412327.

Glossary

ASDEX Upgrade .... Axially Symmetric Divertor Experiment Upgrade, tokamak at the Max-Planck-Institut für Plasmaphysik in Garching, Germany

DCN ..... deuterium cyanide

DCS ..... Discharge Control System, the digital control system of ASDEX Upgrade

DEMO ..... DEMOnstration power station

ECCD ..... electron cyclotron current drive

ECE ..... electron cyclotron emission

EC(R)H ..... electron cyclotron (resonance) heating

EKF ..... Extended Kalman filter

FIR ..... far infrared

FSM ..... finite state machine

ITER ..... experimental nuclear fusion reactor under construction in St.-Paul-lez-Durance, France

LCFS ..... last closed flux surface

LIUQE ..... 'equil' spelled backwards, an equilibrium reconstruction code [Moret et al., 2015]

LM ..... locked mode

MHD ..... magnetohydrodynamics

MPC ..... model predictive control

NBI ..... neutral beam injection

NTM ..... neoclassical tearing mode

ODE ..... ordinary differential equation

PCS ..... plasma control system

PCSSP ..... plasma control system simulation platform

PLL ..... phase-locked loop

PDE ..... partial differential equation

RAPDENS ..... RApid Plasma DENity Simulator
RAPTOR ..... RApid Plasma Transport simulatOR
RT ..... real-time
SCD ..... Système Distribué de Contrôle, the digital plasma control system of TCV
SVD ..... singular value decomposition
TCV ..... Tokamak á Configuration Variable, tokamak at the Swiss Plasma Center in Lausanne, Switzerland
TS ..... Thomson scattering
VDE ..... vertical displacement event
XTe ..... electron temperature measurement from soft X-rays

Dankwoord

The past years have been a journey of hope, personal development, hard work and fatigue, but predominantly joy. Without the input of many people I could not have accomplished it. I would like to thank everybody who has supported me during this journey and who has contributed to my research and this thesis.

Marco, dank voor je inspiratie, optimisme, scherp commentaar op de tekst, en vertrouwen in mij. Zonder jou had ik de laatste maanden niet zo ontspannen ervaren. Ondanks jouw vaste slotzin van onze meetings (ik: 'Dankjewel voor je hulp!', jij: 'Ik heb niks gedaan, jongen!') heb je heel veel voor mij gedaan en betekend.

Maurice, bedankt voor je hulp, vertrouwen en constructief commentaar op de teksten. De vele pagina's vol rood commentaar over koppelwoorden, komma's en consistentie in vergelijkingen zijn dit proefschrift zeer ten goede gekomen.

Federico, dank voor je tomeloze hulp, begeleiding, aandacht en steun. Ik heb veel van je geleerd op het gebied van werken in teamverband, probleemoplossend en effectief werken, software development, control en plasmafysica. Dank voor het vele constructieve commentaar op mijn teksten en presentaties, en de prettige samenwerking in de vele dagen en avonden in de control rooms. Dank voor je vertrouwen en de vrijheid die je me hebt gegeven.

I would like to thank the other members of the committee: Siep Weiland, Jacqueline Scherpen and Emmanuel Witrant. Thank you for your assessment of this thesis and for taking part in the defense committee.

I would like to thank the staff at the Control Systems Technology group, DIFFER, the SPC and the IPP for welcoming me and allowing me to do my research. I would also like to thank EUROfusion for the financial support.

Ik heb Gijs, Jasper en Ricardo met plezier mogen begeleiden tijdens hun afstudeerprojecten. Bedankt voor jullie nuttige inbreng en de prettige samenwerking. Daarnaast wil ik mijn fusion homies, kantoorgenoten en collega's in Eindhoven bedanken voor de hulp, samenwerking en gezelligheid. Bert, Hugo, Matthijs, Timo, Artur, Lennart, Bas, Jurgen, Robbert, Stefan, Daniël, Enzo,

Rolf, Rishi, Frans, Ruud, Robin, Robert, Niek, Max, Mark, Chyannie, Ferdie, Martijn, en vele anderen, bedankt!

I've had the pleasure to work with many good colleagues at the SPC, at the IPP and from elsewhere in Europe. I'd like to thank all of you for the enjoyable cooperation, fun parties and conferences, and most importantly the long control room evenings. Trang, Federico P., Francesco, Mengdi, Himank, Anna, Cristian, Olivier, Kevin, Wouter, Ondra and Xenia, Filip, Branka, Chris, Wolfgang, Chiara, Doohyun, and many more, thank you!

Vrienden en vriendinnen, (oud)leden van Jocanto, het combo en de bende van ellende, dank jullie wel voor de gezelligheid, de leuke feestjes, en voor jullie steun om mij overeind te houden gedurende dit schommelende traject.

Anne en Jitka, jullie zorg en liefde hebben me door dit vierjarige traject heen geleid. Dank jullie wel! Lennart, Tinke, Carmen, Jan, papa en mama, dank jullie voor jullie onvoorwaardelijke steun, zorg, gezelligheid en liefde!

Curriculum vitae

Thomas Blanken was born on February 9, 1989 in Nuenen, the Netherlands. After finishing his secondary education in 2007 at the Strabrecht College in Geldrop, the Netherlands, he studied Mechanical Engineering at the Eindhoven University of Technology in Eindhoven, the Netherlands. He obtained the Bachelor of Science in Werktuigbouwkunde in 2010 and the Master of Science in Mechanical Engineering in 2014. He also obtained the Certificate Program *Philosophical Reflection on Science and Technology*. During the summer of 2012, he did an internship at the KTH Royal Institute of Technology in Stockholm, Sweden. In 2014, he started his Ph.D. research at the Dutch Institute for Fundamental Energy Research (DIFFER) and in the Control Systems Technology group at the Department of Mechanical Engineering at the Eindhoven University of Technology. He was awarded a EUROfusion Engineering Grant by the EUROfusion consortium in 2015. During his Ph.D. research, he has worked for considerable time with the Swiss Plasma Center in Lausanne, Switzerland and the Max Planck Institute of Plasma Physics in Garching, Germany.

List of publications

Peer-reviewed journal articles

- T.C. Blanken, F. Felici, C.J. Rapson, M.R. de Baar, W.P.M.H. Heemels, the TCV team and the ASDEX Upgrade team, Control-oriented modeling of the plasma particle density in tokamaks and application to real-time density profile reconstruction, *Fusion Engineering and Design*, vol 126 (2018). doi:10.1016/j.fusengdes.2017.11.006 . Chapter 2 of this thesis.
- T.C. Blanken, F. Felici, N.M.T. Vu, C. Galperti, M. Kong, O. Sauter, M.R. de Baar, the EUROfusion MST1 team and the TCV team, Real-time plasma state monitoring and supervisory control on TCV, *Nuclear Fusion*, (2018). doi:10.1088/1741-4326/aaf451. Chapter 4 of this thesis.

Submitted journal articles

- T.C. Blanken, F. Felici, C. Galperti, O. Kudláček, F. Janky, A. Mlynek, L. Giannone, P.T. Lang, W. Treutterer, W.P.M.H. Heemels, M.R. de Baar, the TCV team, the ASDEX Upgrade team and the EUROfusion MST1 team, Model-based real-time plasma electron density profile estimation and control on ASDEX Upgrade and TCV, *(submitted to Fusion Engineering and Design)*. Chapter 3 of this thesis.

Selected co-authored peer-reviewed journal articles

- E. Maljaars, F. Felici, T.C. Blanken, C. Galperti, O. Sauter, M.R. de Baar, F. Carpanese, T.P. Goodman, D. Kim, S.H. Kim, M. Kong, B. Mavkov, A. Merle, J.-M. Moret, R. Nouailletas, M. Scheffer, A.A. Teplukhina, N.M.T. Vu, the EUROfusion MST1 team and the TCV team, Profile control simulations and experiments on TCV: a controller test environment and results using a model-based predictive controller, *Nuclear Fusion*, vol 57 (2017). doi:10.1088/1741-4326/aa8c48.

- T. Ravensbergen, P.C. de Vries, F. Felici, T.C. Blanken, R. Nouailletas, L. Zabeo, Density control in ITER: an iterative learning control and robust control approach, *Nuclear Fusion*, vol 58 (2018). doi:10.1088/1741-4326/aa95ce.

- P.T. Lang, T.C. Blanken, M. Dunne, R.M. McDermott, E. Wolfrum, V. Bobkov, F. Felici, R. Fischer, F. Janky, A. Kallenbach, O. Kardaun, O. Kudláček, V. Mertens, A. Mlynek, B. Ploeckl, J.K. Stober, W. Treutterer, H. Zohm and the ASDEX Upgrade Team, Feedback controlled, reactor relevant, high-density, high-confinement scenarios at ASDEX Upgrade, *Nuclear Fusion*, vol 58 (2018). doi:10.1088/1741-4326/aaa339 .

- N.M.T. Vu, T.C. Blanken, M. Kong, E. Maljaars, F. Felici, C. Galperti, O. Sauter, the TCV team and the EUROfusion MST1 team, Tokamak-agnostic actuator management for multi-task integrated control with applications to TCV and ITER, *(submitted to Nuclear Fusion).*

- F. Felici, O. Kudláček, T. Ravensbergen, W. Treutterer, T.C. Blanken, A.A. Teplukhina, O. Sauter, B. Geiger, L. Giannone, M. Reich, J. Stober, M. Willensdorfer, the ASDEX Upgrade team and the EUROfusion MST1 team, Model-based design, simulation and testing of an electron temperature profile controller on ASDEX Upgrade, *(submitted to Nuclear Fusion).*

Peer-reviewed articles in conference proceedings

- T.C. Blanken, F. Felici, M.R. de Baar, W.P.M.H. Heemels, Modeling, observer design and robust control of the particle density profile in tokamak plasmas, *2015 54th IEEE Conference on Decision and Control (CDC)*, 15-18 Dec. 2015, Osaka, Japan. doi:10.1109/CDC.2015.7403425 . (contributed)

Non peer-reviewed abstracts in conference proceedings

- T.C. Blanken, F. Felici, M.R. de Baar, W.P.M.H. Heemels, Kalman filter based reconstruction and robust control of the plasma density in tokamaks, *34th Benelux Meeting on Systems and Control*, March 24 - 26, 2015, Lommel, Belgium.

- T.C. Blanken, F. Felici, M.R. de Baar, W.P.M.H. Heemels and the TCV team, Model-based reconstruction and feedback control of the plasma particle density in tokamaks, *42nd EPS Conference on Plasma Physics*, June 22 - 26, 2015, Lisbon, Portugal.

- T.C. Blanken, F. Felici, Implementation of observers, controllers and supervisory systems for tokamaks, *35th Benelux Meeting on Systems and Control*, March 22 - 24, 2016, Soesterberg, the Netherlands.

- T.C. Blanken, F. Felici, C.J. Rapson, the TCV team and the ASDEX Upgrade team, Particle density modeling for real-time density profile reconstruction and fringe jump detection on ASDEX Upgrade and TCV, *43rd EPS Conference on Plasma Physics*, July 4 - 8, 2016, Leuven, Belgium.

- T.C. Blanken, F. Felici, C. Galperti, N.M.T. Vu, M. Kong, O. Sauter, the TCV team and the EUROfusion MST1 team, First results of real-time plasma event monitoring, supervisory control and actuator allocation on TCV, *59th Annual Meeting of the APS Division of Plasma Physics*, October 23 - 27, 2017; Milwaukee, Wisconsin, USA.

- T.C. Blanken, F. Felici, C. Galperti, N.M.T. Vu, M. Kong, O. Sauter, Real-time plasma state monitoring and supervisory control on the TCV tokamak, *37th Benelux Meeting on Systems and Control*, March 27 - 29, 2018, Soesterberg, the Netherlands.

Workshop presentations

- T.C. Blanken, C. Piron, F. Felici, O. Kudláček, C.J. Rapson, A.A. Teplukhina, C. Galperti, O. Sauter, H. van den Brand, J. Citrin, D. Hogeweij, M. Scheffer, S. Coda, C. Galperti, J.-M. Moret, P. Piovesan, W. Treutterer, L. Giannone, M. Willensdorfer, M. Reich, the TCV team, the ASDEX Upgrade team, the RFX-mod team and the EUROfusion MST1 team, Model-based real-time scenario monitoring for transient event prediction with RAPTOR, *21st Workshop on MHD Stability and Control*, November 7-9, 2016, San Diego, California, USA. (invited)

- T.C. Blanken, F. Felici, C.J. Rapson, M.R. de Baar, W.P.M.H. Heemels, Model-based estimation and control of the particle density on TCV and ASDEX Upgrade, *21st Workshop on MHD Stability and Control*, November 7-9, 2016, San Diego, California, USA. (contributed)

- T.C. Blanken, F. Felici, C. Galperti, N.M.T. Vu, M. Kong, O. Sauter, F. Pesamosca, F. Carpanese, the TCV team and the EUROfusion MST1 team, Real-time plasma event monitoring and supervisory control on TCV, *22nd Workshop on MHD Stability and Control*, November 1, 2017, Madison, Wisconsin, USA. (contributed)